
DEVELOPMENT OF QUANTITATIVE DETECTION
STRATEGIES FOR POTENTIAL CANCER
BIOMARKERS FROM EXTRACELLULAR VESICLES
USING LATERAL FLOW ASSAYS

MASTER THESIS AT FRAUNHOFER INSTITUTE IZI
IN THE MASTER COURSE NANOBIO TECHNOLOGY

Student:

Name: Simon BAUMGARTE

Study No.: 20171710

Supervisors:

Dr. Dirk KUHLMIEER

Ana Leonor HEITOR LOPES, MSc

Assessor:

Leonid GUREVICH, Ph.D.

August 31, 2019

Table of Contents

1	Abstract	7
2	Introduction	9
2.1	Prostate Cancer	9
2.1.1	Prevalence and Burden to Health Care Systems	9
2.1.2	Current Diagnostic Methods	10
2.2	Exosomes and Extracellular Vesicles	11
2.2.1	Cell Signaling through Extracellular Vesicles	14
2.2.2	Extracellular Vesicles as Diagnostic Tools	19
2.2.3	Novel Prostate-specific Biomarkers from EVs	20
2.3	Lateral Flow Assay for Point-of-Care Applications	21
2.3.1	Current Designs for Applications of Lateral Flow Devices	24
2.3.2	Detection Labels and Read-Out from Lateral Flow Devices	25
2.4	Analysis of Extracellular Vesicles and their Content on Lateral Flow Platforms	29
3	Objective of this Thesis	31
4	Materials and Methods	32
4.1	Instrumentation and Equipment	32
4.2	Chemicals and Consumables	33
4.3	Conjugation of AlphaLISA Acceptor Beads with anti-PTEN Antibody	35
4.4	Conjugation of Gold Nanoparticles with anti-PTEN Antibody	36
4.5	Conjugation of anti-PTEN Antibody with FITC	36
4.6	Conjugation of AuNS with anti-PTEN Antibody	36
4.7	Conjugation of anti-PTEN Antibody with Quantum Dots	37
4.8	DLS Measurements of Nanoparticles Suspensions	38
4.9	Absorption Measurements of Gold Nanoparticles for Conjugation with anti-PTEN Antibody	39
4.10	Absorption Measurement of Gold Nanoparticles from Conjugate Pad	39
4.11	Absorption Measurement of Gold Nanostars for Conjugation with anti-PTEN Antibody	40
4.12	Absorption Measurements of Quantum Dots	40
4.13	Production of concentrated Cell Culture Medium	41

4.14	LFA with Fluorescent AlphaLISA Bead Conjugates	41
4.14.1	General Assay Scheme for the Detection of PTEN in Solution	41
4.14.2	Screening of Incubation Time for optimized Signal Intensity on Lateral Flow Strips	42
4.14.3	Measurement of PTEN Standard Curves on Lateral Flow Strips	42
4.14.4	Spike-and-Recovery Evaluation of PTEN on Lateral Flow Strips	43
4.15	Standard Protocol for AlphaLISA Assay on Microtiter Plates	44
4.15.1	Determination of Standard Curves	44
4.15.2	Spike-and-Recovery Experiments from EV samples	45
4.16	LFA using AuNP Conjugates with different Antibodies	46
4.16.1	AuNP conjugated to anti-PTEN Antibodies	46
4.16.2	Use of AuNP from Lateral Flow Conjugate Pad with FITC-labelled anti-PTEN Antibodies	46
4.16.3	Test of unspecific Antibody Binding at the Test Line of Lateral Flow Strips	47
4.17	Use of AuNS-Conjugates on Lateral Flow Strips	48
4.18	LFA using Conjugates of anti-PTEN Antibodies with Quantum Dots	48
4.19	Testing the Running Behavior of QD-Conjugates on Lateral Flow Strips	49
4.20	Dot Blot Assay with QD-Conjugates	49
4.21	Agarose Gel Electrophoresis of Quantum Dots	50
5	Results	52
5.1	DLS Measurements of Nanoparticle Suspensions	52
5.1.1	Hydrodynamic Diameters of AlphaLISA acceptor beads	52
5.1.2	Hydrodynamic Diameters of spherical Gold Nanoparticles	53
5.1.3	Hydrodynamic Diameters of Gold Nanostars	54
5.1.4	Hydrodynamic Diameters of Quantum Dots	55
5.2	UV-Vis Absorption Measurement of Nanoparticle Suspensions	56
5.2.1	Absorption Spectra of Gold Nanoparticles for Conjugation with anti-PTEN Antibodies	56
5.2.2	Absorption Spectrum of Gold Nanoparticles from Conjugate Pad	57
5.2.3	Absorption Spectra of Gold Nanostars for Conjugation with anti-PTEN Antibody	58
5.2.4	Absorption Spectra of Quantum Dots	59
5.3	Screening Incubation Time for optimized Signal Intensity on Lateral Flow Strips	60

5.4	Standard Curves for PTEN Detection with AlphaLISA Beads on Lateral Flow Strips	61
5.5	Spike-and-Recovery Evaluation with conjugated AlphaLISA Beads on Lateral Flow Strips	65
5.6	Standard Curves with Standard AlphaLISA Protocol on Microtiter Plates	69
5.7	Spike-and-Recovery Experiments with AlphaLISA Assay on Microtiter Plates	71
5.8	Performance of Gold Nanoparticles on Lateral Flow Strips	73
5.9	Performance of AuNS-Antibody Conjugates on Lateral Flow Strips	75
5.9.1	Visual Read-Out of Lateral Flow Strips with AuNS	75
5.9.2	Line Scanning Detection of Raman Signal on Lateral Flow Strips	77
5.10	Comparison of Limits of Detection for the Detection of PTEN	79
5.11	Performance of Quantum Dots on Lateral Flow Strips	80
5.11.1	Running Behavior of QDs on Lateral Flow Strips	80
5.11.2	Dot Blot Assay with QD-Conjugates	81
5.11.3	Separation of QDs by Agarose Gel Electrophoresis	82
6	Discussion	84
6.1	Conjugation of AlphaLISA Acceptor Beads with anti-PTEN Antibody	84
6.2	Conjugation of AuNP with anti-PTEN Antibody	84
6.3	Conjugation of anti-PTEN Antibody with FITC	85
6.4	Conjugation of AuNS with anti-PTEN Antibody	85
6.5	Conjugation of Quantum Dots with anti-PTEN Antibody and their Use in Lateral Flow Assays	86
6.6	Performance of AlphaLISA Assay Formats	87
6.7	Recovery of PTEN from Spiked Samples	89
6.8	Performance of AuNS-Conjugates on Lateral Flow Strips	90
7	Conclusion and Outlook	92
	References	94
8	Appendix	118
9	Acknowledgements	142

Acronyms

4-NTB 4-nitrothiobenzoic acid

AuNP gold nanoparticles

AuNS gold nanostars

BSA bovine serum albumin

CV coefficient of variation

DIBO dibenzocyclooctyne

DLS dynamic light scattering

DTT dithiothreitol

ECM extracellular matrix

ELISA enzyme-linked immunosorbent assay

ESCRT endosomal sorting complex required for transport

EV extracellular vesicle

FITC fluorescein isothiocyanate

hCG human chorionic gonadotrophin

HEPES 4-(2-hydroxyethyl)-1-piperazineethanesulfonic acid

HRP horseradish peroxidase

ISEV International Society for Extracellular Vesicles

LD loading dye

LFA lateral flow assay

LO large oncosomes

LoD limit of detection

MES 2-(*N*-morpholino)ethanesulfonic acid

MICA MHC class I polypeptide-related sequence A

MRI magnetic resonance imaging

MS mass spectrometry

MV microvesicles

MVB multivesicular body

MWCO molecular weight cut-off

NIR near infrared

o/n over night

PBS phosphate-buffered saline

PBS-T phosphate-buffered saline with 0.1 % Tween-20

PC prostate cancer

PDI polydispersity index

PEG poly(ethylene glycol)

PIP₃ phosphatidylinositol (3,4,5)-triphosphate

PMMA poly(methyl methacrylate)

PNP plasmonic nanoparticle

PoC point-of-care

PSA prostate specific antigen

PTEN Phosphatase and Tensin homolog

QD quantum dot

RT room temperature

S/N ratio signal-to-noise ratio

SD standard deviation

SDS sodium dodecyl sulfate

SERS surface-enhanced Raman scattering

TAE Tris-acetate-EDTA

TEM transmission electron microscopy

TRF time-resolved fluorescence

UCP up-converting phosphor

1 Abstract

In the course of this master thesis PTEN as a potential new biomarker contained in extracellular vesicles of prostate cancer patients was evaluated concerning its detectability in lateral flow assays. To do so, different labelling and detection strategies were exploited to find the most sensitive detection strategy.

In this respect, the AlphaLISA assay format — similar to an ELISA as the standard methodology for biomarker quantification — showed the highest sensitivity for the target of interest. When this assay format was transferred to lateral flow strips, a decrease in sensitivity by 25× could be observed, lying in the same range as that of a visual read-out, based on gold nanostars. These nanoparticles were additionally modified with a Raman-active molecule, however the detection of SERS signals from these conjugates did not result in a substantial increase of the assay sensitivity. Hence, it was shown that a Raman-based detection strategy was comparable to both the visual read-out and a fluorescence-based detection scheme for the quantitative detection of PTEN as the target of interest.

Still, experiments with Raman-active gold nanostars offered only preliminary results, but gave an insight into the technique’s capabilities for further optimization. Together with the possibility to detect signals using a portable reader prototype, this technique was slightly inferior to Europium-doped AlphaLISA acceptor beads, which depended upon another dedicated strip scanning device. Still, the additional visual assessment of test results using gold nanostars allows for the detection of PTEN without further instrumentation at similar sensitivity, rendering gold nanostars a more versatile technique.

Furthermore, spike-and-recovery experiments showed a strong matrix effect for detection strategies using AlphaLISA acceptor beads on lateral flow strips. These findings stress the importance of a suitable calibration of the system, as well as of finding appropriate purification or enrichment strategies for the samples to be tested. In these experiments, the chemiluminescence-based standard format of the AlphaLISA assay again showed most precise results, while requiring most complex instrumentation.

Lastly, different conjugation chemistries and suitable characterization techniques for nanoparticles to be conjugated with antibodies were exploited throughout this thesis, allowing to assess the success of each conjugation protocol.

Overall, a starting point for the formation of diverse conjugates to be used in lateral flow assays and an evaluation of their performance is reported, giving a first

characterization of the most promising detection schemes. For future experiments, it remains to validate the performance of Raman-based detection strategies as the most versatile label found in this work. Furthermore, the transition from *in vitro* experiments to clinical samples presents another challenge for the assay format, requiring further optimization and calibration of the lateral flow assay reported here. However, the obtained data showed promising results, making an implementation of the assay worthwhile in the future.

2 Introduction

2.1 Prostate Cancer

2.1.1 Prevalence and Burden to Health Care Systems

Although the incidence and cancer mortality are declining over the past years, recent statistical evaluation has shown, that prostate cancer (PC) is still the most commonly diagnosed type of cancer in men and accounts for the second most deaths of male cancer patients [1]. The probability of developing PC increases with age [1] and together with the increasing life expectancy and higher average age due to demographic changes, health care systems are facing a high economic burden with respect to PC treatment [2].

However, not only the treatment of PC is demanding, but also the surveillance of the condition in patients, where diagnosis does not immediately lead to a curative intervention, due to a low-risk classification [3, 4, 5]. For these cases, Tosoian *et al.* reviewed active surveillance as an approach with increasing interest to monitor the progression of PC and limit treatment to patients, whose progression in the disease necessitates intervention. Choosing the approach, the authors stated that adverse effects of aggressive interventions — especially for patients with lower-risk cancer types and of high age — can be circumvented to avoid an impaired quality of life after unnecessary treatment [3]. Nevertheless, active surveillance still requires patients to undergo frequent biopsies, monitoring of prostate specific antigen (PSA) levels or clinical examination to verify the state of the tumor [3]. Hence, patients are dependent on physicians and ongoing re-assessment, also leading to an economic burden.

In contrast, patients with high-risk PC most commonly need to undergo radical prostatectomy, radiation or the combination of radiation after surgery [6]. For these interventions, the adverse effects mentioned above include bowel irritation, impaired urinary control or sexual dysfunction [7, 8]. Due to the discomfort arising from the reduction in quality of life, several measures have been proposed, ranging from pelvic floor training to improve urinary incontinence [9], pharmacological cure for erectile dysfunction [10, 11] and also psychological counseling by personal therapy [12] or self-guided online support [13]. Hence, even after successful intervention, patients still require further medical and psychological support, as it is the case for those under active surveillance. Therefore, it would be desirable to minimize the work load for physicians, allowing them to rapidly monitor if PC develops or progresses further

in male patients. Given such a point-of-care (PoC) device, the need for frequent laborious tests could be reduced and performed only when indicated by the results of rapid tests, allowing to reduce the economic burden on health care systems.

2.1.2 Current Diagnostic Methods

Up to date, diagnosis of PC is based on several approaches, which are mainly digital rectal examination, the use of needle biopsy or determination of serum PSA levels [14, 3]. Especially the latter method can allow to identify small volume PC at the onset of the disease, compared to the other methods [14]. The implementation of the sensitive technique in the late 1980s was used to perform broad screenings of men in the years thereafter, giving rise to a major peak in cancer statistic, as also patients without symptoms were diagnosed with PC [1]. However, elevated PSA levels may also arise from other prostate-related diseases like prostatitis and often benign prostatic hyperplasia, as well as physical disruption during biopsy or simply the patient's age, resulting in low specificity and therefore a high number of false-positive diagnoses for PC [15]. Hence, the extensive testing of male patients is not recommended by the U.S. Preventive Services Task Force anymore to decrease the number of overdiagnoses and subsequent overtreatment in patients, whose tumors would have remained asymptomatic over their lifetime [16]. Nevertheless, in patients with a diagnosis for PC, monitoring the serum level of PSA might give an indication of the progression of the disease and the possibility of further diagnostic assessment, rather than direct intervention [3, 17]. Apart from the aforementioned, further diagnostic tools have been introduced in recent years. One of these is multiparametric magnetic resonance imaging (MRI) [6, 3], an imaging technique, which was already employed in clinical trials for active surveillance of patients with low-risk PC [4, 18]. Lastly, novel biomarkers are being investigated as indicators of PC progression and only a few of these are already employed in diagnostic or prognostic commercial solutions [6, 19]. Most of these utilize different sets of genes, associated with PC, the determination of mRNA levels or epigenetic modifications of relevant genes [19]. Additionally, Kretschmer and Tilki reviewed quantitative proteomic approaches and the quantitation of mRNA from extracellular vesicles (EVs) [19]. However, so far the protein content of EVs secreted from PC cells has not been used in commercial products to assess the cancer state.

2.2 Exosomes and Extracellular Vesicles

Extracellular vesicles have first been described in 1981 by Trams *et al.* as fragments of the originating cells, which are shed having a defined content of membrane proteins and sphingomyelin [20]. It was believed, that cells liberated these vesicles to export membrane proteins in maturation and re-organization processes [21, 22]. Only 15 years after their discovery, it was found that cells also secrete vesicles from multivesicular bodies (MVBs) — instead of simple shedding off membrane fragments — and that these appeared to have a physiological role, resembling the cells of origin [23]. Starting from these findings, the understanding of EVs was driven forward and their classification became more precise, as what Trams *et al.* termed EVs, where much bigger vesicles than those with physiological relevance discovered by Raposo *et al.* [24, 25]. Hence, it is now known, that EVs are highly abundant with approximately 1×10^{12} to 3×10^{12} vesicles per mL plasma and different types of EVs are differentiated according to size and origin [26, 27]. Figure 2.1 gives an overview of these different types and simplified schemes of their biogenesis.

The smallest EVs are exosomes with sizes of 40 nm to 100 nm in diameter [28]. These originate from MVBs and are secreted upon their fusion with the plasma membrane [29, 30]. However, there is still no consensus about the precise size and different types of origin for exosomes. Hence, the term EV will be used throughout this report for examples of published data. In contrast to these, ectosomes are a class of EVs which originate solely from budding of the plasma membrane [29]. In the latter category, microvesicles (MVs) were initially identified as products of red blood cells, but the picture has been broadened to other cells of origin up to date. These EVs have an intermediate size of 100 nm to 1000 nm [31, 26, 29, 28]. Apart from different sizes and due to distinct biogenesis pathways, these two types of EVs also differ concerning their cargo and composition [32]. In figure 2.2 some examples of protein cargo, components of the lipid bilayer membrane and membrane proteins are given for both exosomes and MVs. As it can be seen, these payloads overlap between both EV types in many cases, but there are also striking difference, such as ceramide in exosomal membranes, which is associated with microdomain formation or different tetraspanin-proteins in the bilayer membranes, which have been used as specific biomarkers for exosomes [32].

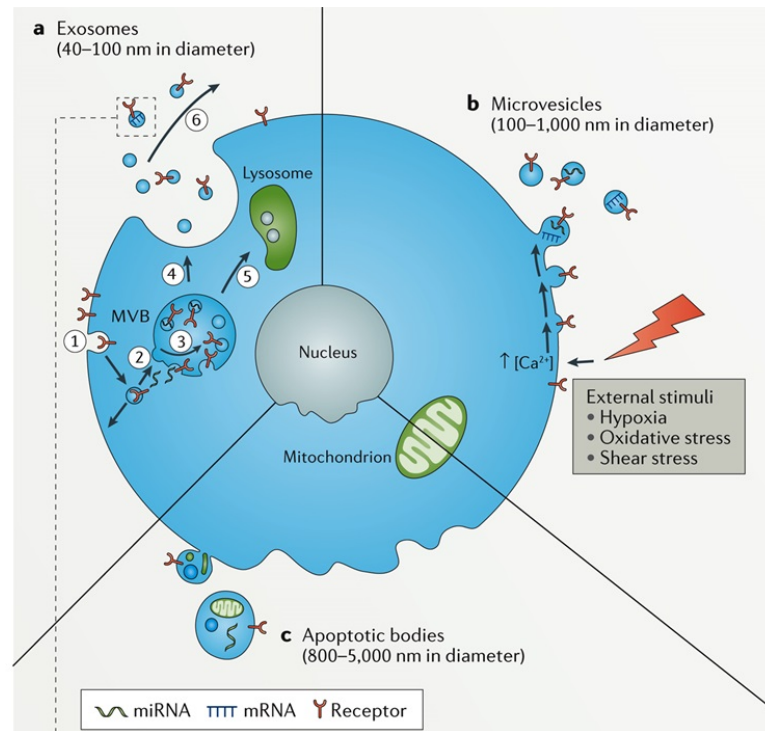


Figure 2.1 Formation of different kinds of EVs. a) Exosomes are the smallest EVs. These originate from early endosomes, that are endocytosed by cells and after maturation to late endosomes fuse with MVBs. The larger endosomes can fuse with the cell membrane to release exosomes or target their content for degradation in lysosomes (green). b) Microvesicles are bigger in size and originate from protrusions of the plasma membrane, which release vesicles by budding. These EVs are released upon cellular stress, mediated by receptor-dependent or Ca^{2+} -concentration dependent pathways. c) The biggest EVs are apoptotic bodies, liberated from cells in the late stage of apoptosis. These vesicles are highly heterogeneous and may contain large fractions of cytoplasmic material such as organelles, whereas the aforementioned EVs carry mostly distinct proteins or nucleic acids. Figure modified from [28].

The last and biggest classes of EVs are apoptotic bodies and large oncosomes (LO) with diameters of approximately $1\ \mu\text{m}$ to $4\ \mu\text{m}$ and $1\ \mu\text{m}$ to $10\ \mu\text{m}$, respectively [29, 26]. Apoptotic bodies are released in the late stage of apoptosis by both cancer and other cells, contain nuclear fragments and it is discussed, whether the cancer-derived DNA might enable horizontal propagation of cancer-related genes [33, 29]. LOs on the other hand originate solely from cancer cells — as their name indicates —, most of which have been described for aggressive, highly migratory and therefore metastatic tumors [29, 34, 35]. In addition to their large size, these EVs are also characterized by oncogenic cargo [31, 29].

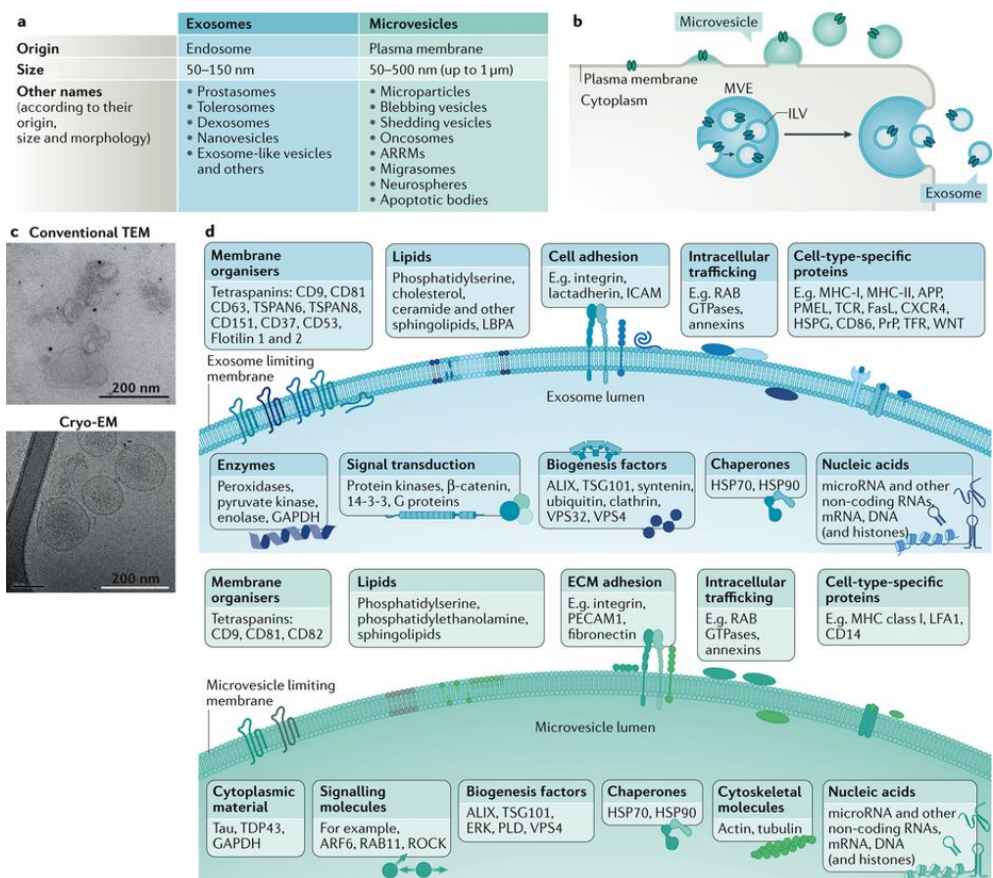


Figure 2.2 Comparison of exosomes and microvesicles. a) Exosomes differ from MVs concerning their organelles of origin and size range. Both types of EVs have been termed with specific names, reflecting their specific size, morphology or cells of origin. b) Cells shed MVs and exosomes *via* different pathways. Microvesicles result from direct budding off the plasma membrane, whereas exosomes are formed as intraluminal vesicles (ILV) by inward budding first, which are located in MVBs. Only a fusion of MVBs with the cell membrane releases the exosomes in the intercellular space. c) Transmission electron microscopy (TEM) images of EVs. Processing steps in conventional TEM leads to shrinking of EVs and non-native states. Only the use of cryo-TEM allows to image EVs in a more native state. d) Components of EVs, as identified by different researchers so far. These can range from soluble and membrane proteins, over different types of nucleic acids to distinct components of the lipid bilayer. Especially the cell type-specific components are highly dependent on the origin and type of EV, whereas both types also share a number of overlapping cargoes. The lipid bilayer composition and specific membrane proteins of the tetraspanin family are means to differentiate between exosomes and MVs. Figure taken from [32]

Despite the specifications for different classes of EVs made here, it has to be stated that for the isolation of EVs, most techniques do not provide specificity for a certain type. Several authors have therefore mentioned, that results obtained for EV populations described as 'exosomes' may instead have been made for mixtures of EVs of different origin and should be seen critically [36, 37, 38]. This is due to the fact, that small EVs are very similar concerning their physical properties, such as size, buoyant density and membrane orientation and hence EVs of non-MVB origin are often co-isolated with exosomes [38, 37]. This has to be considered especially for the literature referenced later in this work, investigating the composition and biochemical properties of EV populations referred to as 'exosomes'. To omit these uncertainties in the investigation of distinct EV subtypes, it is hence inevitable to standardize specific isolation methods based on markers for the desired EV class — until then, it is recommended to refer to these co-isolated populations as 'small EVs'. In this respect, the International Society for Extracellular Vesicles (ISEV) is continuously aiming at the definition of these standards, considering the progress in EV research worldwide [39].

2.2.1 Cell Signaling through Extracellular Vesicles

Although the horizontal gene transfer by apoptotic bodies still requires further investigation [33, 29], the finding that smaller EVs allow for the transfer of functional RNA molecules between cells has risen great attention in the scientific community [24]. In the years 2007 and 2008 it was shown by different research groups, that the RNA cargo of EVs was functional and could be expressed by cells taking up these vesicles — a mechanism previously unknown [40, 41]. Furthermore, it was observed by Valadi *et al.* that this process even allowed for cross-species transfer of murine RNA in EVs, leading to the expression of the respective mouse proteins in human cell lines [40]. The aspect of transferring oncogenic information from tumor to benign cells was found shortly thereafter by Skog and co-workers, who also envisioned the use of EVs for diagnostic purposes in cancer patients [41]. A simplified scheme of this cell-cell communication mechanism by EVs is depicted in figure 2.3

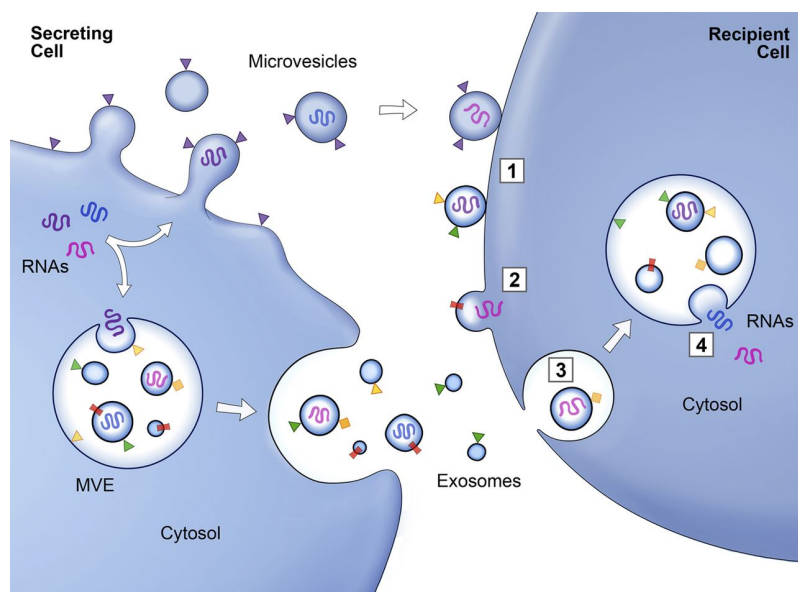
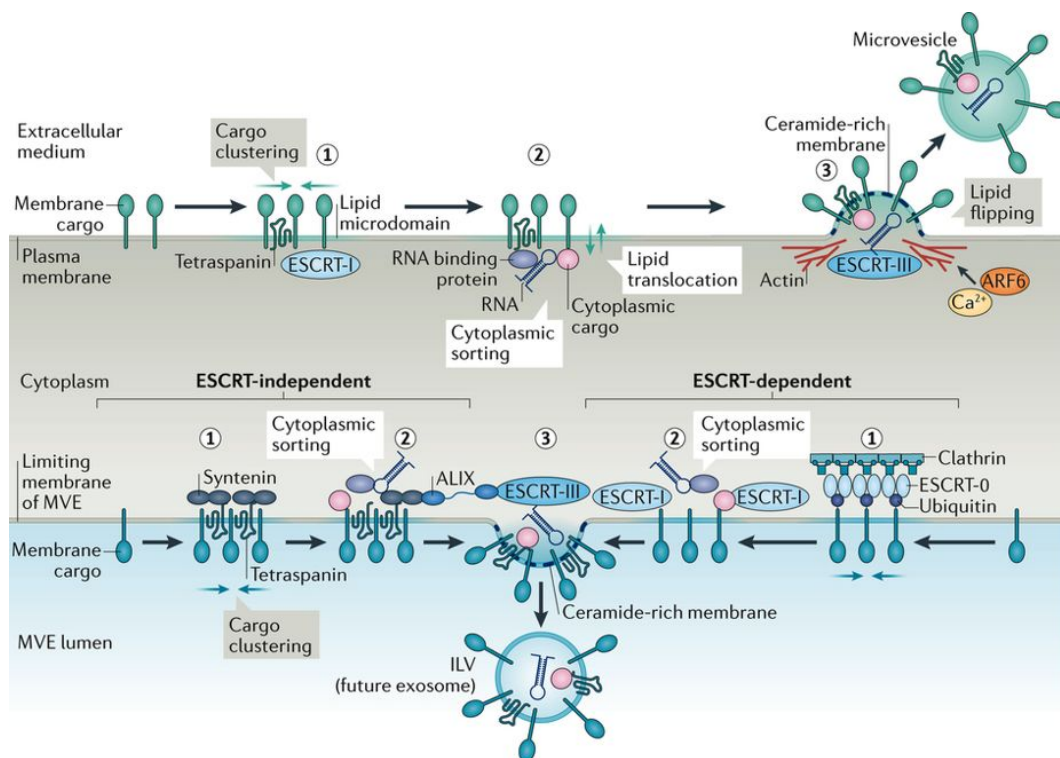


Figure 2.3 Schematic representation of EV trafficking between donor and recipient cells. Transmembrane proteins (rectangles), membrane-associated proteins (triangles) and RNA molecules (curved lines) may be incorporated inside MVs during budding or in exosomes within MVBs. Exosomes are released, when MVBs fuse with the donor cell membrane. Both MVs and exosomes may then be taken up by recipient cell after association (1) and fusion (2) with the plasma membrane, or by endocytosis of the EVs (3). Fusion of the EV with the membrane of the endocytic vesicle liberates the EV cargo in the recipient cell cytosol (4). Figure taken from [25].

As diverse as the different classes of EVs, are the mechanisms by which they allow for the communication with recipient cells. As it was reviewed by van Niel and co-workers last year, exosome biogenesis may occur *via* pathways, which until now were differentiated into endosomal sorting complex required for transport (ESCRT)-dependent and ESCRT-independent formation of exosomes in MVBs, which are compared to microvesicle biogenesis in figure 2.4 [32].

In either way of exosome biogenesis, the future cargo is clustered within microdomains of endosomes, which will later become part of MVBs. For the ESCRT-dependent pathway, subunits 0 and I of the ESCRT complex associate transmembrane proteins that are ubiquitylated in microdomains. In addition, certain lipids of the membrane are clustered in these domains and soluble components associate with the ESCRT subunits to be internalized in exosomes [32]. The ESCRT-II and ESCRT-III subunits are then required to mediate budding of the endosomal membrane and its fission to form exosomes inside MVBs [42, 43]. The ESCRT-independent pathway



Nature Reviews | Molecular Cell Biology

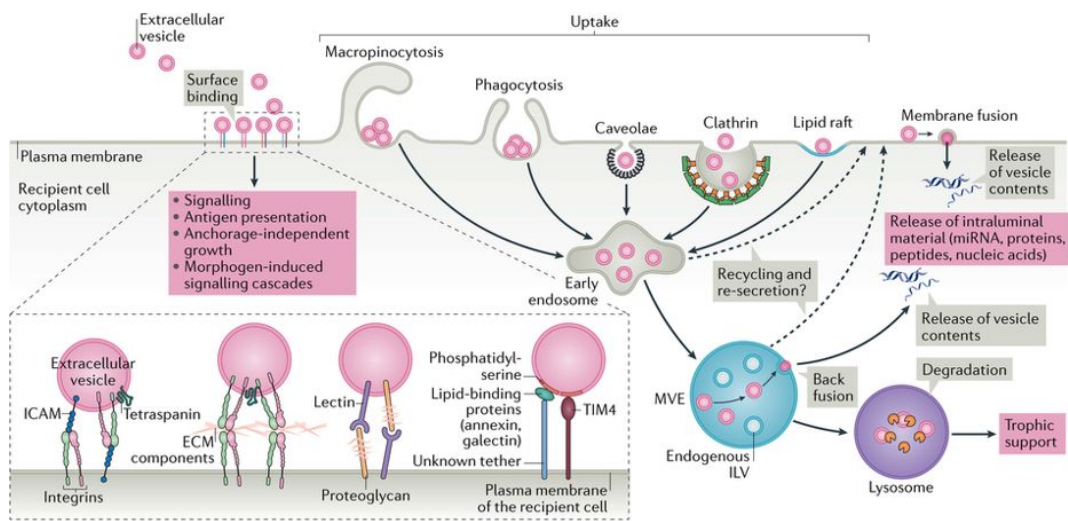
Figure 2.4 Pathways for the biogenesis of MVs and exosomes. The proposed mechanism for MV formation involves the clustering of membrane proteins and cytosolic payloads on microdomains, which bud out and are released into the extracellular environment in dependence of the ESCRT-III complex. Exosomes can originate both from ESCRT-dependent or -independent pathways. In either case, a clustering of cargo on membrane microdomains, which subsequently bud also takes place. The fission of future exosomes into MVBs is in both cases also mediated by the ESCRT-III complex. Figure taken from [32].

was first shown to depend on ceramide. This lipid membrane component is generated by the hydrolysis of sphingomyelin by neutral type II sphingomyelinases [44] and subsequently assembles in subdomains, imposing negative curvature to facilitate budding [45]. Alternatively, members of the tetraspanin protein family — such as CD63, CD81, CD82 and CD9 — have been suggested to be involved in regulating the sorting of cargo to exosomes [46, 47, 48, 49]. As for ceramide, these proteins also organize into microdomains on the endosomal membrane, together with other proteins of the cytosol and transmembrane proteins. Tetraspanins are thus believed to be involved in cargo sorting and the formation of membrane buds [50]. After the

formation of exosomes in MVBs, these have to be targeted for secretion to prevent the fusion with lysosomes and the subsequent degradation of cargo proteins. However, the processes regulating the balance of targeting MVBs to either lysosome or cell membrane fusion are still not fully understood, but it is suspected that distinct mechanisms are in play for each pathway [32]. Secondly, MVBs have to reach the cell periphery to be able to fuse with the plasma membrane — a transport process, which has not been completely unraveled, as well [32]. So far it was shown that MVBs are transported towards the plasma membrane on microtubules [51] in the case of T cells, involved in immunological response. When reaching the cell periphery, a reorganization of the peripheral actin cytoskeleton is then required for MVBs to dock to the plasma membrane [52]. Following these processes, the MVB can fuse with the plasma membrane to release the contained exosomes into the extracellular space for them to reach their target cells [32], which may as well be the secreting cell itself [53].

A very similar mechanism has so far been revealed for the biogenesis of MVs: in a first step, cargo within the cell membrane is clustered in microdomains, together with proteins of the tetraspanin family, and subsequently cytoplasmic cargo associates with these microdomains [32]. Opposed to exosomes, it was shown that a reorganization of membrane lipids between both leaflets of the bilayer is observed for MV biogenesis, which together with the unique membrane compositions causes bending of the membrane [54, 32]. This process is followed by fission of the MVs, which is again assisted by the ESCRT-III machinery [32].

Once EVs reach the target cell, different mechanisms of interaction are possible to deliver cargo to the recipient cell or trigger cellular response upon association with the target cell [32]. These include the binding to specific receptors or cell surface proteins, the uptake of EVs by different mechanisms of endocytosis or the fusion of exosome and cell membrane [32], as it is depicted in figure 2.5.



Nature Reviews | Molecular Cell Biology

Figure 2.5 Overview of different pathways, facilitating the delivery of exosomal cargo in recipient cells. EVs may bind to specific cell surface molecules, such as integrins or other receptors. By these surface molecules, intracellular signaling cascades can be initiated. Otherwise, EVs might fuse with the recipient cell membrane; a process by which the cargo is simply delivered to the cytoplasm. Lastly, different ways of endocytosis are possible, by which EVs enter the recipient cell in endosomes. These processes occur by protrusions of the recipient cell or at special microdomains of the cell membrane, such as lipid rafts or clathrin-coated pits. Figure taken from [32].

For several cell types it has been shown that the recognition of membrane components of EVs targets these to the respective cell types *via* specific receptors of the cell membrane [55, 56, 57, 58]. Among these molecules are tetraspanins, distinct types of lipids, integrins or components of the extracellular matrix (ECM) [32]. As an example, integrins on the membrane of EVs were found to interact with cellular receptors [59], whereas cellular integrins were shown to recognize components of the ECM [60, 61] and tetraspanin membrane proteins of EVs for their targeted docking [62]. In addition, certain glycosylation patterns of the EV membrane proteins may be recognized by cellular receptors [63]. Another way of docking to the recipient cell is the recognition of certain lipids within the EV membrane, recruiting lipid-binding proteins [64]. After binding to the target cell membrane, EVs may persist at the membrane [57, 49] or can be taken up by the cell — again *via* several different mechanisms [32]. These might be rather nonspecific endocytic processes, such as macropinocytosis [65] or phagocytosis [66]. Alternatively, more specific paths might be taken, for example mediated by clathrin-coated pits of the recipient cell [67] or

through caveolae [68]. Lastly, the composition of the recipient cell membrane and the formation of lipid rafts can aid in the internalization of EVs [69]. Subsequently EVs may release their cargo by back fusion with the membrane of MVBs in the recipient cell, if they did not fuse directly with the recipient cell membrane [32]. Despite the numerous ways for exosome recognition and internalization by recipient cells that were mentioned here, these processes still require further understanding [32]. Therefore, research has also been directed towards the analysis of EVs and their cargo for diagnostic purposes without the need to fully understand their effects on potential receptor cells; an approach which will be discussed in the following chapter.

2.2.2 Extracellular Vesicles as Diagnostic Tools

Extracellular vesicles, have gained increasing interest as diagnostic tools due to their distinct cargo, resembling the cells of origin, and are envisioned to allow for minimally invasive diagnosis of pathological conditions in a technique called liquid biopsy, as it has been extensively discussed [70, 71, 72]. For this purpose, different types of exosomal cargo may serve as specific biomarkers for the diagnostic evaluation of EVs, which may be either proteins or nucleic acids [72]. On the other hand, some other proteins — tetraspanin transmembrane proteins, like CD9, CD63 and CD81 for example — seem to be present in EVs of different origin and might therefore aid in isolating EVs in general [73].

Yoshioka *et al.* used two of these tetraspanins, CD9 and CD63, for the detection of EVs originating from colorectal cancer in a single-step, homogeneous luminescence assay based on lanthanide chelates. When combining the detection of CD9 with CD147, another potential biomarker of carcinomas [74], the authors claimed, that they could discriminate healthy from cancer patients with high sensitivity and even detect early forms of colorectal cancer, which is problematic with currently used biomarkers for diagnosis [71]. However, high signal intensities of the luminescence assay were not detected in all confirmed cancer patients. As mentioned before, other studies targeted the content of EVs for analysis [75]. This method employed filter units to purify EVs from urine and subsequently RNA was extracted from EVs to assess the copy number of three different mRNA molecules [75]. Using this approach it could be shown later, that the prediction of prostate cancer state and discrimination between different states of cancer was more accurately achieved than with standard protocols, using needle biopsy and the determination of PSA levels [76]. Another study investigated markers of pancreatic cancers, employing both exosome cargo and

surface markers. The authors showed that four different microRNA species were significantly upregulated in pancreatic cancer patients and correlated this finding with fluorescent labelling of five different surface markers. Although their approach employed laborious ultracentrifugation steps for exosome purification and the use of flow cytometry, making it a protocol with low efficiency and throughput, it was shown, that pancreatic cancer and its progression could be sensitively diagnosed by the combination of microRNA and exosome surface markers [77]. As a last example, a study investigated the presence of Claudin-4 in EVs, a transmembrane protein associated with cellular tight junctions [78], which was already observed to be over-expressed in cancer patients [79]. Despite the time-consuming protocol presented by the authors, which does not allow for clinical implementation, it could be shown, that Claudin-4 was also heavily incorporated in EVs of ovarian cancer patients, but not in those of healthy donors [80]. Taken together, it becomes apparent, that EVs and their cargo are promising targets for diagnosis with high sensitivity, especially in the management of cancer. However, for the clinical translation of research results it is essential to find easy-to-use and time-saving techniques, that allow for the distinct collection of the desired sub-group of EVs and their standardized analysis [72, 81, 82, 83].

2.2.3 Novel Prostate-specific Biomarkers from EVs

Despite the fact, that EVs are not used in clinical diagnosis of PC yet, recent findings have shown that great promise lies in the analysis of exosome cargo. In this concern, Minciocchi *et al.* presented an extended review of proteins from EVs, that were identified by mass spectrometry (MS) approaches and shown to resemble their cells of origin [26]. Apart from proteins, again DNA, mRNA and miRNA molecules were shown to be associated with EVs, as it is summarized in figure 2.6 [26].

From this figure, it becomes clear that numerous proteins are being investigated as potential biomarkers, some of which are evaluated in initial clinical studies for their suitability, as reviewed by Vlaeminck-Guillem [84]. Nevertheless, the analysis of exosome cargo has so far only been shown to be successful for the determination of mRNA levels. The work of Donovan *et al.* therefore analyzed the level of three different gene transcripts in EVs from urine and the group could show later, that the developed assay proved to be more precise in determining PC state than standard-of-care diagnosis [75, 76]. Another promising novel biomarker was presented by Gabriel *et al.*, which is Phosphatase and Tensin homolog (PTEN) [85]. This protein

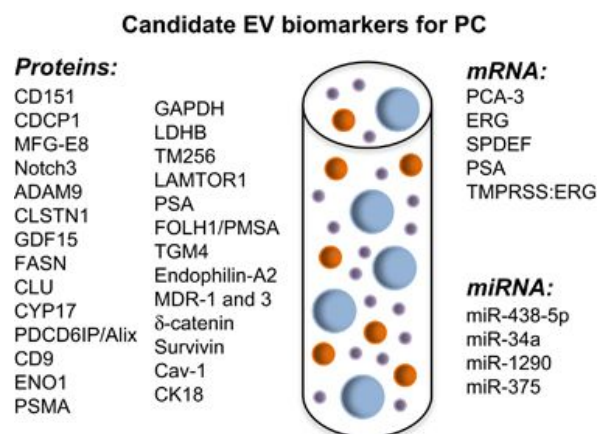


Figure 2.6 Hypothesized protein and nucleic acid biomarkers for the detection of PC. Figure taken from [26].

acts as a tumor-suppressor, as its phosphatase domain mainly dephosphorylates phosphatidylinositol (3,4,5)-triphosphate (PIP₃). By keeping the concentrations of PIP₃ low, pathways for cell proliferation are inhibited and cell growth is controlled [86]. It has been shown, that a loss of PTEN in cells is consequently associated with the progression of cancer [87], which was believed to arise from down-regulation of gene expression [85]. However, the group has shown, that PTEN is additionally exported in EVs in cancer patients having low cellular PTEN levels, whereas healthy patients showed no PTEN in blood EVs. Therefore, exosomal PTEN was suggested as a novel and specific biomarker, whereas PSA was shown to be present in blood EVs of healthy donors and patients with PC [85].

2.3 Lateral Flow Assay for Point-of-Care Applications

Lateral flow assays (LFAs) have been marketed for over 35 years now, with the first and most commonly known application being the detection of human chorionic gonadotrophin (hCG) to ascertain pregnancy [88]. Nowadays, these tests have a much wider range of application, for example in the detection of pathogens, testing for toxins in food, surveillance of environmental contaminants including biological warfare agents or proof of drug abuse [89, 90]. The detection of the analyte of interest relies on its recognition, as for example by protein-specific antibodies or by complementary strands to desired nucleic acid molecules, and on either labelling the analyte itself or the recognition molecules to facilitate a visual read-out [89]. Despite the advantage of not requiring laboratory equipment when performing analyses

with LFAs and fast test-to-result times of 10 min to 20 min, which make these test a desirable format for PoC applications, the test read-out is in most cases only qualitative or semi-quantitative [89, 90]. Figure 2.7 shows the general set-up of a LFA and its working principle, which will be explained in the following.

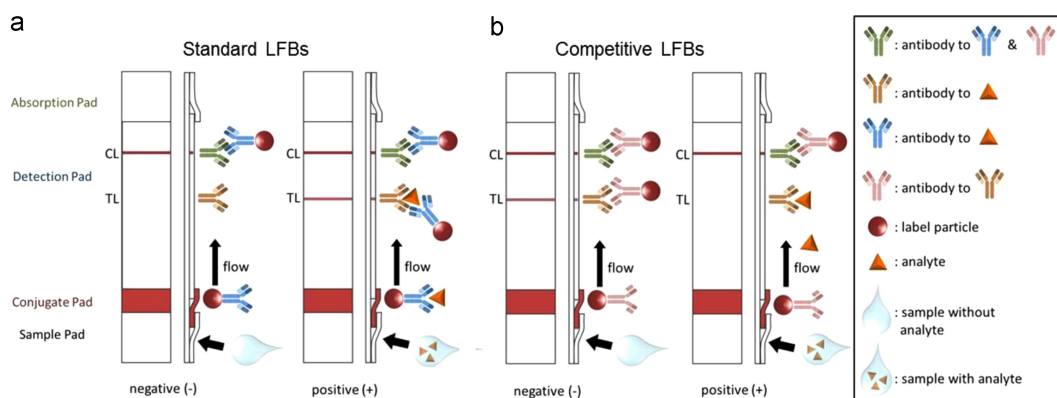


Figure 2.7 Schematic representation of two working principles of LFAs. In both cases, the liquid sample is applied onto the sample pad. When migrating towards the nitrocellulose membrane, the liquid picks up the labelled recognition elements (here, red spheres with blue antibodies) in the conjugate pad. In standard sandwich LFAs, the analyte (orange triangle) binds to the specific antibody during further migration through the membrane. A second antibody (yellow) then captures the bound analyte at the test line (TL), whereas unoccupied antibody-label conjugates are captured at the control line (CL) by (secondary) antibodies specific for the species in which conjugate-antibodies were raised (green). A positive test therefore shows a signal at both test and control line. In the case of competitive LFAs, occupation of the capture antibody (yellow) at the test line inhibits binding of the conjugated antibody (pink). Hence, the signal at the test line disappears in a positive test, whereas the signal of the control line is produced as before. In either cases, excess liquid finally reaches the absorption or wicking pad. Figure taken from [91].

LFAs rely on the dislocation of analytes from liquid samples, which is in most cases achieved by fabricating test strips from nitrocellulose. As the membrane is fragile and thin, it is generally mounted on backing materials, such as plastic or nylon, making it appropriately stable for processing [89]. At one end of the strip, a sample pad for application of the liquid sample is located and overlaps with the conjugate pad. The latter contains the specific recognition elements for the desired analyte, which are dried within this pad [89]. It is here where the interaction of analyte and recognition element, for example between a protein and an antibody, is initiated, but it continues throughout the membrane, to which the conjugate pad is

connected [89]. The liquid subsequently passes the test and control line, deposited onto the membrane and finally reaches the absorption pad — also called wicking pad — at the opposing end of the strip. This last element of a LFA maintains the capillary flow through the nitrocellulose membrane by absorbing excess liquid [89].

For the interaction of analytes with the control and test line, two formats are possible. On the one hand, the sandwich type requires bigger molecules, such as proteins, with at least two epitopes, which can be bound by two different antibodies [89]. In this case, the first antibody is conjugated to a label facilitating the read-out — these nanoparticulate labels usually have sizes of 15 nm to 800 nm [89] and most often colloidal gold is used, but other nanoparticle conjugate have already been investigated [91, 90]. When the analyte is bound to this construct passing the conjugate pad and the matrix, a second epitope of the analyte can be recognized by a second antibody deposited at the test line and therefore fixes the label at the test line. Conjugates devoid of analyte migrate further along the matrix and are captured by a secondary antibody, specific for the antibody conjugated to the label, to create a signal at the control line [89, 91]. In this way, a signal at the control line indicates the correct migration of the fluid through the membrane and the integrity of the antibody-label conjugate. The appearance of a second line in addition to the control line shows a positive result, as it can only arise in the presence of the analyte bound between the two antibodies [89].

On the other hand, competitive LFAs are applied for small molecules or those with just one epitope [89]. In these assays, two different approaches are possible to obtain a decreasing signal intensity at the test line with increasing analyte concentration. First, the test line comprises only a specific antibody for the analyte. In this case, both the analyte in the sample and a labelled analyte molecule are applied on the sample pad, leading to competition between both [92]. Second, it is possible to spot a conjugate of the target molecule with a protein onto the test line. When a labelled antibody is then contained in the conjugate pad, it will be occupied by analyte from the sample and therefore not bind to the test line — again, a decrease in test line signal results for a positive test [93]. In either case, the control line again captures unbound antibodies *via* species-specific antibodies to assure correct functioning of the test.

2.3.1 Current Designs for Applications of Lateral Flow Devices

Given the basic lay-out of lateral flow devices above, many different designs — comprising specialized elements for distinct applications — have been implemented so far. For example, LFAs developed for the analysis of whole blood are often designed with special sample pads that retain red blood cells [94] or with membranes covering the sample pad and through which the sample is filtered [95]. In this way, erythrocytes or their fragments are prevented from obscuring the read-out of LFAs, which is especially important when results are assessed visually [96]. Additionally, it renders the tests independent of laboratory equipment and skilled workers, as centrifugation steps to obtain serum from blood can be circumvented. Furthermore, it has been shown that the addition of anticoagulants to retain the liquid properties of blood samples, may drastically lower the limit of detection (LoD) for biomarkers in lateral flow devices [97], further stressing the ease of on-device sample preparation. Other samples may however be solid with a need for extraction prior to analysis. This is mostly true for the detection of food contaminants, such as antibiotics in meat or eggs [98, 99], as well as remains of insecticides in vegetables [100]. But even, if samples are in a sufficiently liquid state for detection, they might not lead to an ideal result. One example is urine, which may vary strongly concerning its pH. Therefore, components within the sample pad are required to compensate for these variations [101]. Other liquids may migrate through the nitrocellulose membrane too fast by capillary forces, leaving an insufficient time for interaction of analytes with the recognition molecules. Hence, research has been directed to modify the given porous matrix in an attempt to improve the read-out signal. Rivas *et al.* achieved this goal for example by printing wax pillars in the sub-mm range onto lateral flow strips, which decreased the flow speed of samples, resulting in a 3-fold sensitivity increase [102]. Despite these modifications of the standard layout of LFAs, the technique has high potential for further improvement and optimization, as it is reviewed elsewhere [101, 103].

2.3.2 Detection Labels and Read-Out from Lateral Flow Devices

Until today, gold nanoparticles (AuNP) remain as the standard conjugate for the visualization of LFA read-outs due to their long shelf-life, ease of production and coupling and short test-to-result times [91, 104, 90]. These labels can even be read by the naked eye, as colloidal gold suspensions have distinct colors, depending on the size and shape of the contained particles [105, 106]. Using AuNP, LFAs usually produce only qualitative results — as the appearance of the second test line in pregnancy tests [88] —, which might be a sufficient result for many applications. However, others might require a lower LoD or a quantitative result. Therefore, more sensitive approaches have been developed using AuNP as the conjugate, that binds the analyte of interest, but employing more complex detection schemes [90]. One of these is the use of strip-readers, in which the color signal on test strips is converted into optical density, making results quantifiable when the ratio between test line and control line signal is considered [107]. Other groups reported the decoration of other materials with gold, such as magnetic Fe_2O_3 particles [108] or silica nanorods [109], and therefore enhancing the sensitivity of standard AuNP-based assays. Other reports also presented the enhancement of AuNP with further deposition of gold [110, 111] or silver [112], as well as incubation and binding with a second AuNP population with specific antibodies for a protein bound to those conjugates that capture the analyte of interest [113]. Apart from gold, other colored nanoparticles for the visual read-out of test results have been described in literature [90, 91]. These labels are for example selenium nanoparticles, giving a rust-colored signal. Despite a similar ease of application compared to gold, the LoD with selenium labels only reached the mg to μg range [114, 115], making AuNP a more sensitive label due to its stronger color [91]. Another example are carbon nanoparticles with a high contrast, due to their black color on white background [90]. With these labels, the detection of amplified DNA was shown down to concentrations below the ng mL^{-1} range [116].

As the labels for visual evaluation mentioned above might be prone to subjective interpretation and in most cases do not allow for a quantitative read-out, more elaborate labelling and detection techniques have already been developed [117]. These modifications usually rely on the use of fluorescent particles, which allow for quantification of the signal, but therefore also require suitable equipment for the detection of results [117]. One example of fluorescent particles are the so-called quantum dots (QDs): semiconductor crystals with sizes of a few nm, which exhibit a size-dependent narrow fluorescence spectrum, a broad excitation spectrum and low

photo-bleaching [118]. These QDs were shown to decrease the LoD by around 10-fold in comparison to AuNP as the standard, when conjugated with aptamers for the detection of pathogen-DNA [119]. Conjugation of QDs with specific antibodies for the detection of the antibiotic chloramphenicol also revealed sensitivity and quantitative results below the ng mL^{-1} range [120, 121]. Despite these promising optical properties and assay times comparable to those using AuNP, the flow behavior and stability of QDs in contact with biological matrices might be altered and their small size allows the attachment of only few recognition molecules [91, 90]. Hence, several groups have developed strategies for the encapsulation of QDs or tested their coupling to other beads. To do so, the group of Xiong used a microemulsion technique to formulate QDs inside a poly(methyl methacrylate) (PMMA) shell, thereby reaching higher sensitivity than with AuNP. However, in these reports, the achieved LoD was not compared to that of free QDs [122, 123]. Bai *et al.* covalently attached QDs to silica particles instead to achieve increased performance. In doing so, the detection limit for the tumor marker α -fetoprotein could be decreased by one order of magnitude, compared to AuNP. Again, no comparison of conjugated and free QDs was performed [124].

Another class of fluorescent nanoparticles are those comprising elements of the lanthanide series, mostly europium (Eu) or terbium (Tb), which also possess a sharp emission spectrum, a large Stokes shift and long fluorescence lifetimes [90]. These metal ions — as stable dyes — are commonly incorporated in other nanoparticles in the form of chelates and were shown to allow for highly sensitive detection. In this respect, Juntunen *et al.* presented a systematic comparison between standard AuNP and nanoparticles containing Eu^{3+} chelates for the detection of PSA as a model analyte with clinical relevance and the binding between streptavidin and biotin conjugated with bovine serum albumin (BSA), as a reference standard for the binding of recognition elements after conjugation to both labels [117]. Despite the fact that also the detection with AuNP was performed in a quantitative manner, i.e. by scanning strips and calculating grey scale values, the work showed that the detection of fluorescence signals of Eu^{3+} had a 3-fold higher signal-to-noise ratio (S/N ratio) [117]. Additionally, the long lived fluorescence of Eu^{3+} allows for time-resolved fluorescence (TRF) detection of signals and has been exploited in Juntunen's work. This technique is based on the fact that autofluorescence of materials or buffers and fluorescence of biological molecules is usually short-lived and the emitted signal decays within approximately 100 ns, whereas the fluorescence emission from complexed lanthanide ions can last up to 1000 μs [125, 126]. This fact

makes it possible to excite all fluorescent molecules in a sample by a laser pulse, but measure fluorescence signals only after a delay period, during which undesired signals have decayed and only that of the europium chelate persists [125]. Figure 2.8 gives a schematic representation of the TRF measurement technique.

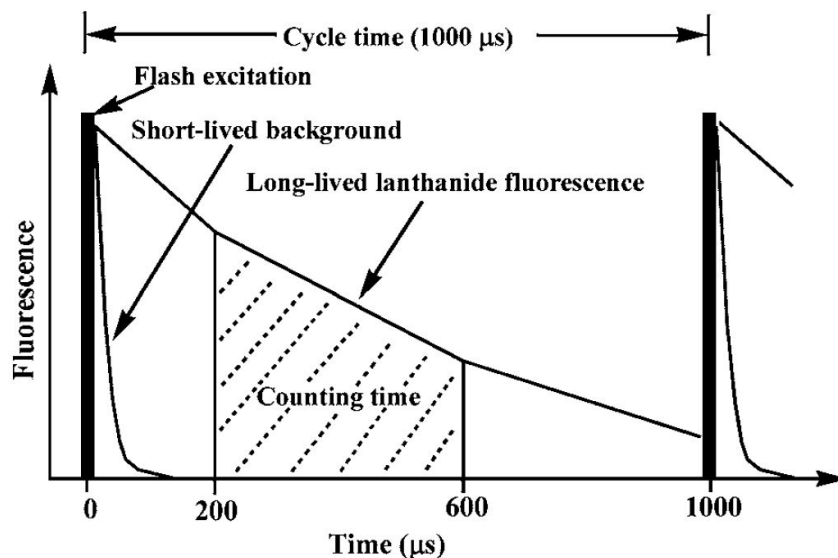


Figure 2.8 Measurement principle of TRF, in which all fluorescent molecules are initially excited by a short laser pulse. After excitation, short-lived background signal decays during the delay period, here 200 μs . Only then, fluorescence signal of the lanthanide chelates are detected during the counting time of the following 400 μs . Fluorophores may then be excited again during a new cycle, here 1000 μs after the first excitation. Figure taken from [127].

Employing TRF measurements, Juntunen showed that the S/N ratio could be increased over five times compared to the detection with AuNP and even around 80% in comparison to the direct detection of fluorescence signals from Eu^{3+} . At the same time, the LoD for PSA decreased by a factor of 5 and for the detection of biotinylated BSA even by a factor of 300, comparing the TRF measurement to AuNP [117]. Hence, the advantages of lanthanide complexes as fluorescent labels over conventional AuNP and even other fluorescent dyes with shorter fluorescence lifetimes become apparent.

Similarly sensitive assays using rare earth elements have also been developed with so-called up-converting phosphor (UCP) nanoparticles [90, 91]. These materials are crystals with sizes up to a few hundred nm, which can be doped with different pairs of lanthanides and are capable of absorbing light in the near infrared (NIR) range and emitting photons with energies of the visible range after up-conversion within the crystal. This process happens by one of the lanthanides absorbing NIR photons and transferring the excitation energy to the other dopant element through the crystal structure. Depending on the pair of lanthanides, two or three photons are transferred to the emitter ion, which then emits light in a narrow wavelength range to relax to the ground state [128, 129]. As up-conversion does not occur in nature, the use of these labels also omits background signal, leading to its high sensitivity [129, 130]. The group of Cooper were the first to introduce UCPs for the detection of hCG in LFAs [129], followed by Niedbala and colleagues employing these labels in LFAs for the detection of microorganisms and small molecules in 2001 [130]. Ever since then, more reports showed the application of UCP nanoparticles, for example by Zhao *et al.*, who reported a decrease in the LoD of marine pathogens by two orders of magnitude in comparison to an enzyme-linked immunosorbent assay (ELISA) [131].

As a last example of unconventional detection methods, the work by Tran *et al.* published this year should be mentioned, employing plasmonic nanoparticles (PNPs), made of gold-core/gold-satellite constructs with a Raman reporter molecule, as conjugates and a miniaturized surface-enhanced Raman scattering (SERS) reader for detection [132]. The use of Raman spectroscopy for LFAs had been reported before, but with high acquisition times — in the range of min, when sampling only parts of the test line — and complex instrumental requirements [133, 134], rendering the technique inappropriate for PoC testing [132]. Therefore, the use of line-illumination, combined with compact readers avoiding expensive Raman-detection set-ups by Tran and co-workers marked a step towards application of the approach in real-life scenarios [132]. The working principle is schematically depicted in figure 2.9, together with the line-illumination probe and the compact light source. The group chose hCG as a model target and compared their results to commercially available pregnancy tests, showing a decrease in the LoD by 15-fold within an acquisition time of 5 s [132]. However, the researchers measured only the test line within this scan time, where scanning the entire membrane appears useful to allow for example for normalization of signals at the test line with those from the control line. Still, the technique appears promising for the sensitive detection of targets, for which a decrease in the LoD cannot be achieved by using fluorescent dyes of particles.

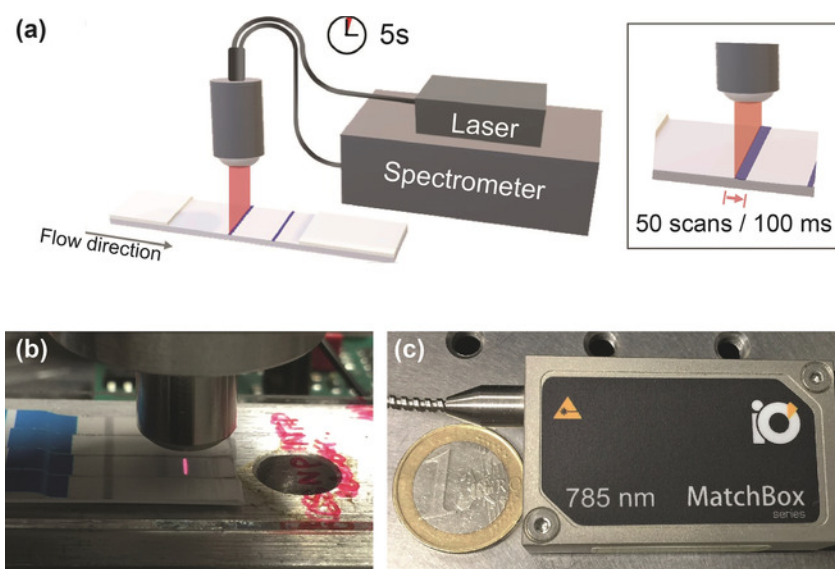


Figure 2.9 Working principle of the portable SERS reader and its components, as developed by Tran and co-workers. a) Schematic illustration of line illumination at the test line with a read-out time of 5 s, based on 50 scans with 100 ms acquisition time each. b) Photograph of custom-designed optical probe allowing for line illumination of test strips. c) Photograph of compact, portable diode laser as illumination source. Figure taken from [132].

2.4 Analysis of Extracellular Vesicles and their Content on Lateral Flow Platforms

Despite the discovery of numerous new potential biomarkers, for example for different cancer types, after screening the content of EVs [72, 70] and the advances made in creating LFAs with increasing sensitivity, as discussed above, there have been only few reports about using LFAs as the basis for EV analysis. The published data does not reach back more than three years and mostly focuses on the detection of EVs as such and their quantification [135, 136, 137]. In all these reports, the capture and detection of EVs was facilitated by targeting tetraspanins in the exosomal membrane — CD9, CD63 or CD81 —, which are easily accessible on intact EVs. In addition, the read-out was based on AuNP, giving rather high LoDs in the range of 1×10^8 to 1×10^9 particles per mL [135, 136]. However, Wu *et al.* coupled the detection with a second population of AuNP to enhance the signal of the first AuNP, targeting the tetraspanin CD9 in exosomal membranes. In this way, the LoD could be decreased to 1.3×10^6 particles per mL, which appears low when the high

abundance of approximately 1×10^{12} particles per mL plasma is considered [137]. At this time, only one publication investigated the presence of exosomal cargo on a LFA, which was MHC class I polypeptide-related sequence A (MICA) [138]. This protein is a biomarker for cancer and its level in serum correlates with the progression of tumors [139]. For the detection of MICA associated with EVs, López-Cobo *et al.* first captured the EVs with an anti-CD9 antibody and then detected MICA with a specific antibody-AuNP conjugate. The group could also show, that it was more advantageous to target the less abundant MICA for detection, compared to capturing EVs *via* MICA and detect these with conjugates targeting CD9. It was hypothesized that only in the described set-up steric hindrance of detection conjugates, bound during a pre-incubation step, could be circumvented to allow for the capture of EVs on the lateral flow strip [138]. These results show that LFAs also presented a suitable basis for the detection of cancer biomarkers of EVs. However, MICA is associated with a specific receptor of the exosomal membrane and therefore easily accessible to antibodies [140]. Hence, for cargo contained within EVs, analysis schemes will have to be developed in future research, that allow to isolate EVs from complex matrices by appropriate strip design, capture EVs *via* generic markers — such as the tetraspanins mentioned before — and perform their lysis on lateral flow strips to detect desired molecules in a last step. In that way, the scope of applications for LFAs may be broadened to facilitate the quick and sensitive detection of biomarkers from EVs.

3 Objective of this Thesis

In the course of this master thesis, different types of labels should be evaluated concerning their sensitivity for the detection of protein biomarkers in lateral flow assays. In this comparison the use of fluorescent lanthanide chelates and quantum dots, as well as Raman-active labels for highly sensitive and quantitative detection should be compared to gold nanoparticles, as the standard conjugate in current commercial solutions. One drawback of the visual read-out for gold nanoparticles by their characteristic colour is the fact that mostly qualitative results can be obtained. The use of lanthanide chelates, characterized by their long fluorescent life-times, or quantum dots with a high photo-stability overcomes this limitation. The same is true for labels that rely on the detection by surface-enhanced Raman scattering: using molecules with distinct and unique spectra — so called fingerprints —, low interference with the biological sample is possible during their detection. Another advantage of these alternatives to spherical gold nanoparticles should be the possibility for quantification of the detected analyte. This should be performed after specific antibodies are coupled to each label and the detectability of the conjugates in customized lateral flow assays is validated.

The molecule of interest for detection should be PTEN, a novel potential biomarker of prostate cancer, which has recently been identified in exosomes of tumor cells. As it was found, that its concentration in extracellular vesicles positively correlates with the progression of prostate cancer, the quantification of this protein in a quick and easy format seems of great importance to minimize invasive methods in prostate cancer surveillance and to make point-of-care analyses without complex instrumentation possible. After the proof-of-principle detection of PTEN solutions on lateral flow strips, these results should be transferred to more complex biological matrices, as encountered in clinically relevant applications: until today these are for example extracellular vesicle populations purified by ultracentrifugation or affinity chromatographic techniques. However, the scientific community has not implemented standard procedures for the diagnostic use of extracellular vesicles. Hence, such samples represent the most reliable sources for extracellular vesicle research.

At the end, it is thus desired to identify the most sensitive label for antibodies against PTEN, that allows for the detection at minute amounts within biological matrices, using lateral flow assays and a dedicated, yet affordable and compact detection system.

4 Materials and Methods

4.1 Instrumentation and Equipment

For the measurement of UV-Vis spectra in 96-well plates, a M200 Nanoquant spectrophotometer plate reader was used. The device was equipped with Quad4 MonochromatorTM optics and a 10 W, 40 Hz xenon flash lamp, allowing to scan a wavelength range of 230 nm to 1000 nm with 1 nm step width and bandwidth of 9 nm for > 315 nm and 5 nm for ≤ 315 nm, respectively.

For the read-out of AlphaLISA assays on 384-well microtiter plates, a Tecan Infinite M1000pro plate reader was used. Samples were in this case illuminated with a high power laser (750 mW) at 680 nm during an excitation time of 100 ms to release oxygen radicals from donor beads. The resulting chemiluminescence from acceptor beads was then detected at a wavelength of 615 nm during an integration time of 300 ms. Both devices were remotely controlled with i-controlTM software V.6 (all Tecan Group Ltd., Männedorf, Switzerland).

For dynamic light scattering (DLS) measurements, a Zetasizer Nano ZSP, equipped with a 633 nm He–Ne laser (10 mW laser power) and a detection angle of 173° for the intensity measurement of back-scattered light was used. The device was remotely controlled with Zetasizer Software (both Malvern Panalytical GmbH, Kassel, Germany). All measurements were performed in UV micro-cuvettes made of polystyrene for sample volumes of at least 70 μ L (BRAND GmbH + Co KG, Wertheim, Germany).

To record images of lateral flow strips, a Bio-Rad ChemiDoc MP system was used. Fluorescence signals from AlphaLISA beads were recorded using the **Ethidium Bromide** setting with UV trans illumination and a bandpass filter for 602 nm with 50 nm bandwidth, the exposure time was manually adjusted to 5 s. Lateral flow strips, in which AuNP were used, were imaged with the **colorimetric** setting of the instrument, the exposure time was automatically set by the system. Furthermore, the fluorescence signal from quantum dots was detected with the **Cy3** setting by excitation with a green LED and detection using the same band pass filter as in the **Ethidium Bromide** setting. Again, the exposure time was automatically set by the system. Data was recorded with the built in software and analyzed using Image LabTM software, version 6.0.1 (all Bio-Rad Laboratories GmbH, München, Germany).

Fluorescence signal intensities of AlphaLISA beads and QDs were additionally recorded by scanning lateral flow strip with an LRE CPoCLabFluo reader (LRE Medical GmbH, Munich, Germany as part of Esterline Technologies Corporation, Bellevue, WA, USA now Transdigm, Cleveland, OH, USA). The parameters used

for detection were an integration time of $T_{int} = 4160 \mu\text{s}$ and a waiting time of $T_{wait} = 20\,800 \mu\text{s}$.

To perform agarose gel electrophoresis of quantum dots, a PeqLab Perfect Blue gel system Mini S (VWR International GmbH, Darmstadt, Germany) was used and powered with a Consort EV261 Electrophoresis Power Supply (Consort bvba, Turnhout, Belgium).

The UV-Vis spectrum of gold nanostars before and after conjugation was recorded using a Jasco V-630 spectrophotometer (JASCO Deutschland GmbH, Pfungstadt, Germany). The absorption spectrum was recorded in a range from 400 nm to 1100 nm in steps of 0.5 nm against the respective buffer as the blank.

Lateral flow strips used with Raman-active gold conjugates were scanned with a custom-built miniaturized Raman-reader, as it is described in [132], with 1000 ms illumination time per line and 100 μm steps to measure the entire test line. A 785 nm laser was used with a power output of 150 mW. Additionally, a Bruker Senterra Raman Microscope (Bruker Corporation, Billerica, MA, USA) was used to detect the SERS signal at distinct spots of the test line of lateral flow strips with a 4 \times objective. The signal was measured upon irradiation with a 785 nm laser with 25 mW. The integration time per spot was 20 s in all cases. All measurements with Raman-active gold nanostars were performed by Vi Tran (Schlucker Group, University of Duisburg-Essen).

4.2 Chemicals and Consumables

AlphaLISA[®] Acceptor Beads (1 mg as 50 μL of 20 mg mL^{-1} suspension, lot#: 2424554), PTEN (human) AlphaLISA Detection Kit with 500 assay points (comprising acceptor beads with anti-PTEN antibodies and donor beads, biotinylated anti-PTEN antibody, as well as lyophilized PTEN, article no.: AL380C) and White Opaque OptiPlate 384-well microtiter plates made from polystyrene were purchased from PerkinElmer[®] (Rodgau, Germany).

NHS-Activated Gold Nanoparticle Conjugation Kit with 40 nm gold nanoparticles for the conjugation of three times 20 μg antibody (lot#: 2458582_40NHS) was purchased from CytoDiagnostics, Inc. (Burlington, Canada).

Human PTEN matched antibody pair kit (100 μL at 1 mg mL^{-1} capture antibody, 100 μL at 250 μg mL^{-1} detector antibody and 350 ng lyophilized human PTEN, lot#: GR288298-1, GR3273444-1 and GR3273444-2) and fluorescein isothiocyanate (FITC) Conjugation kit (for conjugation of 3 \times 10 μg antibody, lot#: GR3236492-13) were

purchased from abcam (Berlin, Germany).

SiteClick™ Qdot™ 625 Antibody Labelling Kit for the conjugation of 100 µg antibody with quantum dots (lot#: 2071568), Gibco® MEM Non-Essential Amino Acids Solution (100×), Fisherbrand™ disposable polyethersulfone bottle top filter with a pore size of 0.22 µm for vacuum filtration and PageRuler™ Plus Prestained Protein Ladder (Range: 10 kDa to 250 kDa) were purchased from Thermo Fisher Scientific, Life Technologies GmbH (Darmstadt, Germany).

Sodium cyanoborohydride (NaBH₃CN), *O*-(carboxymethyl)hydroxylamine hemihydrochloride (NH₂OCH₂COOH · ½HCl), Proclin™-300, 2-(*N*-morpholino)ethanesulfonic acid (MES) monohydrate (for molecular biology, purity ≥ 99.5 %), Tris(hydroxymethyl)aminomethane hydrochloride (Tris · HCl), cOmplete™ Mini tablets of protease inhibitor cocktail and Penicillin-Streptomycin (with 10,000 units penicillin and 10 mg streptomycin per mL in 0.9 % NaCl, sterile-filtered for cell culture) were purchased from Sigma-Aldrich (Munich, Germany).

Sodium hydroxide (NaOH) and 4-(2-hydroxyethyl)-1-piperazineethanesulfonic acid (HEPES) were purchased from AppliChem GmbH (Darmstadt, Germany).

Poly(ethylene glycol) (PEG)-4000, bovine serum albumin fraction V (protease-free, purity ≥ 98 %), Agarose standard (Roti® agarose for DNA/RNA electrophoresis) and Tween®-20 were purchased from Carl Roth GmbH + Co. KG (Karlsruhe, Germany).

RPMI 1640 cell culture medium with stable glutamine and 2.0 g L⁻¹ NaHCO₃ (catalog-no.: FG1215) for culturing human prostate carcinoma epithelial cell line 22Rv1 (DSMZ no.: ACC 438) and human immortalized prostate epithelial cell line PNT1a (ECACC no.: 95012614) was purchased from Biochrom GmbH (Berlin, Germany).

Centricon Plus-70 centrifugal filter units with a molecular weight cut-off (MWCO) of 100 kDa for concentration of up to 70 mL aqueous samples were purchased from Merck Millipore (Merck KGaA, Darmstadt, Germany).

White Cellstar® 96-well microplates with flat bottom for running samples in LFAs, transparent Cellstar® 96-well microplates with flat bottom for absorption measurements on a Tecan M200 Nanoquant and transparent Cellstar® 24-well multiwell plates for dot blot assays with quantum dots were purchased from Greiner Bio-One International GmbH (Kremsmünster, Austria).

Amersham Protran nitrocellulose Western Blotting membrane with a pore size of 0.2 µm was purchased from GE Healthcare Europe GmbH (Freiburg, Germany).

Goat anti-rabbit IgG, conjugated with horseradish peroxidase was purchased from dianova GmbH (Hamburg, Germany).

Clarity Western ECL Substrate for chemiluminescence detections using an HRP-conjugated secondary antibody was purchased from Bio-Rad Laboratories GmbH (München, Germany).

Lateral flow dip sticks (DetectLine Basic or DetectLine Basis *plus*) were purchased from AMODIA Bioservice GmbH (Braunschweig, Germany). The conjugates contained in the conjugate pad of both strip types target fluorescein. The only test line of DetectLine Basic strips binds biotin for the detection of double-labelled molecules. DetectLine Basic *plus* strips have an additional test line, binding molecules that are double-labelled with digoxigenin and fluorescein.

4.3 Conjugation of AlphaLISA Acceptor Beads with anti-PTEN Antibody

For the conjugation of purchased capture antibodies against human PTEN with AlphaLISA acceptor beads, a protocol from the supplier of the latter was used. A simplified reaction scheme is depicted in the appendix, figure 8.1. Following the recommended procedure, to 50 μL supplied bead suspension, 50 μL phosphate-buffered saline (PBS) were added in a reaction tube and the mixture was spun down for 15 min at $16\,000 \times \text{isg}$ to pellet the beads. The supernatant was carefully removed with a pipette. To the resulting pellet, 100 μg antibody (100 μL at a concentration of 1 mg mL^{-1}) were added, as well as 88.75 μL 4-(2-hydroxyethyl)-1-piperazineethanesulfonic acid (HEPES) buffer at pH 7.4, 1.25 μL of a 10 % Tween-20 solution and 10 μL of a freshly prepared 400 mM solution NaBH_3CN in water. The resulting mixture with a total volume of 200 μL was incubated for approximately 22 h at 37°C and 200 rpm in a thermo shaker under light protection. After the coupling step, unoccupied sites on AlphaLISA beads were blocked by the addition of 10 μL of a 65 mg mL^{-1} solution of carboxymethoxylamine ($\text{NH}_2\text{OCH}_2\text{COOH} \cdot \frac{1}{2}\text{HCl}$) in 800 mM NaOH to the reaction mixture and incubation at 37°C and 200 rpm for 1 h. The conjugated beads were subsequently washed by pelleting at $16\,000 \times \text{isg}$ and 4°C for 15 min and removal of the supernatant. The beads were then resuspended in 200 μL of 100 mM Tris \cdot HCl buffer at pH 8.0 and sonicated with 10 pulses of 1 s using a probe sonicator at 10 % maximum power. The beads were again centrifuged, resuspended in fresh Tris \cdot HCl buffer and sonicated with the same parameters. Then, the conjugated beads were centrifuged again at $16\,000 \times \text{isg}$ and 4°C for 15 min, but resuspended in 200 μL PBS with 0.05 % Proclin-300 as the storage medium. After a last sonication step as before, the beads were transferred to an opaque reaction tube and stored at 4°C until further use.

4.4 Conjugation of Gold Nanoparticles with anti-PTEN Antibody

The conjugation protocol for anti-PTEN capture antibodies with AuNP was performed as indicated by the manufacturer with slight modifications as follows: The purchased antibody solution was diluted 1:2 with supplied protein resuspension buffer, to obtain a concentration of 0.5 mg mL^{-1} by adding 25 μL antibody solution to 25 μL buffer. Lyophilized AuNP were reconstituted in 50 μL of supplied reaction buffer and 5 μL were removed and immediately diluted in 95 μL reaction buffer as an unconjugated control with final $OD = 2$. Subsequently, 40 μL of the antibody dilution were transferred to the tube containing reconstituted AuNP. The conjugation reaction was then allowed to progress during 3 h at room temperature. At the end of incubation, 10 μL of a supplied quencher solution were added to stop the reaction. The final conjugate was then pelleted by centrifugation at $900 \times g$ for 30 min and the supernatant was removed. The pellet was resuspended in 90 μL storage buffer (20 mM Tris · HCl at pH 8.0, 150 mM NaCl, 1 wt % BSA and 0.025 wt % Tween-20), giving an optical density of $OD = 20$ according to the manufacturer, and stored at 4°C until further use.

4.5 Conjugation of anti-PTEN Antibody with FITC

Capture antibodies against PTEN were conjugated to FITC to allow for the use of AuNP contained in the conjugate pad of lateral flow strips, which are coupled to anti-fluorescein antibodies. For conjugation, the manufacturer's protocol was followed. For the labelling reaction, 10 μL capture antibody solution (in PBS with 0.02 wt % sodium azide) at a concentration of 1.0 mg mL^{-1} were used. To this volume, 1.0 μL of the supplied Modifier reagent were added. The entire volume was then transferred to a vial containing the lyophilized FITC reagent and the reagents were mixed by gently pipetting up and down. The conjugation reaction was then allowed to proceed at room temperature (RT) for 3 h under protection from light. After incubation, 1.0 μL Quencher reagent was added to the reaction mixture and allowed to inactivate unconjugated dye molecules within 30 min. Thereafter, the conjugated antibody was ready to use and was stored at 4°C .

4.6 Conjugation of AuNS with anti-PTEN Antibody

Gold nanostars (AuNS) with hydrophilically stable PEG-coating and 4-nitrothiobenzoic acid (4-NTB) as the Raman-reporter molecule were kindly synthesized and conjugated with anti-PTEN antibodies using standard EDC/sNHS chemistry. The protocol

followed the procedure developed in the group of Prof. Dr. Schlücker and described by Schütz *et al.* [141], as it is summarized in the appendix, figure 8.2. The success of conjugation was verified by dispensing Protein A onto nitrocellulose membranes and running samples of the conjugation reaction product in lateral flow assays. The conjugation was confirmed by the formation of a visible signal at the test line, as well as by measuring Raman signals of the conjugated AuNS at six points of the test line and outside the test line with a Bruker Senterra Raman microscope. The conduction of these experiments by Vi Tran (Schlücker Group, University of Duisburg-Essen) is highly acknowledged.

4.7 Conjugation of anti-PTEN Antibody with Quantum Dots

For the conjugation of anti-PTEN capture antibodies with quantum dots, having an emission wavelength of $\lambda = 625$ nm, the instructions supplied by the manufacturer were used. A simplified scheme of the reaction is shown in figure 8.3 of the appendix. Following these, the PBS storage solution of the antibody was first exchanged against antibody concentration buffer, thereby increasing the antibody concentration and removing sodium azide. To do so, 100 μ L of the antibody solution were transferred to the supplied spin filter unit, previously washed with ddH₂O, giving 100 μ g of antibody. This volume was diluted to 500 μ L by the addition of 400 μ L antibody preparation buffer. Subsequently, the volume was reduced by centrifuging the spin filter at $5000 \times \text{isg}$ for 6 min. Again, 450 μ L antibody preparation buffer were added to the concentrate and it was centrifuged with the same parameters to yield a final volume of approximately 50 μ L. This volume was collected by inverting the filter unit in a fresh tube and centrifuging at $1000 \times \text{isg}$ for 3 min. The carbohydrate chains of the glycosylated Fc region of the prepared antibodies were then modified by the addition of 10 μ L β -galactosidase solution and incubation at 37 °C of 4 h. After incubation, the following components were added to the vessel containing UDP-GalNAz as the azide carrying sugar moiety: 75 μ L ddH₂O, 10 μ L of supplied 20 \times Tris buffer, pH 7.0, 25 μ L supplied buffer additive and 80 μ L of β -1,4-galactosyltransferase solution. The components were mixed by vortexing and the prepared antibody solution was added to the vial. The coupling of the azide modified sugar moiety was allowed to proceed over night (o/n) at 30 °C. After incubation, the reaction mixture was transferred to a large antibody concentrator unit and 1.75 mL 1 \times Tris buffer at pH 7.0, prepared from the supplied 20 \times stock, were added. The concentrator was centrifuged for 6 min at $1200 \times \text{isg}$ to reduce the volume. Then two more washing steps followed, adding

1.8 mL $1\times$ Tris buffer, pH 7.0 to the filter and centrifuging for 10 min at $1200\times$ *isg*, respectively. In the final washing step, 1.8 mL $1\times$ Tris buffer, pH 7.0 were added and the concentrator was centrifuged for 10 min at $1200\times$ *isg* to give a final volume of approximately 100 μ L concentrate. This volume was recovered by inverting the filter unit into the collection tube and centrifuging at $1000\times$ *isg* for 3 min. Until the conjugation with quantum dots, the thus modified antibodies were stored at 4 °C.

For the conjugation reaction, 50 μ L of dibenzocyclooctyne (DIBO)-modified quantum dot suspension were added to azide-functionalized antibody solution. The mixture was briefly vortexed, collected at the bottom of the vial and incubated o/n at 25 °C. Then, the reaction mixture was purified using a purification concentrator, which had been washed with ddH₂O. To do so, the entire reaction volume was applied on the filter and PBS was added to adjust the volume to 500 μ L. Quantum dots and antibodies that were not conjugated were separated by centrifugation at $1500\times$ *isg* for 10 min, followed by two additional washing steps, adding 500 μ L PBS and centrifuging with the same parameters. The now purified solution of antibody-QD conjugate (200 μ L) was removed from the filter membrane and transferred to an opaque vial for light protection and stored at 4 °C until use.

4.8 DLS Measurements of Nanoparticles Suspensions

To perform DLS measurements of AlphaLISA acceptor beads purchased with conjugated anti-PTEN antibody and those conjugated to the antibody in-house, the stock suspensions were diluted to a final concentration of 0.01 mg mL⁻¹ in PBS. To do so, 0.5 μ L of the stocks (5 mg mL⁻¹, respectively) were first added to 4.5 μ L PBS, then 2.0 μ L of this dilution were transferred to 98 μ L PBS, giving a final 1:500 dilution. The entire volume of 100 μ L was then transferred to polystyrene micro-cuvettes for measurements. Each sample was measured at 25 °C for a total of three times, during which 15 runs with an acquisition time of 10 s were binned, respectively. Z-average hydrodynamic diameter, size average and polydispersity index (PDI) for each sample were calculated automatically in the measurement software and the average size by intensity is reported for each sample.

AuNP for the conjugation with anti-PTEN antibody were measured at a concentration of $OD = 1$ after dilution with storage buffer in a volume of 100 μ L, using polystyrene micro-cuvettes. Again, samples were measured at 25 °C. However, five repeated measurements were performed, during which 15 runs with an acquisition time of 10 s were binned, respectively. Z-average hydrodynamic diameter, size average

and PDI for each sample were calculated automatically in the measurement software. For these samples, the average size by intensity had to be considered due to the high abundance of BSA in the storage buffer.

AuNS before conjugation were measured at an $OD = 0.08$ after dilution in PBS. Conjugated AuNS were measured at an $OD = 0.8$ in PBS with 2% BSA as the storage buffer. Both samples were measured in polystyrene micro-cuvettes at a temperature of 25 °C. Each sample was measured three times with 15 runs of 10 s acquisition time. The Z-average hydrodynamic diameter, the PDI, the average size by intensity and its standard deviation (SD) were calculated by the software automatically.

For the measurement of QDs, unconjugated samples were diluted 1:200 in Tris buffer pH 7.0, whereas samples after conjugation were used in a 1:50 dilution of the reaction product in the same buffer. Both samples were measured in micro-cuvettes at a temperature of 25 °C. For each sample, three measurements were performed with 15 runs of 10 s acquisition time. Again, the Z-average hydrodynamic diameter, the average size by intensity together with its SD and the PDI were calculated by the software automatically.

4.9 Absorption Measurements of Gold Nanoparticles for Conjugation with anti-PTEN Antibody

Absorption spectra of gold nanoparticles were recorded on a Tecan M200 Nanoquant both before and after conjugation to the anti-PTEN antibody at a concentration of $OD = 1$, corresponding to approximately 7.2×10^{10} particles mL^{-1} according to the manufacturer. To do so, AuNP were diluted in storage buffer (20 mM Tris · HCl at pH 8.0, 150 mM NaCl, 1 wt% BSA and 0.025 wt% Tween-20) and 50 μL were transferred to wells of a 96-well plate, together with the same volume of the storage buffer as the blank. Subsequently, the absorption of the conjugated particles was recorded over a range of 350 nm to 800 nm. All measurements were carried out in triplicate and average values of three blank measurements using storage buffer were subtracted from the results of each sample. The absorption values were then normalized to give a value at the absorption maximum of $Abs_{max} = 1$ and the absorption spectrum is reported as the average of all three samples.

4.10 Absorption Measurement of Gold Nanoparticles from Conjugate Pad

To determine the size of AuNP contained in the conjugate pad of commercial lateral flow strips, the particles first had to be recovered. To do so, the conjugate pad of

a single strip was removed and immersed in 350 μL ddH₂O to elute the particles. Of the obtained AuNP solution, 100 μL were transferred to wells of a 96-well plate. Additionally, the same volume of pure ddH₂O was measured to obtain the blank value. The absorption was recorded over a range of 350 nm to 800 nm on a Tecan M200 Nanoquant. All measurements were carried out in triplicate and average values of three blank measurements were subtracted from the absorption values of eluted AuNP. The absorption values were then normalized to give a value at the absorption maximum of $Ab_{s_{max}} = 1$ and the absorption spectrum is reported as the average of all three samples.

4.11 Absorption Measurement of Gold Nanostars for Conjugation with anti-PTEN Antibody

The absorption spectra of unconjugated and conjugated AuNS were measured as an indication for successful conjugation of the antibody. For the unconjugated AuNS this was done for a sample with an $OD = 0.8$ in 10 mM 2-(*N*-morpholino)ethanesulfonic acid (MES) buffer. The conjugated AuNS were measured at an $OD = 0.5$ in PBS. The measured volumes were approximately 800 μL , together with the same volume of the respective buffer as a blank. The absorption was recorded over a range of 400 nm to 1100 nm in 0.5 nm steps on a Jasco V-630 spectrophotometer. The absorption values of either AuNS sample were then normalized to give a value at the absorption maximum of $Ab_{s_{max}} = 1$.

4.12 Absorption Measurements of Quantum Dots

Absorption spectra of QD before and after conjugation to the anti-PTEN antibody were recorded on a Tecan M200 Nanoquant after dilution in the respective buffers. For unconjugated QDs this was in Tris buffer, pH 7.0 to a final dilution of 1:50, for QDs after conjugation PBS was used to dilute the reaction product 1:12.5, resulting in a similar final dilution due the approximate 1:4 dilution in the reaction mixture. Of each sample, 50 μL were transferred to wells of a 96-well plate, together with the same volume of the respective buffer as blanks. Subsequently, the absorption of QDs was recorded over a range of 350 nm to 800 nm. All measurements were carried out in triplicate and average values of three blank measurements were used to correct the absorption values of each sample. Again, the absorption values were normalized to give a value at the absorption maximum of $Ab_{s_{max}} = 1$ and the absorption spectrum is reported as the average of all three samples.

4.13 Production of concentrated Cell Culture Medium

To evaluate the matrix effect for the detection of PTEN on lateral flow strips, RPMI 1640, supplemented with 1 % non-essential amino acid solution (100×) and 1 % penicillin-streptomycin solution was concentrated to be used as the diluent of PTEN. To do so, approximately 200 mL of the medium were first filtered through a bottle top filter with 0.22 μm pore size using vacuum. The collected medium was then transferred to Centricon filters with a MWCO of 100 kDa, previously washed with phosphate-buffered saline with 0.1 % Tween-20 (PBS-T), and concentrated by centrifugation for 10 min at 3500 × *isg*. After concentration of the entire volume, the filter units were inverted onto collection reservoirs and the concentrate was recovered by centrifuging for 2 min at 1000 × *isg*. The volume of the recovered concentrate was estimated using a micropipette, giving approximately 365 μL and hence a concentration factor of approximately 560×, based on the starting volume. The recovered concentrated medium was distributed to 70 μL aliquots and stored at −80 °C until use. For use, the concentration factor was adjusted with PBS to result in the range obtained in EV samples.

4.14 LFA with Fluorescent AlphaLISA Bead Conjugates

4.14.1 General Assay Scheme for the Detection of PTEN in Solution

In general, purified PTEN in solution was detected in samples of 50 μL volume. To prepare these, first mixes of the biotinylated antibody and the antibody conjugate were prepared, using 0.1 μL antibody-conjugated bead suspension (50 ng or 333 fmol antibody, immobilized on 0.5 μg beads), 0.03 μL biotinylated antibody (corresponding to 7.5 ng or 50 fmol) and 4.87 μL AlphaLISA assay buffer, supplemented with a final concentration of 2.0 % PEG-4000, per sample. The resulting volume of 5.0 μL antibody mix per sample was then transferred to a reaction tube and 5.0 μL of a PTEN dilution with known concentration were added. To promote binding of the analyte, the mixture was incubated for a period of 5 h with shaking (750 rpm) and protection from light at RT. Subsequently, 40 μL assay buffer were added to each sample and the entire volume was transferred to a well of a 96-well plate. Then, lateral flow dip sticks, from which conjugate and sample pad had been removed, were inserted into the sample and allowed to take up the liquid within 18 min. Thereafter, the strips were directly analysed in an LRE CPoCLabFluo reader, using a signal integration time of $T_{int} = 4160 \mu\text{s}$ and a waiting time of $T_{wait} = 20\,800 \mu\text{s}$. The device scanned strips over a length of 38.7024 mm in steps of 0.0528 mm. As a control,

blanks were prepared by replacing the volume of the PTEN dilution with assay buffer and subsequently incubated and analyzed in the same manner.

Lateral flow strips were also imaged in a ChemiDoc MP system after drying. Images were acquired with the **Ethidium Bromide** setting, using 5 s exposure time. Signal intensities at the test line were determined using Lab View software.

4.14.2 Screening of Incubation Time for optimized Signal Intensity on Lateral Flow Strips

To identify the most suitable incubation time of analyte and antibody mixtures, the samples prepared as previously described (section 4.14.1) were incubated with shaking and light protection at RT for distinct intervals. Thereafter, they were used on lateral flow strips as before and directly analyzed with the LRE CPoCLabFluo reader. For each time point, additional blanks were prepared to exclude the possibility of unspecific binding events. Both samples and blanks were prepared in triplicates. Peak maxima of the test line region were used for the representation of signal evolution in samples and for blank correction. After plotting the blank corrected signal intensity against the incubation time, the data was fitted with a one-phase association model in GraphPad. Equation 1 represents the fitted function:

$$y = y_0 + (\text{Plateau} - y_0) \cdot (1 - e^{-K \cdot x}) \quad (1)$$

The variables of the equation are reported together with R^2 for the goodness of fit within the fitted curves.

4.14.3 Measurement of PTEN Standard Curves on Lateral Flow Strips

To record standard curves of PTEN, samples with known concentrations of PTEN were prepared and incubated as described in section 4.14.1. For the dilution of PTEN either AlphaLISA assay buffer with 2% PEG-4000 or concentrated medium was used. The concentrated medium was previously diluted 1:7 in PBS to results in a concentration factor of approximately 80 \times . In the case of concentrated medium, a part of the assay buffer was replaced by a volume of one seventh of the antibody master mix volume with a 7 \times protein inhibitor cocktail, prepared by dissolving one tablet of the formulation in 1.5 mL ddH₂O. The concentration range was from

$1.0 \times 10^{-7} \text{ g L}^{-1}$ to $1.0 \times 10^{-11} \text{ g L}^{-1}$ in the final sample volume, that was applied to the strips. The corresponding signal intensity maxima of the test line were used, when strips were scanned in the LRE CPoCLabFluo reader and signals of blanks were subtracted. For the analysis of images from the ChemiDoc MP system, bands were detected automatically within the central 2 mm along the strip to exclude edge effects and background was subtracted automatically by Lab View software. Thereafter, the signal was integrated over the width of the test line and used for plotting standard curves.

The signal intensity was plotted against the decadic logarithm of PTEN concentration and fitted with a 4-parameter logistics curve in GraphPad. Equation 2 was used for fitting:

$$y = \text{bottom} + \frac{\text{top} - \text{bottom}}{1 + 10^{(\log / C_{50-x}) \cdot \text{HillSlope}}} \quad (2)$$

The variables of the equation are reported together with R^2 for the goodness of fit within the calibration curves.

4.14.4 Spike-and-Recovery Evaluation of PTEN on Lateral Flow Strips

The recovery of PTEN was assessed in spiked samples of purified EVs from the 22Rv1 cell line as the biological matrix based on the signal from AlphaLISA beads conjugated to anti-PTEN antibody. This cell line was shown to be positive for PTEN in EVs. The EVs were concentrated and purified using either ultra-filtration (concentration factor: $79\times$) or ultra-centrifugation. Samples were characterized by nanoparticle tracking analysis, as depicted in the appendix, figure 8.19 and 8.20 and kindly provided by Susann Allelein (Fraunhofer IZI, Microdiagnostics Group). The EV samples were divided into 4 aliquots of $18 \mu\text{L}$ volume to which $2 \mu\text{L}$ of a known PTEN dilution were added to achieve an added volume $\leq 10\%$, according to [142]. The dilutions were prepared in ddH₂O and had concentrations of $3.5 \times 10^{-6} \text{ g mL}^{-1}$, $3.5 \times 10^{-7} \text{ g mL}^{-1}$ and $3.5 \times 10^{-8} \text{ g mL}^{-1}$, hence resulting in concentrations of $3.5 \times 10^{-7} \text{ g mL}^{-1}$, $3.5 \times 10^{-8} \text{ g mL}^{-1}$ and $3.5 \times 10^{-9} \text{ g mL}^{-1}$ upon 1:10 dilution in EV samples. Additionally, a blank was prepared by replacing the PTEN dilution with ddH₂O. Of these spiked samples, $5 \mu\text{L}$ were mixed with $5 \mu\text{L}$ of antibody mix in triplicates, as described in section 4.14.1. Incubation and analysis of the strips using an LRE CPoCLabFluo was also performed as in section 4.14.1.

Hence, measured PTEN concentrations were $10\times$ lower than that of the spiked EV samples due to dilution after incubation. The concentration of PTEN was calculated from the obtained signal intensity at the test line using the previously obtained standard curves, prepared in concentrated medium or AlphaLISA assay buffer with 2% PEG-4000. After subtraction of the blank values, the measured PTEN concentration was compared to the known amount of PTEN used for spiking each sample. The same experiment was performed using PTEN-negative EV samples from PNT1a cells. The samples were purified by ultra-filtration (concentration factor: $72\times$) and kindly provided by Susann Allelein again. The size characterization of this sample is shown in the appendix, figure 8.21. The recovery is reported as the mean of these values in %, together with the coefficient of variation (CV) for each concentration.

4.15 Standard Protocol for AlphaLISA Assay on Microtiter Plates

As the AlphaLISA assay was developed for use on microtiter plates, these experiments were conducted as the standard procedure, serving as a comparison to the approach transferred to lateral flow strips. A schematic representation of the assay principle is depicted in the appendix, figure 8.4.

4.15.1 Determination of Standard Curves

Again, a mix of antibodies was prepared first, as it is described for the general assay scheme for lateral flow assays in section 4.14.1, but replacing buffer with one seventh of the total volume by $7\times$ protease inhibitor cocktail. Of this mix, $5\ \mu\text{L}$ were transferred to a well of a 384-well OptiPlate for each sample. PTEN was diluted in concentrated medium, which was previously diluted 1:7 in PBS to a concentration factor of $80\times$, to obtain final concentrations in samples in a range from $1.0 \times 10^{-7}\ \text{g L}^{-1}$ to $1.0 \times 10^{-11}\ \text{g L}^{-1}$. Of the respective dilutions, $5\ \mu\text{L}$ were added to each well and mixed by pipetting up and down. In blanks, the PTEN dilution was replaced by concentrated medium only. After collecting the reaction mixture at the bottom of the plate by a short centrifugation, the samples were incubated either 1 h as the standard incubation time or 5 h as for LFAs at RT with shaking and light protection. After incubation, $40\ \mu\text{L}$ of a mix containing $39.6\ \mu\text{L}$ AlphaLISA assay buffer and $0.4\ \mu\text{L}$ of the donor bead suspension per sample, were added to each sample. The solutions were again mixed well by pipetting up and down and collected at the plate bottom by a short centrifugation. Donor beads, binding the biotinylated

anti-PTEN antibody were then allowed to incubate for 1 h at RT with shaking and light protection in both cases. Thereafter, the chemiluminescence intensity of Eu^{3+} chelates resulting from reactive oxygen species produced by donor beads upon excitation at a wavelength of 680 nm was immediately recorded on a Tecan Infinite M1000pro plate reader, using the AlphaLISA setting with 100 ms excitation time and 300 ms integration time. For both incubation times, samples of each PTEN concentration were prepared in triplicates, while four samples of the blanks were prepared in triplicate, respectively. After subtraction of blank values, the standard curves were calculated as described above and fitted using equation 2.

4.15.2 Spike-and-Recovery Experiments from EV samples

The same EV samples from 22Rv1 cells as employed in spike-and-recovery experiments with the LFA were used, which were enriched by ultra-filtration (concentration factor: $79\times$, figure 8.19) or ultra-centrifugation (figure 8.20), respectively. The EV samples were divided into 4 aliquots of 18 μL volume again and 2 μL of a known PTEN dilution were added. The dilutions were prepared in ddH₂O and had concentrations of $3.5 \times 10^{-6} \text{ g mL}^{-1}$, $3.5 \times 10^{-7} \text{ g mL}^{-1}$ and $3.5 \times 10^{-8} \text{ g mL}^{-1}$, hence resulting in concentrations of $3.5 \times 10^{-7} \text{ g mL}^{-1}$, $3.5 \times 10^{-8} \text{ g mL}^{-1}$ and $3.5 \times 10^{-9} \text{ g mL}^{-1}$ upon 1:10 dilution in EV samples. A blank was prepared by replacing the PTEN dilution with ddH₂O. The same concentrations of PTEN and the blank were prepared in concentrated medium, diluted 1:7 to a concentration factor of $80\times$, to serve as the internal control. After 5 μL of the antibody mix, prepared as in section 4.15.1 with protease inhibitor, was transferred to each well of a 384-well OptiPlate, 5 μL of the spiked EV samples were added. The liquid was thereafter collected at the plate bottom by short centrifugation and incubated for 5 h at RT on a shaking plate and protected from light. After the target was bound by AlphaLISA acceptor beads and biotinylated antibody, 40 μL of a donor bead dilution, containing 0.4 μL stock suspensions and 39.6 μL AlphaLISA assay buffer with 2.0 % PEG-4000 per sample, were added to each sample and mixed well. After a short centrifugation, the plate was again incubated for 1 h at RT with shaking and light protection to promote donor bead binding. Subsequently, the plate was immediately read on a Tecan M1000pro, using the AlphaLISA setting with 100 ms excitation time and 300 ms integration time. The blank values were subtracted from signal of PTEN-containing samples. Thereafter, the relative recovery was calculated with respect to the internal controls. The recovery is reported as the mean of three measurements and their CV.

4.16 LFA using AuNP Conjugates with different Antibodies

4.16.1 AuNP conjugated to anti-PTEN Antibodies

To test AuNP on lateral flow strips after conjugation to anti-PTEN capture antibodies as described in section 4.4, a protocol from Juntunen *et al.* [117] was modified as follows: Samples were prepared with 5 μL PTEN dilution at a concentration of $1 \times 10^{-6} \text{ mg mL}^{-1}$ to which 5 μL of antibody-conjugated AuNP ($OD = 20$, 1110 ng antibody) were added. Additionally, biotinylated antibody solution was added with a volume of 0.03 μL (7.5 ng) per sample or a 5-fold increased amount of 0.15 μL (37.5 ng) per sample. The volume was then adjusted to a total of 20 μL using AlphaLISA assay buffer with 2.0 % PEG-4000. The thus prepared samples had a final PTEN concentration of $2.5 \times 10^{-7} \text{ mg mL}^{-1}$ and AuNP density of $OD = 5$. For blanks, 5 μL PTEN dilution were replaced with the same volume of AlphaLISA assay buffer with 2.0 % PEG-4000. Incubation was subsequently carried out during 5 h as with AlphaLISA beads at RT and with shaking (750 rpm). After incubation, the sample volume of 20 μL was transferred to wells of a 96-well plate, into which lateral flow strips were immersed after removal of conjugate and sample pad. When the entire volume was taken up by the strips, these were transferred to wells, containing 100 μL AlphaLISA assay buffer with 2.0 % PEG-4000 to wash out unbound AuNP conjugates. Lateral flow strips remained inside the buffer until all conjugates were dislocated to the wicking pad and the membrane showed a white color again.

4.16.2 Use of AuNP from Lateral Flow Conjugate Pad with FITC-labelled anti-PTEN Antibodies

When FITC-targeting AuNP contained in the conjugate pad of lateral flow strips were used directly, anti-PTEN antibodies conjugated with FITC according to section 4.5 were employed. For the preparation of these samples, antibody mixes were prepared comprising 0.03 μL antibody-FITC conjugate solution at a concentration of 0.1 mg mL^{-1} (3 ng or 20 fmol capture antibody), 0.012 μL biotinylated antibody (corresponding to 3 ng or 20 fmol) and 4.89 μL AlphaLISA assay buffer per sample. Of this mix, 5 μL were transferred to a fresh reaction tube for each sample and 5 μL of PTEN dilutions with a known concentration were added. For blanks, PTEN was replaced by AlphaLISA assay buffer with 2.0 % PEG-4000. The samples and blanks prepared in this fashion were incubated for 2 h at RT with shaking (750 rpm) and light protection. Subsequently, the entire sample volume of 10 μL was transferred to the conjugate pad of lateral flow strips using a micropipette and allowed to incubate

for 3 min. To run strips, these were then immersed in 100 μL AlphaLISA assay buffer with 2.0 % PEG-4000 in wells of a 96-well plate. Lateral flow strips — in this set-up intact with sample and conjugate pad — were allowed to run for 20 min. The intensity of signals at the test and control line was assessed visually and by imaging on a ChemiDoc MP system.

4.16.3 Test of unspecific Antibody Binding at the Test Line of Lateral Flow Strips

To test if FITC-conjugated antibodies bind unspecifically at the test line of lateral flow strips, a Western Blot-like experiment was carried out. To prevent the interference with AuNP from the conjugate pad of test strips, the conjugate and sample pad were again removed from the strips. The binding behavior was assessed in samples, containing either 100 ng unconjugated or FITC-conjugated antibody in a volume of 20 μL . To do so, 1.0 μL of 0.1 mg mL^{-1} solutions of either antibody were diluted in 19 μL of AlphaLISA assay buffer with 2.0 % PEG-4000. These samples were transferred to wells of a 96-well plate and the modified lateral flow strips were immersed in the solution. After taking up samples, the strips were transferred to 100 μL assay buffer for 20 min to wash away unbound antibodies. The strips were then dried at RT for 15 min and subsequently immersed in a 5 % BSA solution, prepared in PBS, to block any unoccupied sites on the membrane. Strips were incubated in plastic boxes for 45 min at RT with shaking at 450 rpm. Thereafter, the strips were rinsed briefly with PBS-T. A 1:10000 dilution of an anti-rabbit secondary antibody, conjugated to horseradish peroxidase (HRP) was prepared by diluting 1.0 μL of the antibody solution in 10 mL of a 2.5 % BSA solution in PBS and added to the lateral flow strips. The secondary antibody was allowed to bind the unconjugated and FITC-labelled antibodies during 45 min incubation at RT with shaking at 450 rpm. After removal of the solution, the membrane was washed twice with PBS-T for 2 min and finally with PBS for 2 min. The covering plastic foil was removed from the strips to allow the substrate to reach the HRP-conjugate more easily. As the chemiluminescent substrate, 6.0 mL of a solution containing 0.2 mM *p*-coumaric acid and 1.25 mM Luminol in 100 mM Tris buffer, pH 8.5 and 18 μL of a 3 % H_2O_2 solution in dd H_2O were mixed and added to the strips. The strips were imaged using the ChemiDoc MP system with **auto optimal** exposure in the **chemiluminescence** mode at a binning of 1×1 pixel, resulting in an exposure time of 123.5 s.

4.17 Use of AuNS-Conjugates on Lateral Flow Strips

For AuNS-conjugates obtained according to section 4.6, the protocol reported by Juntunen *et al.* was again adapted [117]. Following this procedure, samples were prepared in a volume 20 μL , using 5 μL PTEN dilution, 0.03 μL biotinylated antibody (corresponding to 7.5 ng or 50 fmol), 4.97 μL AlphaLISA assay buffer with 2 % PEG-4000 and 10 μL AuNS-conjugates with an $OD = 8$ in PBS, hence resulting in a final $OD = 4$ in samples. The dilutions of PTEN were prepared in AlphaLISA assay buffer with 2 % PEG-4000 in a concentration range of $1 \times 10^{-6} \text{ g mL}^{-1}$ to $1 \times 10^{-10} \text{ g mL}^{-1}$, giving a final concentration range in samples from $2.5 \times 10^{-7} \text{ g mL}^{-1}$ to $2.5 \times 10^{-11} \text{ g mL}^{-1}$. Additionally, blanks were prepared by replacing PTEN dilution with 5 μL AlphaLISA assay buffer with 2 % PEG-4000. The thus prepared samples were incubated o/n (approximately 17 h) at 4 °C. Subsequently, the entire sample volume was transferred to wells of a 96-well plate and lateral flow strips were inserted into samples after removal of conjugate and sample pad. When the entire sample had been taken up by the strips, these were transferred to wells containing 50 μL AlphaLISA assay buffer with 2 % PEG-4000 to wash away unbound AuNS-conjugates. After the strips had dried in ambient conditions, these were analyzed using the Raman signal of the entire test line, which was accumulated using the spectrometer of a the custom-built Raman reader with line illumination [132]. For all samples except blanks, single measurements were performed. Hence, the LoD could again be calculated as $\text{LoD} = \text{blank average} + 3 \cdot SD$ after fitting data with the 4-parameter logistics function.

4.18 LFA using Conjugates of anti-PTEN Antibodies with Quantum Dots

For the use of QD-labelled antibodies against PTEN, conjugated as described in section 4.7, samples were prepared in a similar fashion as for the detection by fluorescent AlphaLISA bead conjugates in section 4.14.1. Hence, first a mix of antibodies was prepared, employing 0.1 μL of the QD-conjugated antibody with a concentration of approximately 0.5 mg mL^{-1} (50 ng or 333 fmol capture antibody), 0.03 μL biotinylated antibody (7.5 ng or 50 fmol) and 4.87 μL AlphaLISA assay buffer with 2 % PEG-4000 per sample. Of this master mix, 5 μL were transferred to fresh reaction tubes and mixed with 5 μL of a PTEN dilution with known concentration. The samples were then incubated for 5 h at RT with shaking at 750 rpm and light protection. For blanks, the volume of the PTEN dilution was replaced with 5 μL AlphaLISA assay buffer with 2.0 % PEG-4000. Otherwise, blanks were treated the

same as samples containing PTEN. After incubation, 40 μL AlphaLISA assay buffer with 2.0% PEG-4000 were added to each reaction tube and the entire volume was transferred to wells of a 96-well microtiter plate. After removal of the conjugate and sample pad, lateral flow strips were inserted into the wells and allowed to take up the entire sample during 18 min. Thereafter, the fluorescence signal from the strips was recorded using an LRE CPoCLabFluo reader with the same parameters as stated for AlphaLISA beads in section 4.14.1.

4.19 Testing the Running Behavior of QD-Conjugates on Lateral Flow Strips

To elucidate, if and in which buffers QDs after conjugation to anti-PTEN antibodies migrate on strips, the reaction product of the conjugation was diluted in different buffers. To do so, 1.0 μL of the stock suspension was first added to 4.0 μL PBS as the storage buffer, creating a 1:5 dilution. Of this dilution, 1.0 μL were transferred to 49 μL of either PBS or AlphaLISA assay buffer with 2% PEG-4000, respectively to obtain a final 1:250 dilution. The entire sample volume of 50 μL containing approximately 100 ng conjugated antibody based on input amount and final volume of the conjugation reaction was then transferred to wells of a 96-well microtiter plate. After removing the sample and conjugate pad from lateral flow strips, these were inserted into the wells and allowed to take up the entire sample. Subsequently, strips were imaged in a ChemiDoc MP system, using the DyLight550 setting with `auto optimal` exposure (0.918 s exposure time).

4.20 Dot Blot Assay with QD-Conjugates

A dot blot assay was chosen to assess, if the anti-PTEN antibody had been successfully conjugated to QDs using the manufacturer's protocol. In this experiment, a nitrocellulose membrane with 0.2 μm pore size was first cut into pieces to fit into wells of a 24-well plate. On these untreated membrane pieces, 0.5 μL of the PTEN stock solution — hence 1.75 ng — were spotted using a micropipette. The protein solution was allowed to dry on the membranes o/n at 4 $^{\circ}\text{C}$. Subsequently, unoccupied binding sites of the membranes were blocked by 60 min incubation with 500 μL of a 2% BSA solution in PBS per well on a shaking plate. Thereafter, membranes were washed three times with 300 μL PBS-T to remove unbound protein. To the blocked membranes, 300 μL of diluted unconjugated antibody or QD-conjugated antibody were added per well, respectively. To do so, the unconjugated antibody was diluted 1:2000 in AlphaLISA assay buffer with 2% PEG-4000 giving a final concentration

of $0.5 \mu\text{g mL}^{-1}$. Additionally, the reaction product of the conjugation with QDs was diluted 1:1000 in either AlphaLISA assay buffer with 2 % PEG-4000 or in PBS. Based on the employed amount of antibody for the conjugation reaction and the final volume, a final antibody concentration of approximately $0.5 \mu\text{g mL}^{-1}$ resulted for the incubation with the membranes. The antibodies were allowed to bind the target during 90 min incubation at RT and with shaking. After incubation, the membranes were again washed five times with 500 μL PBS-T to remove unbound antibodies. Then, a 1:5000 dilution of an anti-rabbit secondary antibody-HRP conjugate was prepared by adding 1.0 μL of the stock solution to 5 mL of a 2.5 % BSA solution in PBS-T. Of this dilution 500 μL were transferred per well and allowed to incubate for 60 min with the primary anti-PTEN antibody. Subsequently, the membranes were washed twice with 500 μL PBS-T and lastly once with the same volume of PBS. Commercial chemiluminescence substrate (Bio-Rad) was prepared by mixing equal parts (1.5 mL) of component A with the same volume of component B. Of the substrate 300 μL were transferred to each well, the plate was briefly shaken and directly imaged using a ChemiDoc MP system. Chemiluminescence signal was recorded using the **Chemiluminescence** setting with a binning of 1×1 pixel, while fluorescence from QDs was recorded using the **DyLight550** setting. In both channels, **auto optimal** exposure was chosen, resulting in 17.831 s exposure time for the fluorescence channel and 151.413 s exposure time for the chemiluminescence image.

4.21 Agarose Gel Electrophoresis of Quantum Dots

To differentiate conjugated from unconjugated QDs, agarose gel electrophoresis was performed, following a protocol by Meiner *et al.* [143]. Therefore, a 1.5 % agarose gel was prepared by adding 1.05 g agarose to 70 mL $1 \times$ Tris-acetate-EDTA (TAE) buffer. The mixture was heated using a microwave oven until full dissolution of the agarose was achieved. Then, 700 μL of a 10 % sodium dodecyl sulfate (SDS) solution were added to the solution directly before casting the gel, resulting in a final concentration of 0.1 % SDS. After casting, the gel was allowed to solidify by cooling to RT. To prepare samples, a 1:50 dilution in Tris buffer, pH 7.0 of supplied unconjugated, DIBO-modified QDs and a 1:15 dilution in Tris buffer, pH 7.0 of the reaction product after conjugation were used. These dilutions were mixed in the following proportions with $6 \times$ loading dye (LD), containing 375 mM Tris \cdot HCl buffer at pH 6.8, 12 % SDS, 60 % glycerol, 0.06 % bromophenol blue for non-reducing conditions and an additional 600 mM dithiothreitol (DTT) for reducing LD: For the unconjugated QDs 6 μL of the

dilution were mixed with 18 μ L reducing or non-reducing 6 \times LD, resulting in a final 1:200 dilution in samples. For the conjugation product 4 μ L of the dilutions were mixed with 20 μ L of either reducing or non-reducing 6 \times LD, giving final dilution of 1:90, respectively. The thus prepared samples were completely transferred to pockets of the agarose gel and additionally, 5 μ L of PageRuler Plus were applied to the gel as a reference for migration. The electrophoresis chamber was then filled with 1 \times TAE buffer, supplemented with a final concentration of 0.1% SDS. Subsequently, the agarose gel electrophoresis was performed with a constant potential of 80 V for 100 min. The gel was then imaged on a ChemiDoc MP system, using the Cy3 setting for the detection of QD signal with `auto optimal` image acquisition (exposure time: 24.843 s).

5 Results

5.1 DLS Measurements of Nanoparticle Suspensions

5.1.1 Hydrodynamic Diameters of AlphaLISA acceptor beads

Measuring the hydrodynamic diameter of AlphaLISA acceptor beads by DLS revealed that acceptor beads coupled to antibodies in-house showed a similar size and size distribution as acceptor beads, that were purchased with already coupled antibodies as part of a kit. In the case of acceptor beads, conjugated to purchased anti-PTEN antibodies, the Z-average values were as follows in the three measurements: I. 304.6 nm, II. 315.2 nm and III. 304.3 nm. The overall average size by intensity was calculated as $311.7 \text{ nm} \pm 8.61 \text{ nm}$ with a PDI of 0.081 ± 0.015 , indicating a narrow size distribution. The results for commercially available acceptor beads with coupled antibodies were similar, giving the following Z-average sizes, respectively: I. 288.2 nm, II. 286.0 nm and III. 292.2 nm. These results showed similar results with an average size by number of $294.4 \text{ nm} \pm 2.86 \text{ nm}$ and a PDI of 0.024 ± 0.025 . Still, a significant difference between both types of beads could be found using a two-sided *t*-test for unpaired sample ($p = 0.04329$). Table 1 gives an overview of the measured properties and size distributions of the respective measurements can be found in the appendix, figure 8.5 and figure 8.6.

Table 1 Average sizes by intensity and SDs, as well as PDI values for different measurements of AlphaLISA acceptor beads conjugated to anti-PTEN antibody and commercial AlphaLISA beads with already coupled antibodies. The overall average and SD of average sizes and PDIs are also indicated for each type of beads.

	conjugated beads			commercial beads			
measure- ment	average size [nm]	SD size [nm]	PDI	measure- ment	average size [nm]	SD size [nm]	PDI
I	306.0	48.77	0.074	I	291.7	34.87	0.002
II	321.6	75.97	0.098	II	297.4	63.88	0.052
III	307.5	48.23	0.070	III	294.1	34.28	0.019
average	311.7		0.081	average	294.4		0.024
SD	8.61		0.015	SD	2.86		0.025

5.1.2 Hydrodynamic Diameters of spherical Gold Nanoparticles

In the case of AuNP, the presence of BSA in storage buffer as the diluent for samples resulted in Z-average values that were smaller than the observed size averages by intensity, which were also considered for these nanoparticles. However, a significant difference between AuNP before and after conjugation could be found using a two-sided *t*-test for unpaired sample, when the average sizes by intensity were considered ($p = 0.000293$). The obtained Z-average values for unconjugated AuNP in the five measurements were: I. 61.35 nm, II. 61.13 nm, III. 62.11 nm, IV. 61.27 nm and V. 61.48 nm. The measurements of AuNP after conjugation revealed the following Z-average values: I. 71.29 nm, II. 71.27 nm III. 69.78 nm, IV. 71.12 nm and V. 71.37 nm. These values illustrate the low variability of the hydrodynamic diameters of AuNP, which is also represented by the overall average sizes by intensity, which were $76.25 \text{ nm} \pm 0.86 \text{ nm}$ and $91.03 \text{ nm} \pm 3.22 \text{ nm}$ for unconjugated and conjugated AuNP, respectively. The PDI hints at the fact that AuNP had a low variability in size. These were on average 0.223 ± 0.008 and 0.266 ± 0.005 for unconjugated and conjugated AuNP, respectively. Table 2 gives the obtained values for all five measurement per sample and the reported overall averages and SDs, as well as the PDIs. The size distributions of all five measurements of both samples, as well as their average distributions are given in the appendix, figures 8.7, 8.8, 8.9 and 8.10.

Table 2 Average sizes by intensity and SDs, as well as PDI values for different measurements of unconjugated and conjugated AuNP. The overall average and SD of average sizes and PDIs are also indicated for AuNP before and after conjugation.

measure- ment	unconjugated AuNP			conjugated AuNP			
	average size [nm]	SD size [nm]	PDI	measure- ment	average size [nm]	SD size [nm]	PDI
I	75.80	18.45	0.225	I	86.71	21.34	0.257
II	75.92	14.49	0.216	II	91.10	26.38	0.267
III	76.29	16.01	0.214	III	89.74	25.17	0.270
IV	77.70	18.05	0.227	IV	92.08	32.13	0.268
V	75.52	21.28	0.234	V	95.51	34.04	0.270
average	76.25		0.223	average	91.03		0.266
SD	0.859		0.008	SD	3.221		0.005

5.1.3 Hydrodynamic Diameters of Gold Nanostars

For AuNS, the determination of the hydrodynamic diameter revealed a significant difference between the particles before and after conjugation, using a two-sided t -test for unpaired sample, when the average sizes by intensity were considered ($p = 0.000232$). In addition, the AuNS population before conjugation showed the presence of smaller particles, as it is visible in figure 8.11 of the appendix. Therefore, the obtained Z-average values were slightly smaller than the hydrodynamic diameters of the AuNS themselves, giving values of I. 62.79 nm, II. 63.19 nm and III. 63.54 nm for the respective measurements. The average hydrodynamic diameter was however $72.48 \text{ nm} \pm 2.139 \text{ nm}$ and the PDI was measured as 0.232 ± 0.015 .

For AuNS that were conjugated to anti-PTEN antibodies the following Z-average values were measured: I. 78.38 nm, II. 77.51 nm and III. 78.14 nm. These results illustrate the low variability of the obtained values, which is also represented by the overall average sizes by intensity, which was $95.38 \text{ nm} \pm 2.298 \text{ nm}$. The PDI was on average 0.225 ± 0.009 for conjugated AuNS. Table 3 gives the obtained values for all three measurement per sample and the reported overall averages and SDs, as well as the PDIs. The size distributions of conjugated AuNS are also given in figure 8.12 of the appendix.

Table 3 Average sizes by intensity and SDs, as well as PDI values for different measurements of unconjugated and conjugated AuNS. The overall average and SD of average sizes and PDIs are also indicated for unconjugated and conjugated AuNS.

	unconjugated AuNS			conjugated AuNS			
measure- ment	average size [nm]	SD size [nm]	PDI	measure- ment	average size [nm]	SD size [nm]	PDI
I	72.07	16.58	0.217	I	96.70	30.35	0.216
II	74.79	17.75	0.232	II	96.72	38.45	0.225
III	70.57	21.67	0.246	III	92.73	28.26	0.234
average	72.48		0.232	average	95.38		0.225
SD	2.139		0.015	SD	2.298		0.009

5.1.4 Hydrodynamic Diameters of Quantum Dots

The measurement of QDs revealed unexpected results, as QDs after conjugation showed similar hydrodynamic diameters as those prior to conjugation. This size difference was not significant in a two-sided t -test for unpaired samples ($p = 0.4750$). As visible in figures 8.14 and 8.13 of the appendix, QDs before conjugation and after conjugation also showed very similar distribution of the size by intensity with the appearance of few aggregates. The Z-average values obtained for the three measurements of unconjugated QDs were I. 28.61 nm, II. 28.95 nm and III. 27.50 nm. Similar to these, the Z-average values from measurements of the conjugated QDs were I. 27.06 nm, II. 25.32 nm and III. 25.62 nm. Therefore, the Z-average values were slightly smaller than the measured average sizes, which were $31.38 \text{ nm} \pm 1.92 \text{ nm}$ for unconjugated QDs and $32.59 \text{ nm} \pm 1.853 \text{ nm}$ for conjugated QDs. The measured particles also showed low deviations in size, according to the PDI values, which were 0.244 ± 0.035 and 0.269 ± 0.022 for unconjugated and conjugated QDs, respectively. The values obtained in the measurement of the respective samples are summarized in table 4, together with the averages and SDs.

Table 4 Average sizes by intensity and SDs, as well as PDI values for different measurements of unconjugated and conjugated QDs, respectively. The overall average and SD of average sizes and PDIs are also indicated for both samples.

	unconjugated QDs			conjugated QDs			
measure- ment	average size [nm]	SD size [nm]	PDI	measure- ment	average size [nm]	SD size [nm]	PDI
I	31.65	10.78	0.229	I	34.66	13.64	0.244
II	29.34	9.88	0.284	II	31.08	11.36	0.284
III	33.15	12.28	0.220	III	32.04	10.89	0.279
average	31.38		0.244	average	32.59		0.269
SD	1.92		0.035	SD	1.853		0.022

5.2 UV-Vis Absorption Measurement of Nanoparticle Suspensions

5.2.1 Absorption Spectra of Gold Nanoparticles for Conjugation with anti-PTEN Antibodies

Evaluation of the absorption spectrum of AuNP showed an expected shape and absorption maximum of $Abs_{max} = 528$ nm, as reported by Haiss *et al.* for AuNP of 40 nm size [144]. Both unconjugated and conjugated AuNP showed only a single absorption peak in the tested wavelength range and very similar spectra overall, as seen in figure 5.1. It was observed, that the absorption maximum (Abs_{max}) shifted slightly from $\lambda = 528$ nm for unconjugated AuNP to $\lambda = 530$ nm after conjugation. This behavior was reported by the manufacturer upon conjugation due to an increase of the local refractive index at the surface of AuNP [145].

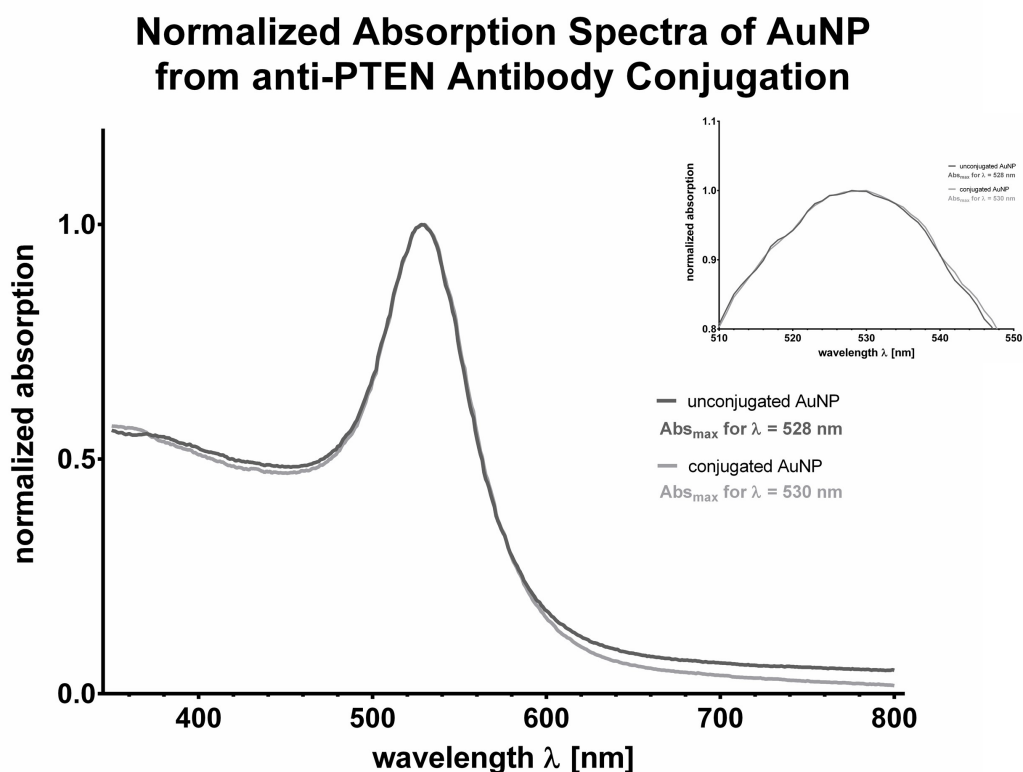


Figure 5.1 UV-Vis absorption spectra for AuNP before (dark grey line) and after conjugation (light grey line). The spectra were normalized to give a value of $Abs_{max} = 1$ at the indicated wavelength of the absorption peak. The inset figure visualizes the subtle change in the absorption maximum.

5.2.2 Absorption Spectrum of Gold Nanoparticles from Conjugate Pad

The absorption spectrum of AuNP from the conjugate pad of lateral flow strips was recorded to determine the size of the contained particles from the absorption maximum. As seen in figure 5.2, the AuNP had a similar absorption spectrum to that determined for AuNP conjugated to the anti-PTEN antibody directly (figure 5.1). However, in this case the absorption maximum was found at a wavelength of $\lambda = 532$ nm. According to Haiss *et al.* this absorption maximum corresponds to AuNP with a size of approximately 52 nm [144].

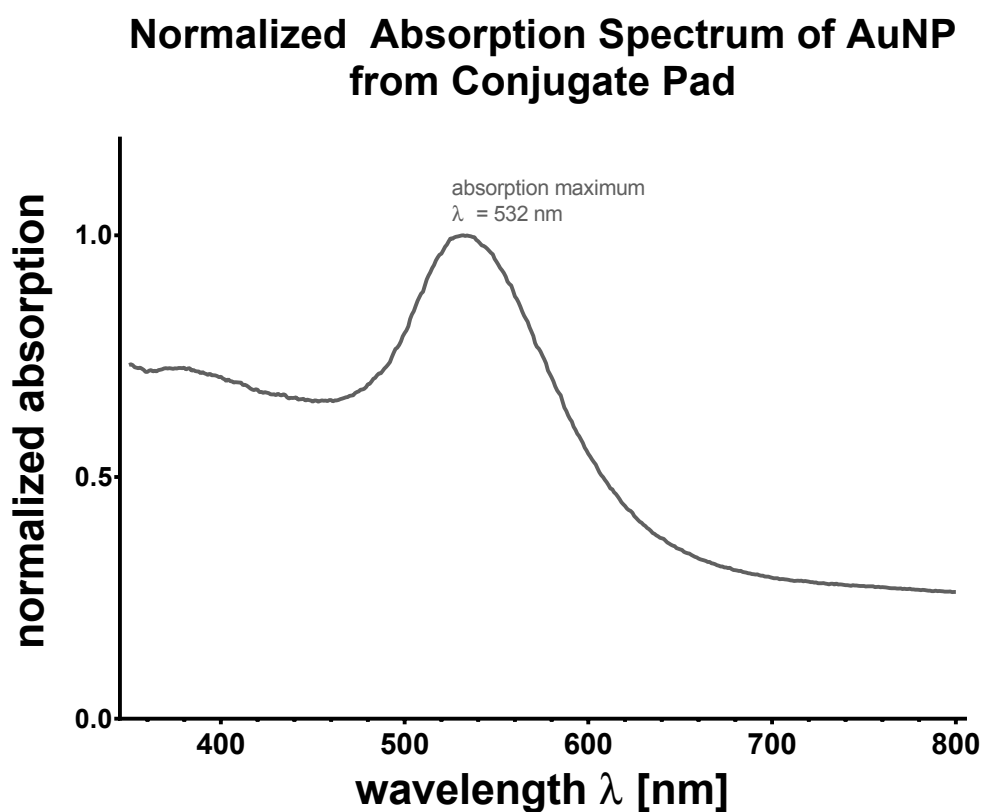


Figure 5.2 UV-Vis absorption spectrum of AuNP recovered from the conjugate pad of lateral flow strips. The spectrum was normalized to give a value of $Abs_{max} = 1$ at the indicated wavelength of the absorption peak at 532 nm.

5.2.3 Absorption Spectra of Gold Nanostars for Conjugation with anti-PTEN Antibody

The comparison of absorption spectra of conjugated and unconjugated AuNS showed the expected shape, which was reported previously [141, 146]. As seen in figure 5.3, both AuNS populations had a similar spectrum. However, the absorption maximum shifted clearly from a wavelength of $\lambda = 628$ nm for unconjugated particles to $\lambda = 634.5$ nm for AuNS after conjugation — a behavior, which was already reported in literature upon conjugation with biomolecules [141].

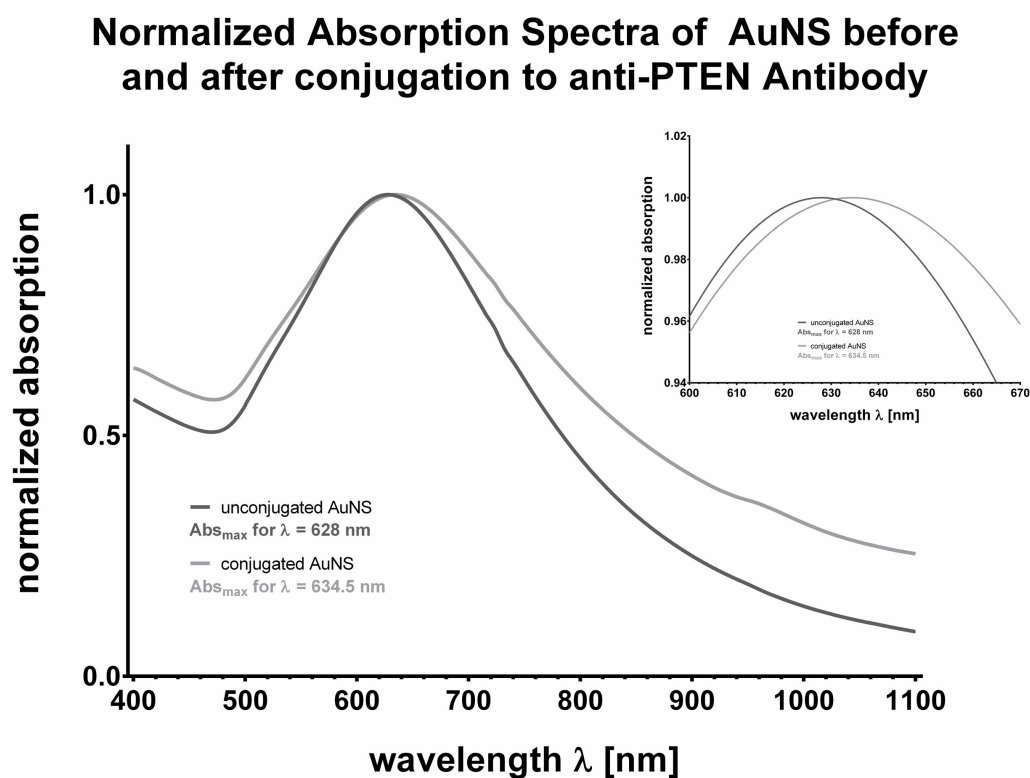


Figure 5.3 Comparison of UV-Vis absorption spectra of AuNS and the shift in the absorption maximum after conjugation, as seen in the inset figure. Unconjugated AuNS (dark grey line) and AuNS after conjugation (light grey line) were measured against buffer by Vi Tran. The spectra were normalized to give a value of $Abs_{max} = 1$ at the respective wavelengths of the absorption peaks.

5.2.4 Absorption Spectra of Quantum Dots

The recorded UV-Vis spectra of QDs both before and after the conjugation reaction were very similar in their appearance and showed spectra that coincided with those reported for Cd-based core QDs with ZnS shell [147, 148]. However, it cannot be deduced from the obtained data, whether the core consists of CdSe or CdTe and this information is not disclosed by the supplier. Both populations showed a strong absorption in the near-UV range, which decreased towards the emission wavelength of the QDs at $\lambda = 625$ nm, as seen in figure 5.4. Beyond the emission wavelength, no absorption was detected. These observations did not show any apparent differences for QDs before and after performing the conjugation reaction.

Absorption Spectra of QDots625

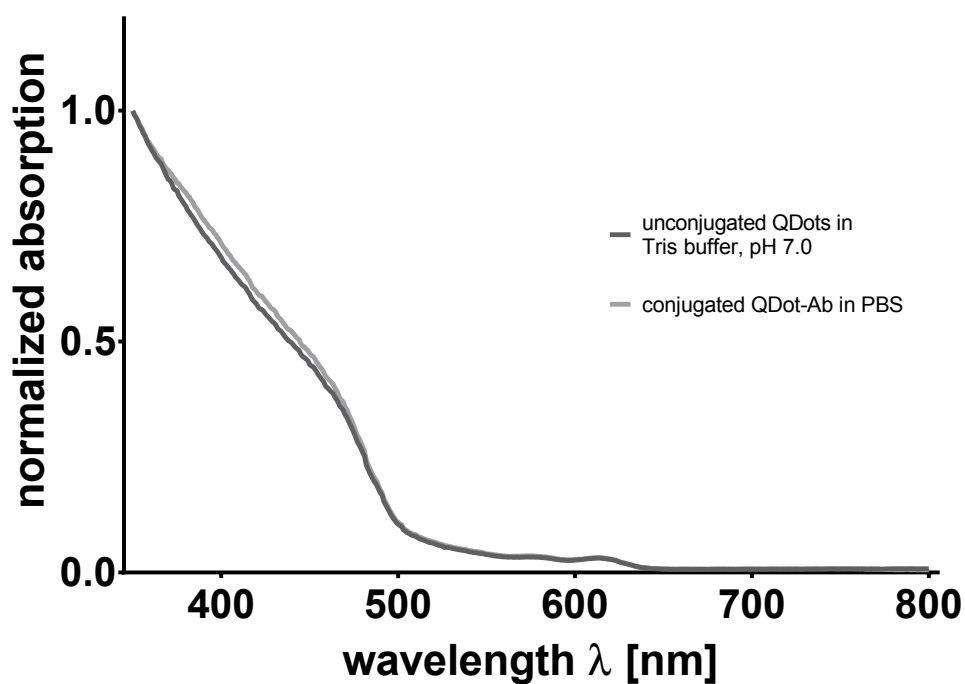


Figure 5.4 UV-Vis absorption spectra of QDs before conjugation, diluted in Tris buffer, pH 7.0 (dark grey line) and QDs after performing the conjugation reaction with an anti-PTEN antibody, diluted in PBS (light grey line). The spectra were normalized to give a value of $Abs_{max} = 1$ at the absorption maximum at the lower limit of the wavelength range.

5.3 Screening Incubation Time for optimized Signal Intensity on Lateral Flow Strips

When different incubation times for binding of the analyte PTEN by the antibody pair were assessed, it became apparent, that a prolonged incubation led to higher signals detectable at the test line of lateral flow strips. As it is depicted in figure 5.5, the signal could be enhanced by around 3-fold when the incubation time was changed from 1 h as recommended by the manufacturer to 6 h. However, some data points showed high variations in the obtained signal intensity. Still, it was possible to fit a saturation function to the obtained data, using a one-phase association model with the equation and obtained parameters as indicated in figure 5.5. According to the fitted function, a value close to the calculated saturation, i.e. a signal intensity of 2.1×10^5 counts, would be reached only after incubation times of over 15 h. However, to ensure stability of analytes and reagents, an incubation time of 5 h was chosen for future experiments.

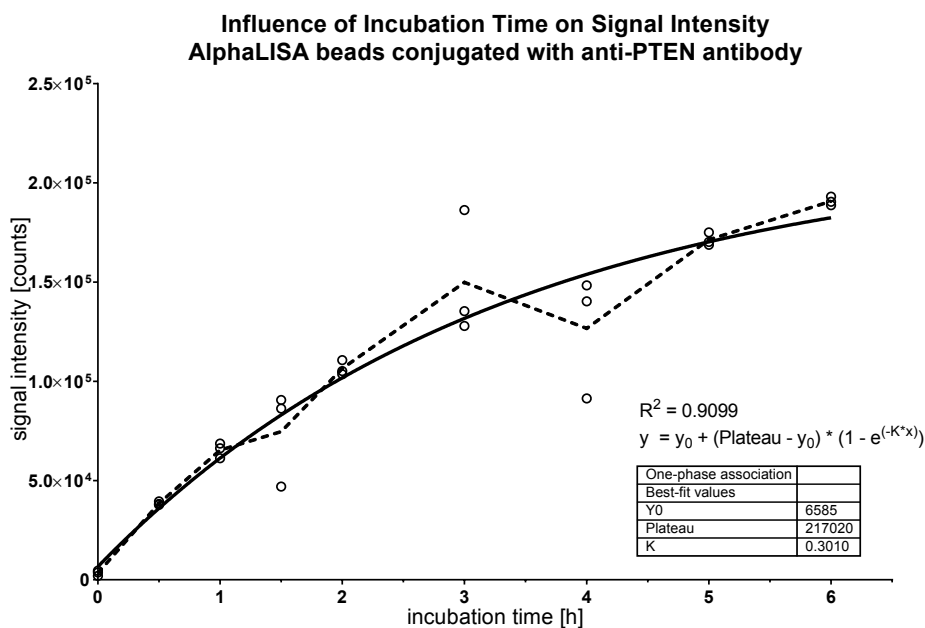


Figure 5.5 Evolution of test line signal intensity from Eu chelates of conjugated AlphaLISA beads detected on lateral flow strips with increasing incubation time. The measured intensities for each time point are represented as open circles and the dashed line connects the resulting mean values. The solid line represents the fit function with the indicated equation and goodness of fit (R^2). Values given in the box represent the obtained values for the parameters of the fit function.

5.4 Standard Curves for PTEN Detection with AlphaLISA Beads on Lateral Flow Strips

The standard curve for PTEN diluted in AlphaLISA assay buffer with 2 % PEG-4000 with AlphaLISA beads, which was recorded on an LRE cPoCLabFluo reader (for a representative scan see appendix, figure 8.16) after 5 h incubation revealed a non-linear behavior of the signal intensity with increasing PTEN concentration. Hence, the described 4-parameter logistics function was fitted to the data, giving the values reported in figure 5.6. As depicted, the fitted function reproduces the measured values well, which is also indicated by the goodness of fit $R^2 = 0.9954$. Based on this function, the LoD was determined as $\text{LoD} = \text{blank average} + 3 \cdot SD$, giving a value of $\text{LoD} = 990.6 \text{ pg mL}^{-1}$. The same was true for a standard curve prepared by diluting PTEN in AlphaLISA assay buffer with 2 % PEG-4000 and 1 h incubation time with the antibody mixture, depicted in figure 8.17 of the appendix. The 4-parameter logistic function resulted in a good fit of the data points ($R^2 = 0.9671$), but a higher LoD of 4267 pg mL^{-1} , as expected from screening the incubation time of the assay.

In contrast to the dilution of PTEN in buffer, the dilution in concentrated medium showed a shift of the standard curve to higher PTEN concentrations. Still, the general shape of the standard curve remained the same, allowing for a fit of the measured values with a 4-parameter logistics function. Figure 5.7 illustrates the measured signals intensities for the decadic logarithm of the employed PTEN concentrations and the fitted function, together with the obtained parameters for the fit function. As indicated by the goodness of fit with $R^2 = 0.9989$ the measured values are well reflected by the 4-parameter logistic function and allowed to calculate the LoD as before, giving a value of $\text{LoD} = 2370 \text{ pg mL}^{-1}$.

Standard Curve for PTEN on Lateral Flow Strips in AlphaLISA buffer - 5 h incubation

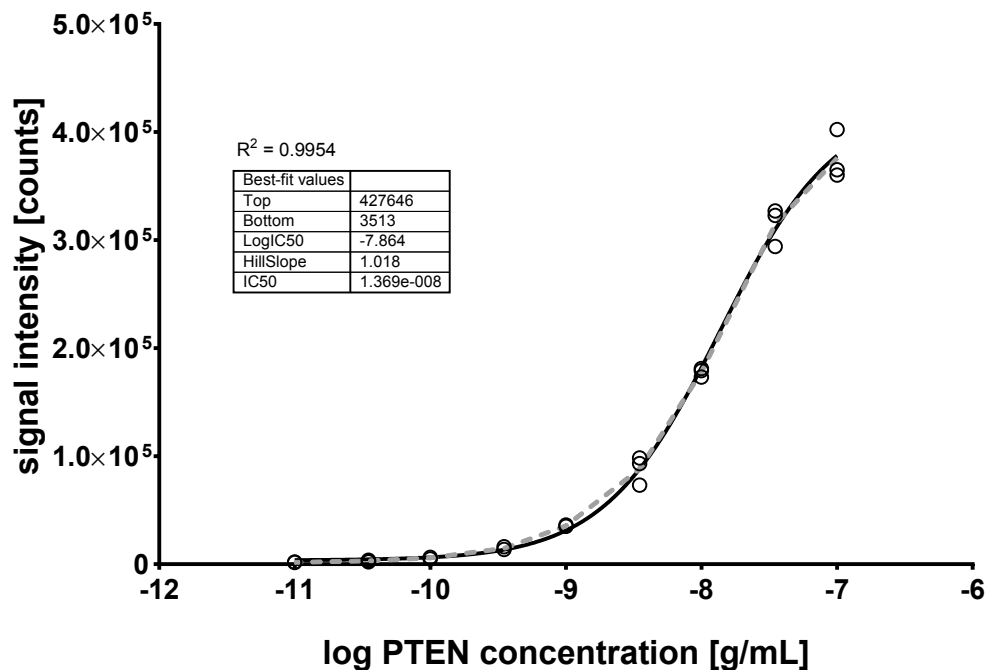


Figure 5.6 Calibration curve for PTEN diluted in AlphaLISA assay buffer with 2% PEG-4000, using AlphaLISA beads conjugated to anti-PTEN antibody in-house and an incubation time with the analyte of 5 h. Signals were recorded on an LRE cPoCLabFluo reader and samples were prepared in triplicate. The blank-corrected signal maxima at the test line are depicted as open circles for each data point and the mean for each PTEN concentration is represented by the grey dashed line. The black solid line represents the 4-parameter logistics function with the indicated results and goodness of fit R^2 .

When the same strips as read in the LRE cPoCLabFluo reader were imaged using the ChemiDoc MP system and fluorescence signals at the test line were quantified using Lab View software, the measured signal intensity and the PTEN concentration correlated poorly. Hence it was not possible to fit a 4-parameter logistics function to the recorded data, opposed to signals measured in the LRE cPoCLabFluo reader. The distribution of the measured values with respect to the PTEN concentration in buffer is depicted in the appendix, figure 8.18. Due to the poor correlation of signal intensity and PTEN concentration, a quantification of signal intensity by the ChemiDoc MP system was not considered further.

Standard Curve for PTEN on Lateral Flow Strips in concentrated medium - 5 h incubation

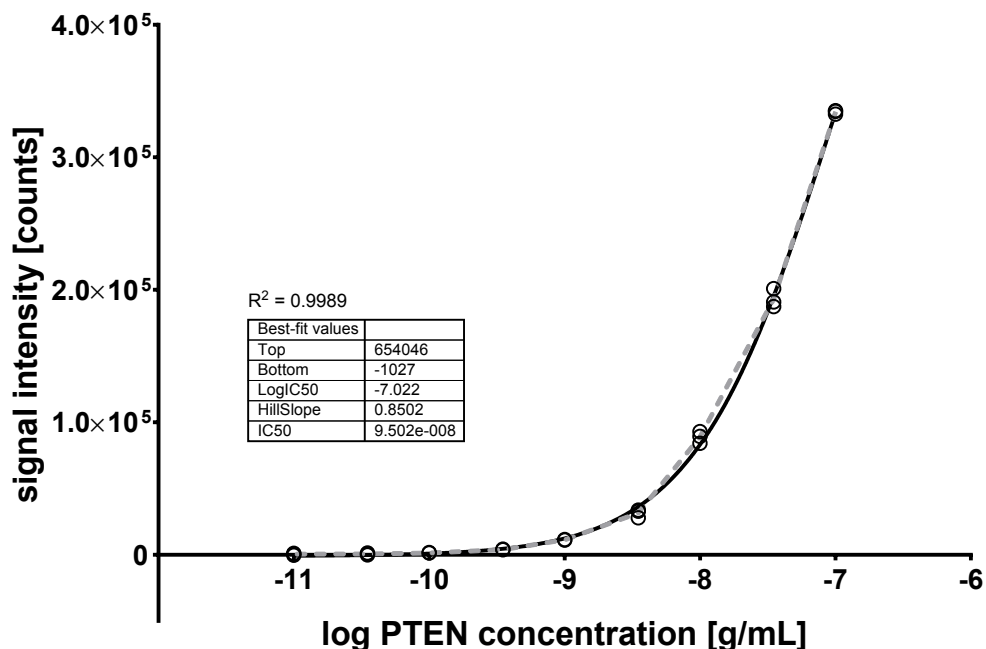


Figure 5.7 Calibration curve for PTEN diluted in concentrated medium (concentration factor: $80\times$), using AlphaLISA beads conjugated to anti-PTEN antibody in-house and an incubation time with the analyte of 5 h. Signals were recorded on an LRE cPoCLabFluo reader and samples were prepared in triplicate. The blank-corrected signal maxima at the test line are depicted as open circles for each data point and the mean for each PTEN concentration is represented by the grey dashed line. The black solid line represents the 4-parameter logistics function with the indicated results and goodness of fit R^2 .

Still, optical images of strips allowed to visually assess the lowest PTEN concentrations detectable on strips by the ChemiDoc MP system. Figure 5.8 shows samples in which PTEN was diluted in AlphaLISA buffer with 2 % PEG-4000, whereas figure 5.9 shows the image of strips, which were tested after diluting PTEN in concentrated medium. The concentrations for which a signal at the test line was still clearly visible were 1.0 ng mL^{-1} and 3.5 ng mL^{-1} for the dilution of PTEN in buffer and concentrated medium, respectively. Furthermore it is visible, that the signal along the test and control lines is not uniform and an increased signal is observed at the edges of lateral flow strips.

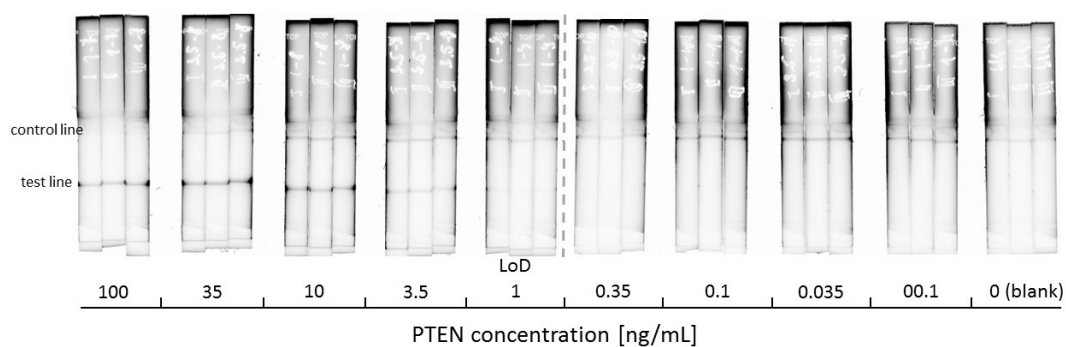


Figure 5.8 Optical image with inverted grey scale values of lateral flow test strips, imaged on a ChemiDoc MP system. Concentrations of PTEN after dilution in AlphaLISA assay buffer with 2% PEG-4000 are indicated for each set of triplicates that was prepared. The lowest concentration of PTEN that could be visually detected in the image was 1.0 ng mL^{-1} .

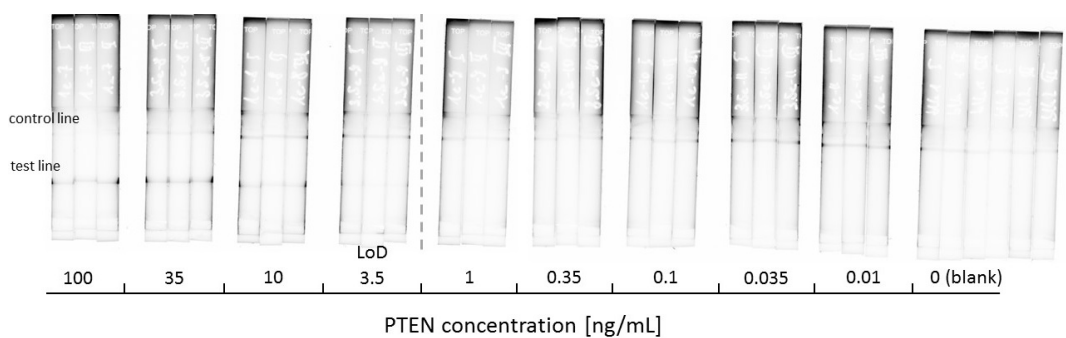


Figure 5.9 Optical image with inverted grey scale values of lateral flow test strips, imaged on a ChemiDoc MP system. Concentrations of PTEN after dilution in concentrated medium (concentration factor: $80\times$) are indicated for each set of triplicates that was prepared. The lowest concentration of PTEN that could be visually detected in the image was 3.5 ng mL^{-1} .

5.5 Spike-and-Recovery Evaluation with conjugated AlphaLISA Beads on Lateral Flow Strips

The calculation of recovery values of PTEN from spiked samples of enriched EVs showed a strong dependence on the matrix used for the preparation of standard curves and the purification strategy of the sample. As depicted in the graphical representation of the recovery values seen in figure 5.10, it can be observed that calculated recovery values were always higher, when calculations were based on the standard curve prepared in concentrated medium. This effect is attributed to the fact that the curve was shifted to higher PTEN concentrations, compared to the standard curve prepared in buffer. Another general observation was, that recovery values were in all cases higher for spiked samples obtained from ultra-filtration than for those from ultra-centrifugation. This was true for calculations based on both standard curves. Furthermore, it was observed that recoveries within one set of samples did not show consistent recovery values. For example, when samples from ultra-filtration were spiked with a final concentration of $3.5 \times 10^{-8} \text{ g mL}^{-1}$ PTEN and the recovery was calculated based on the standard curve prepared with concentrated medium, a recovery value of approximately 114 % was obtained. However, when the same sample was spiked with only $3.5 \times 10^{-10} \text{ g mL}^{-1}$ PTEN, the recovery shifted to values of more than 160 %. This increase in recovery values at decreasing spiking concentrations was observed for all samples. The obtained recovery values for all samples are summarized in table 5.

As it is visible, the calculation of recovery values based on the standard curve prepared in buffer does not give results in the desired range of $100 \% \pm 20 \%$, except for the sample obtained from ultra-filtration at the lowest spiking concentration. However, due to the described shift in recovery values for decreasing PTEN concentrations, this result was not regarded as reliable. Due to the matrix effect of the PTEN diluent used in the preparation of standard curves, all recovery values remained far below the spiked PTEN concentration, when calculated based on the standard curve prepared in buffer. For the calculation of recovery values using the standard curve prepared in concentrated medium however, it became apparent that the spiked PTEN concentration was exceeded by far. This observation was more pronounced in samples from ultra-filtration. Samples from ultra-centrifugation however showed a suitable recovery based on the standard curve prepared in concentrated medium for the highest spiking concentration of PTEN, but at lower concentrations a high divergence was observed again.

Recovery of PTEN from spiked 22Rv1 EV samples using different calibration curves

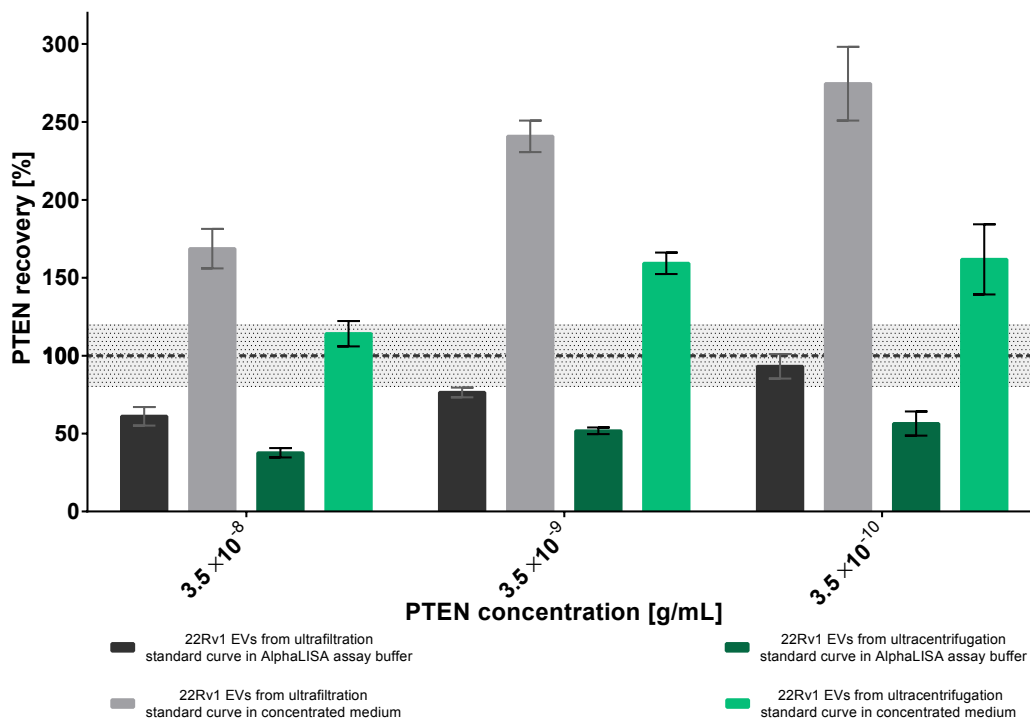


Figure 5.10 Graphical representation of the relative recovery of the indicated spiked PTEN concentrations and their CV from EVs samples of 22Rv1 cells obtained by ultra-filtration (grey bars) or ultra-centrifugation (green bars). The recovery was calculated based on the standard curve prepared in AlphaLISA assay buffer with 2% PEG-4000 (darker colors) or on that prepared in concentrated medium (lighter colors). The dashed horizontal line denotes a recovery of 100% with the desired interval of $\pm 20\%$ as the gray dotted area.

Table 5 Theoretical and measured concentrations of PTEN in spiked samples of purified EVs from 22Rv1 cell line. The SDs for the measured concentration and recovery are given, as well as the CV. The recovery values were calculated based on both standard curves, as indicated.

spiked concentration ng mL ⁻¹	measured concentration ng mL ⁻¹	CV %	recovery %
Recovery determined from Standard Curve in Buffer			
Samples from Ultra-Centrifugation			
35	21.4 ± 2.1	9.79	61.10
3.5	2.67 ± 0.11	4.07	76.42
0.35	0.326 ± 0.028	8.46	93.16
Samples from Ultra-Filtration			
35	13.2 ± 1.07	8.09	37.73
3.5	1.81 ± 0.074	4.09	51.78
0.35	0.198 ± 0.027	13.72	56.47
Recovery determined from Standard Curve in concentrated Medium			
Samples from Ultra-Centrifugation			
35	59.0 ± 4.44	7.52	168.71
3.5	8.43 ± 0.354	4.20	240.79
0.35	0.961 ± 0.083	8.62	274.54
Samples from Ultra-Filtration			
35	39.9 ± 2.83	7.07	114.14
3.5	5.58 ± 0.234	4.28	159.31
0.35	0.566 ± 0.079	13.93	161.78

It was assumed, that the drift of recovery values at lower spiking concentrations might arise from endogenous PTEN present in samples of 22Rv1 EVs, which would have an increasing relative contribution, when lower concentrations of PTEN are used for spiking. Hence, the experiment was repeated with ultra-filtrated EV samples obtained from PNT1a cells, which are known to release PTEN-negative EVs. Figure 5.11 depicts the obtained recovery values, which are also summarized in table 6.

Recovery of PTEN from spiked PNT1a EV samples using different calibration curves

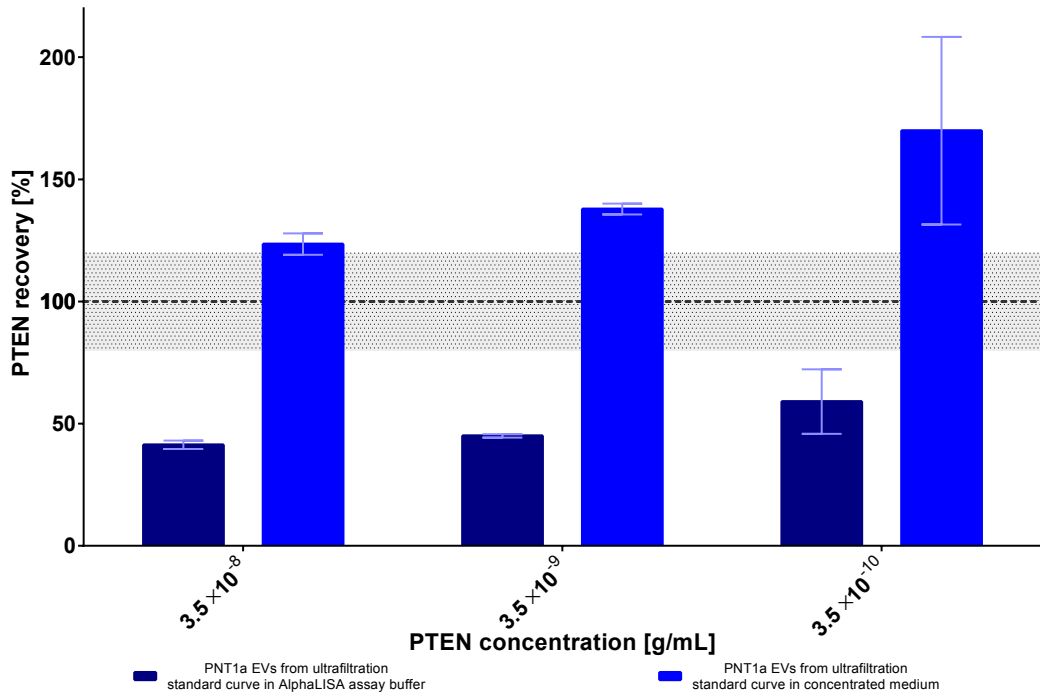


Figure 5.11 Relative recovery of the indicated spiked PTEN concentrations and their CV, measured in spiked EVs samples from PNT1a cells, that were obtained by ultra-filtration. The recovery was calculated based on the standard curve prepared in AlphaLISA assay buffer with 2 % PEG-4000 (darker colors) or on that prepared in concentrated medium (lighter colors). The dashed horizontal line denotes a recovery of 100 % with the desired interval of $\pm 20\%$ as the gray dotted area.

Again, it can be observed that in samples originating from PNT1a cells an increase in the recovery values arises when samples were spiked with decreasing concentrations of PTEN. In addition, the standard curve used for the calculation of recovery values has the same effect as for samples from 22Rv1 cell: when the recovery is calculated based on the standard curve in buffer, values of around 50 % are achieved, whereas the calculation using the standard curve in concentrated medium gives values exceeding 100 %. Still, for the latter case, values are closer to the employed PTEN concentration than it was the case for 22Rv1 EV samples, that were obtained by ultra-filtration.

Table 6 Theoretical and measured concentrations of PTEN in spiked samples of PNT1a EVs, purified by ultra-filtration. The SDs for the measured concentration and recovery are given, as well as the CV. The recovery values were calculated based on both standard curves, as indicated.

spiked concentration ng mL ⁻¹	measured concentration ng mL ⁻¹	CV %	recovery %
Recovery determined from Standard Curve in Buffer			
Samples from Ultra-Centrifugation			
35	14.5 ± 0.60	4.16	41.34
3.5	1.58 ± 0.024	1.53	45.01
0.35	0.207 ± 0.046	22.31	59.04
Recovery determined from Standard Curve in concentrated Medium			
Samples from Ultra-Centrifugation			
35	43.23 ± 1.53	3.54	123.52
3.5	4.83 ± 0.077	1.60	137.87
0.35	0.595 ± 0.134	22.60	169.91

5.6 Standard Curves with Standard AlphaLISA Protocol on Microtiter Plates

Standard curves were prepared on 384-well microtiter plates, following the standard protocol of the AlphaLISA assay, to serve as a comparison to the system transferred to a LFA. Concentrated medium was chosen as the biological matrix for preparation of the standard curve. As an incubation time of 1 h is recommended for the target molecule with the antibodies, it was chosen as a reference point. A representation of the data is depicted in the appendix, figure 8.15. A 4-parameter logistics function could be successfully fitted to the data, which showed non-linear behavior, resulting in a suitable goodness of fit with $R^2 = 0.9985$. For 1 h incubation time, the LoD was calculated from $\text{LoD} = \text{blank average} + 3 \cdot SD$, giving $\text{LoD} = 482 \text{ pg mL}^{-1}$.

In comparison to a standard curve, which was also prepared by diluting PTEN in concentrated medium, but with an incubation time of 5 h a 4-parameter logistics function could again be fitted well ($R^2 = 0.9990$), as seen in figure 5.12. This standard curve was prepared to achieve the same incubation time as for lateral flow strips. Similar to results from lateral flow strips, an increase in sensitivity was observed. Therefore, the limit of detection with 5 h incubation time was $\text{LoD} = 88.9 \text{ pg mL}^{-1}$.

Standard Curve for PTEN on microtiter plate in concentrated medium - 5 h incubation

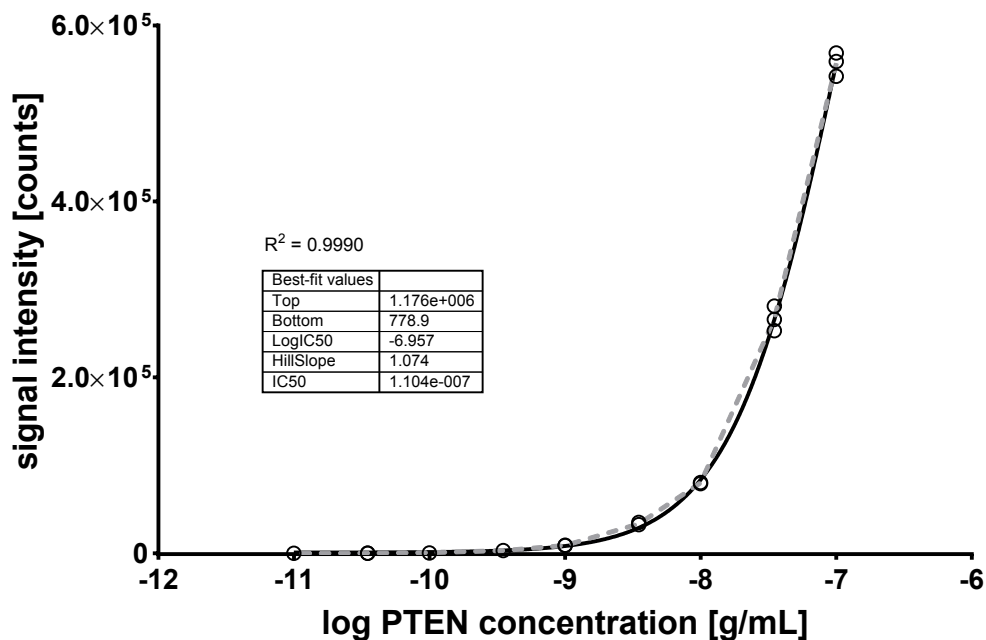


Figure 5.12 Calibration curve for PTEN diluted in concentrated medium (concentration factor: 80 \times), obtained using AlphaLISA acceptor beads conjugated to anti-PTEN antibody in-house in a standard protocol on microtiter plates. The incubation time of antibodies with PTEN was 5 h. Signals were recorded for 300 ms on a Tecan Infinite M1000pro, after excitation of donor beads at 680 nm for 100 ms. All samples were prepared in triplicates, together with four blanks that were measured in triplicate. Blank corrected values for each data point are given by open circles as the blank-corrected signal and the mean for each PTEN concentration is represented by the grey dashed line. The black solid line represents the 4-parameter logistics function with the indicated results and goodness of fit R^2 .

5.7 Spike-and-Recovery Experiments with AlphaLISA Assay on Microtiter Plates

When assessing the recovery of PTEN with the standard AlphaLISA assay format in the same EV samples as for lateral flow strips, a different behavior than in LFAs was observed, as it is depicted in figure 5.13. Using the standard AlphaLISA protocol, there was no apparent discrepancy in the recovery values measured for samples obtained by ultra-centrifugation and the internal controls over the entire range of tested spiking concentrations of PTEN. In addition, samples from ultra-centrifugation did not show increasing recoveries for lower spiking concentrations of PTEN, as it was the case for LFAs. However, spiked samples obtained from ultra-filtration demonstrated recovery values that were elevated and had an increasing trend towards lower spiked PTEN concentrations. Still, the measured recoveries resembled the spiked PTEN concentration more closely than it was the case for LFAs. The obtained values are summarized in table 7.

Table 7 Theoretical concentrations of PTEN in spiked samples of 22Rv1 EVs, purified by ultra-filtration or ultra-centrifugation and their measured recovery. The CV is given for three measurements per concentration, respectively. The recovery values were calculated based on the signal measured in internal controls, prepared in concentrated medium.

spiked concentration ng mL ⁻¹	recovery %	CV %
Recovery calculated from internal control		
<hr/>		
Samples from Ultra-Filtration		
35	122.32	9.65
3.5	132.90	2.13
0.35	157.96	21.21
Samples from Ultra-Centrifugation		
35	109.68	14.68
3.5	106.05	10.10
0.35	100.56	7.64

Recovery of PTEN from spiked 22Rv1 EV samples using AlphaLISA assay on microtiter plates

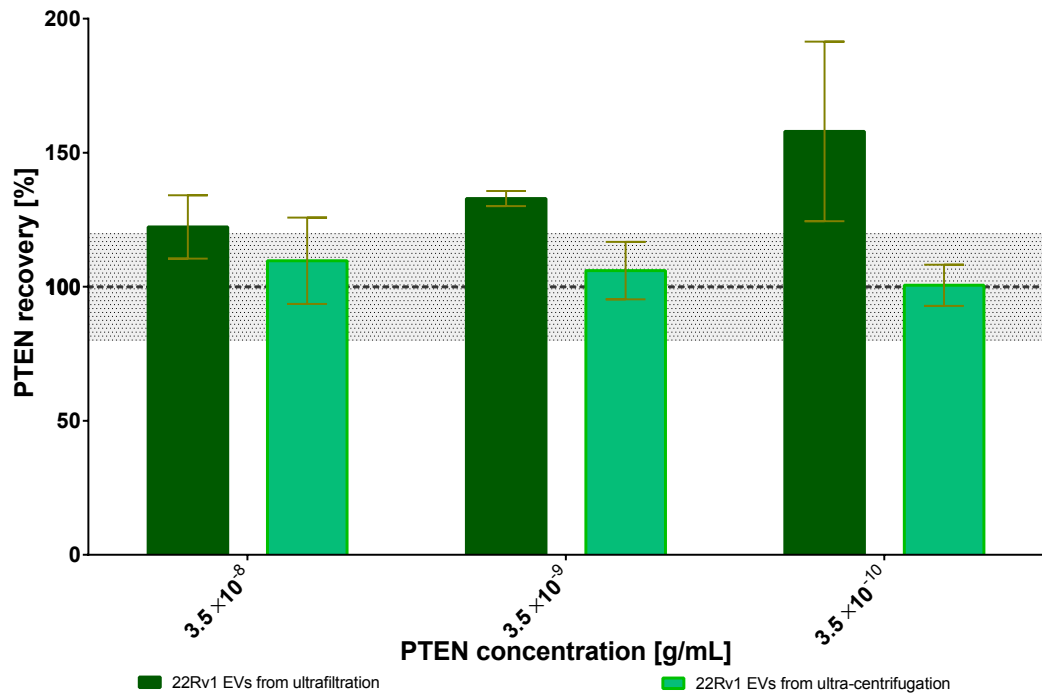


Figure 5.13 Relative recovery of the indicated spiked PTEN concentrations and their CV, measured in spiked EVs samples from 22Rv1 cell, that were obtained by ultra-filtration (dark green) or ultra-centrifugation (light green). The recovery was calculated based on the measured signal of internal controls prepared in concentrated medium. The dashed horizontal line denotes a recovery of 100 % with the desired interval of $\pm 20\%$ as the gray dotted area.

5.8 Performance of Gold Nanoparticles on Lateral Flow Strips

First, it was attempted to conjugate the anti-PTEN antibody directly with AuNP to achieve a similar assay set-up as that using AlphaLISA beads. However, no signal — neither at the control, nor the test line — was visible on the lateral flow strips. This was true, even for extended incubation times and following a protocol reported in literature for the use of AuNP [117] (data not shown). Due to this reason, the protocol was changed to use FITC-conjugates of the anti-PTEN antibody, which should be visualized by the FITC-targeting AuNP contained in the conjugate pad of lateral flow strips.

In this approach, it was observed that false-positive results occurred in the blank control, not containing any PTEN. As shown in figure 5.14, there was no apparent difference between samples containing different concentrations of PTEN, nor between the negative control without PTEN and analyte containing samples. However, it could be verified that these signals did not arise from an unspecific binding of the FITC-antibody conjugate at the test line. The detection of the antibody by a secondary antibody-HRP conjugate did not show accumulation of the FITC-antibody conjugate over the entire test line, but its binding at the control line. In a similar manner, unmodified antibody also showed a strong signal at the control line of lateral flow strips and no accumulation at the test line. Both samples — with FITC-conjugated and unmodified anti-PTEN antibody — are depicted in the appendix, figure 8.22. Hence, it could not be deduced which mechanism was underlying the observed unspecific signal. Therefore, the use of FITC-labelled antibodies with AuNP-conjugates of lateral flow strips was also abandoned, as no measure to eliminate the unspecific signal at the test line could be found in the course of this thesis.

Lastly, the conjugation of the anti-PTEN antibody with AuNS was tested as an approach, which allows both the visual read-out of LFA results as well as the quantitative detection based on Raman reporter molecules.

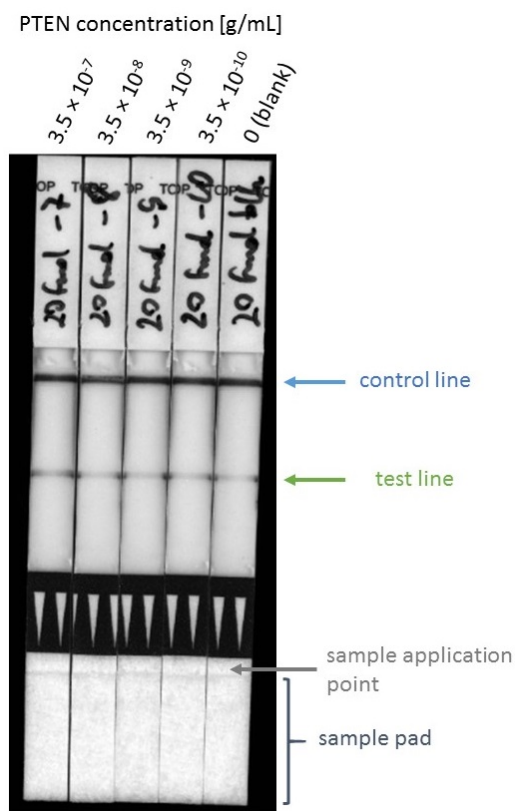


Figure 5.14 Colorimetric image of lateral flow strips, testing 20 fmol of both FITC-conjugated and biotinylated antibody against the indicated PTEN concentrations. The control line shows a strong signal for all samples, including the blank. The test line shows a weaker signal, which cannot be differentiated between different concentrations of PTEN and the blank control without PTEN.

5.9 Performance of AuNS-Antibody Conjugates on Lateral Flow Strips

5.9.1 Visual Read-Out of Lateral Flow Strips with AuNS

The conjugates of AuNS with Raman-active reporter molecules served for both the visual evaluation and the quantitative read-out of LFAs. First, the successful conjugation of anti-PTEN antibodies with AuNS *via* EDC/sNHS coupling was evaluated using lateral flow strips with a Protein A test line. As it can be seen in figure 5.15, a clearly visible band developed at the test line when samples of the conjugate were tested, indicating a successful conjugation. Additionally, the displayed spectra show that the specific accumulation of AuNS coincides with a strong Raman signal of the Raman reporter 4-NTB at its marker band around 1340 cm^{-1} . In contrast, regions outside the test line region show only minor background signal at the spectral region of interest, to which the nitrocellulose itself also contributes. Figure 8.23 of the appendix illustrates, that the unspecific binding of AuNS-conjugates at the test line region is negligible, when Raman spectra outside the test line region are compared to that of the nitrocellulose membrane itself. Hence, the prepared AuNS-conjugates could be employed for measuring a standard curve.

Considering the visual read-out of test results, the lowest detectable PTEN concentration was 2500 pg mL^{-1} , as it is seen in figure 5.16. It was also observed, that test line and control line developed a visually homogeneous signal.

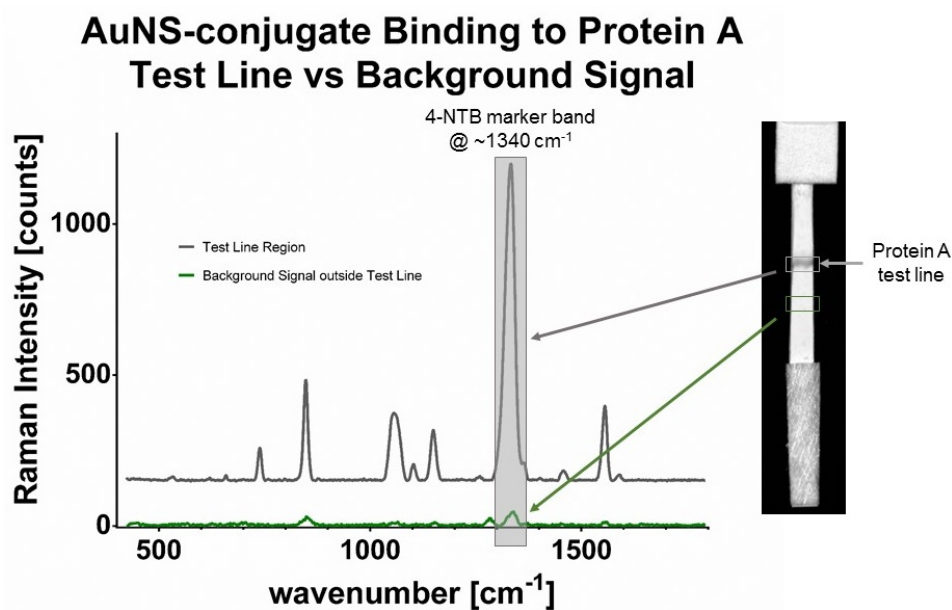


Figure 5.15 Raman spectra obtained from the indicated regions of a lateral flow strip with a Protein A test line. For each region six point measurements were performed and averaged. The strong Raman signal from 4-NTB as the Raman reporter molecule on AuNS at the test line, indicates that particles were successfully conjugated to antibodies, as these are bound by Protein A.

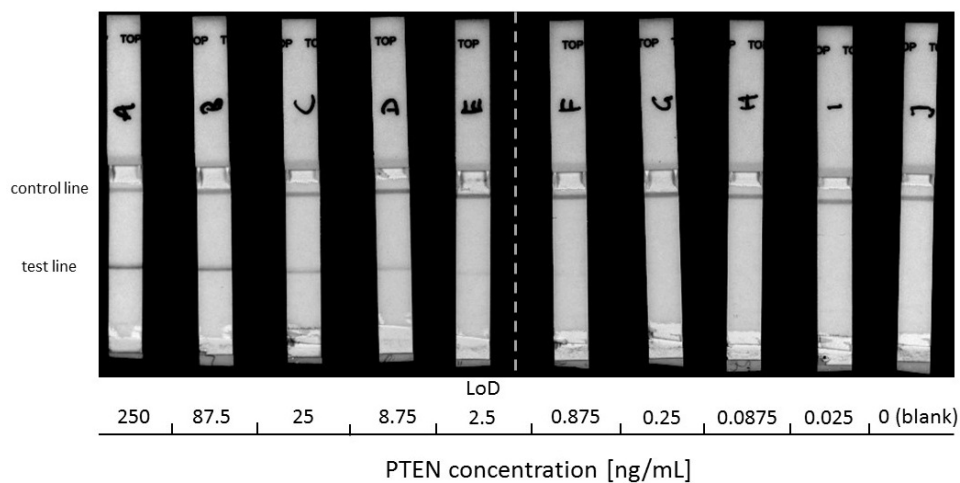


Figure 5.16 Colorimetric image of lateral flow strips used to test the indicated concentrations of PTEN at a AuNS concentration of $OD = 4$ in each sample. The lowest concentration of PTEN that was visually detectable was 2.5 ng mL^{-1} , as indicated in the figure.

5.9.2 Line Scanning Detection of Raman Signal on Lateral Flow Strips

It was observed that not only the visual inspection, but also the measured Raman signal along the test line showed only slight variations in the signal intensity. Figure 8.24 of the appendix shows the spectral region of the marker band of 4-NTB for six different points measured with low variation on the test line when a concentration of $8.75 \times 10^{-8} \text{ g mL}^{-1}$ PTEN was used. To eliminate any further variation in the detection of the Raman signal from 4-NTB, the whole test line was recorded, using line-scanning measurements. With this approach an slightly lower LoD of 2195 pg mL^{-1} compared to the visual read-out was obtained. This values was calculated from the calibration curve as $\text{LoD} = \text{blank average} + 3 \cdot \text{SD}$. In figure 5.17 the obtained signal intensity maxima at the marker band of 4-NTB (877 nm) are plotted against the logarithm of the PTEN concentration. Additionally, figure 8.25 in the appendix shows the recorded spectra of the test lines of the employed samples. In the case of AuNS, it was also possible to obtain a good fit of the calibration curve data ($R^2 = 0.9874$) using equation 2.

**Standard Curve for PTEN in AlphaLISA buffer
using Raman Signal from AuNS on Lateral Flow Strips**

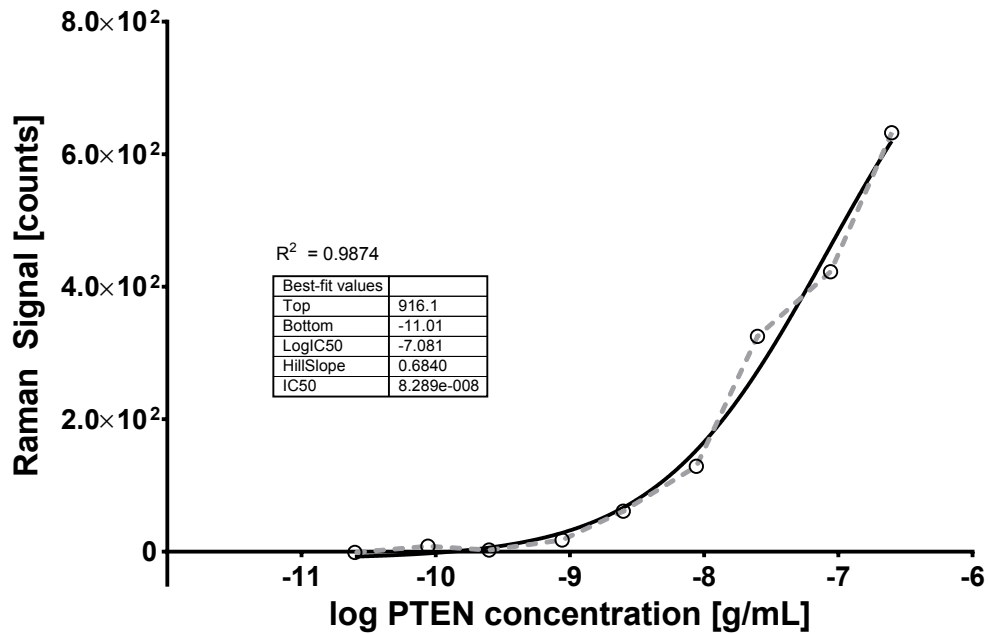


Figure 5.17 Calibration curve for PTEN diluted AlphaLISA assay buffer with 2% PEG-4000 and incubated o/n at 4 °C with AuNS-conjugates and biotinylated antibodies. Signals were recorded on a custom-built Raman strip reader as described in [132] and all samples were prepared with single measurements. The blank-corrected signal maxima of the marker band of 4-NTB (877 nm) are depicted as open circles for each data point and connected by the grey dashed line. The black solid line represents the 4-parameter logistics function with the indicated results and goodness of fit R^2 .

5.10 Comparison of Limits of Detection for the Detection of PTEN

Summarizing the obtained LoDs, it became apparent that the microtiter plate-based format of the AlphaLISA assay represented the most sensitive technique for the detection of PTEN. As found for lateral flow strips, a prolonged incubation time also resulted in enhanced sensitivity compared to the standard incubation time of 1 h. Fluorescence detection from Eu^{3+} doped AlphaLISA beads resulted in the second lowest LoD, when samples of the standard curve were prepared in AlphaLISA assay buffer with 2% PEG-4000 and a similar LoD to the visual and Raman read-out of AuNS was found, when the samples were prepared in concentrated medium. To summarize these findings, the detected signal and LoDs of the mentioned methods are given in table 8.

Table 8 Limits of detection for different measurement techniques with respect to the diluent of PTEN. All samples for standard curve preparation were incubated with the antibodies for 5 h at RT, except for AuNS, which were incubated o/n at 4 °C. Assay buffer is AlphaLISA assay buffer with 2% PEG-4000.

Assay format	measured signal	PTEN diluent	LoD
standard AlphaLISA on microtiter plate	chemiluminescence	concentrated medium	88.9 pg mL^{-1}
AlphaLISA Europium beads in LFAs	fluorescence	concentrated medium	2370 pg mL^{-1}
AlphaLISA Europium beads in LFAs	fluorescence	assay buffer	990.6 pg mL^{-1}
Raman-active AuNS	visual read-out	assay buffer	2500 pg mL^{-1}
Raman-active AuNS	Raman signal (line scanning)	assay buffer	2195 pg mL^{-1}

5.11 Performance of Quantum Dots on Lateral Flow Strips

After performing the conjugation protocol of QDs with anti-PTEN antibodies, the conjugates were tested on lateral flow strips in the same way as conjugated AlphaLISA beads. However, no signal could be detected neither at the test line, nor the control line using the LRE cPoCLabFluo reader. An accumulation of signal was only detected at the beginning of the nitrocellulose membrane of lateral flow strips. Hence, the migration behavior of conjugated QDs was investigated in different buffers.

5.11.1 Running Behavior of QDs on Lateral Flow Strips

When using diluted QD-conjugates in PBS, it became apparent that signal was only detected at the beginning of lateral flow strips, indicating their aggregation. For comparison, a dilution in AlphaLISA assay buffer with 2% PEG-4000 as the standard buffer for LFAs showed the distribution of signal over the entire nitrocellulose membrane, but also a fraction of non-migrating QDs at the beginning of the strips. Hence, PBS seemed to inhibit the migration of QDs in general and the standard buffer seemed to allow for the movement of colloidal QDs, but not aggregates through the nitrocellulose membrane, as the fluorescence image in figure 5.18 shows. Therefore, it was tested why no binding and accumulation of fluorescence signal was observed at neither the test nor the control line. To do so, a dot blot assay was performed.

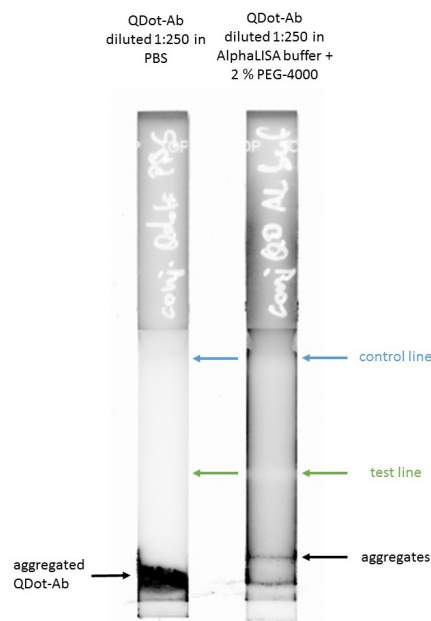


Figure 5.18 Test of running behavior on lateral flow strips. When QD-conjugates were diluted in PBS, particles are aggregated at the very beginning of the nitrocellulose membrane and no signal is detected along the rest of the lateral flow strip (left). A dilution in AlphaLISA assay buffer with 2 % PEG-4000 leads to a distribution of signal along the entire nitrocellulose membrane (right). However, no accumulation is visible in the control line area. In addition, a low number of aggregates can be seen as a narrow band at the beginning of the strip.

5.11.2 Dot Blot Assay with QD-Conjugates

As it was found by the detection of the anti-PTEN antibody using a secondary antibody-HRP conjugate, no co-localization of chemiluminescence signal from the antibody with the fluorescence signal of QDs was observed. As seen in figure 5.19, the unconjugated antibody diluted in AlphaLISA assay buffer with 2 % PEG-4000 showed the highest intensity of chemiluminescence, but no fluorescence signal as expected. For QD-conjugates in the same buffer, a distinct chemiluminescence signal at the spotted PTEN was also observed. However, the fluorescence channel revealed only clusters that were deposited randomly over the membrane, but no accumulation of fluorescence signal on the spotted PTEN. When QD-conjugates were diluted in PBS, the chemiluminescence signal was more faint than for a dilution in AlphaLISA buffer, but still mostly restricted to the spotted PTEN. In contrast, the fluorescence channel revealed, that QDs had accumulated on the entire membrane. A few aggregates are

visible on the membrane, but no accumulation of fluorescence signal at the PTEN spot.

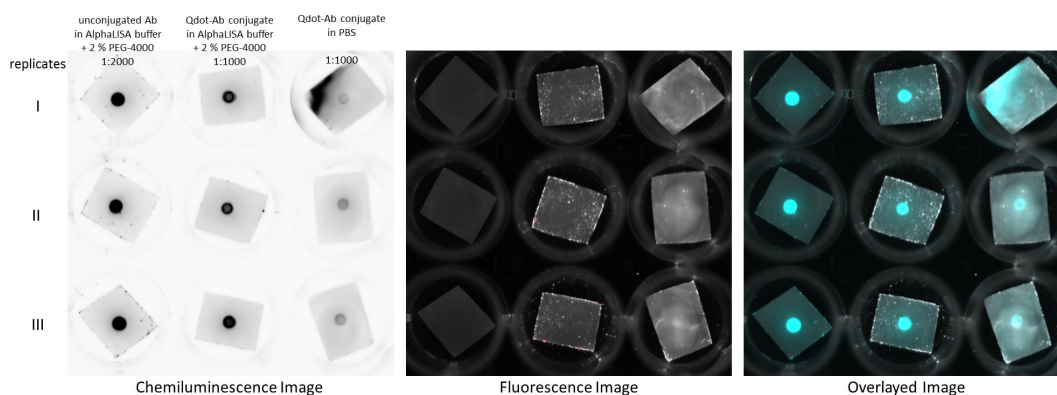


Figure 5.19 Dot blot assay to test antibody conjugation with QDs. Unconjugated antibody, as well as QD-conjugates after dilution in different buffers were assessed, as indicated in the figure. All samples gave chemiluminescence signal on the spot of PTEN with different signal strength (left). Fluorescence signal from QD samples was not restricted or enriched on the spotted protein (middle). The overlaid images show no co-localization of chemiluminescence signal (cyan) with fluorescence signal (grey scale), indicating a failed conjugation.

5.11.3 Separation of QDs by Agarose Gel Electrophoresis

When the migration behavior of QDs was analyzed with agarose gel electrophoresis for the differentiation between conjugated and unconjugated QDs, it first became apparent that a reducing LD resulted in more focused bands in the gel. These allowed for a more reliable comparison between QDs as seen in the gel image (figure 5.20, lane 2 and 4) in comparison to blurry and smeared bands that resulted when non-reducing LD was used (lanes 3 and 5). Comparing the electrophoretic mobility between QDs before and after conjugation, no apparent difference could be observed between both sample types (lanes 2 and 4). In contrast to a retardation expected for conjugated QDs, the obtained reaction product rather migrated slightly faster than unconjugated QDs. However, this effect might also arise from the difference in the applied amount of material, that can be deduced from the difference in fluorescence signal intensity. A similar behavior could be deduced from samples prepared in non-reducing LD, however the blurred lanes do not allow for a reliable comparison.

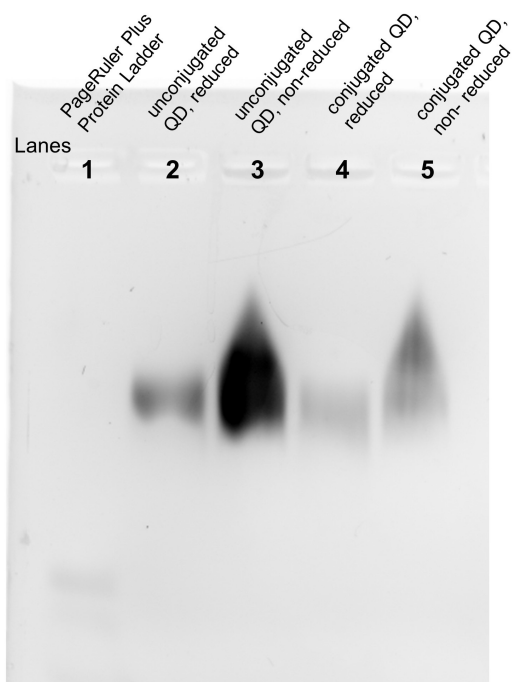


Figure 5.20 Fluorescence image of an agarose gel used for the separation of QDs. The electrophoretic mobility of unconjugated QDs at a final 1:200 dilution in reducing (lane 2) and non-reducing LD (lane 3) was compared to that of the reaction product of the conjugation in a 1:90 dilution, also in reducing (lane 4) and non-reducing LD (lane 5). Lane 1 contained 5 μ L PageRuler Prestained Protein Ladder as a reference of the migration front.

6 Discussion

6.1 Conjugation of AlphaLISA Acceptor Beads with anti-PTEN Antibody

The conjugation of the anti-PTEN antibody with aldehyde-functionalized AlphaLISA acceptor beads was successful, considering their performance in the detection of PTEN by LFAs. It was found, that the conjugated beads produced a specific signal at the test line, when PTEN was captured between the conjugates and a biotinylated antibody against PTEN. Furthermore, the signal intensity was scaling with the employed PTEN concentration and allowed to record standard curves. For blank controls without PTEN, the signal at the test line was not detectable, opposed to the control line signal, which indicates the specificity of conjugate immobilization on lateral flow strips.

However, the recorded DLS data showed a significant size difference between the acceptor beads conjugated in-house and commercially available antibody-bead conjugates (section 5.1.1). It was still concluded, that this size difference might have arisen from batch-to-batch variations in the particle synthesis, as the conjugation of antibodies with the aldehyde-functional beads was successful based upon their performance in LFAs.

6.2 Conjugation of AuNP with anti-PTEN Antibody

In the case of AuNP, determination of the hydrodynamic diameters by DLS measurements (section 5.1.2) gave a strong indication of the conjugation, as unconjugated AuNP were available as a reference. The comparison between AuNP before and after conjugation showed a significant difference between both populations. This difference of approximately 15 nm roughly matches the longest dimension of antibodies, which was reported to be in the range of 10 nm to 12 nm [149, 150]. However, the observed size difference is slightly higher, which can be attributed to the fact, that antibodies might be bound on opposing sides of AuNP with random orientation.

An additional observation in DLS measurements was, that the measured size of unconjugated AuNP was not 40 nm as given by the manufacturer for AuNP, but almost twice the value. This value is believed to arise from the fact, that AuNP are coated with PEG-spacer molecules ($M_W = 10$ kDa). In addition, the absorption spectrum indicates that cores of AuNP had the desired size of approximately 40 nm (section 5.2.1), due to the characteristic absorption peak Abs_{max} at a wavelength of $\lambda = 530$ nm [144].

Despite the indication of successful conjugation of AuNP with anti-PTEN antibodies, the performance in LFAs showed no detectable signal for PTEN at the test line, nor a PTEN-independent signal at the control line. A possible explanation is the low number of AuNP that were immobilized at the test line, even if PTEN was captured by the conjugated antibody. Hence, a different approach was followed, using the AuNP contained in the conjugate pads of lateral flow strips. To do so, it was required to conjugate purchased anti-PTEN capture antibodies with FITC, which could in turn be bound by gold conjugates contained in the lateral flow strip.

6.3 Conjugation of anti-PTEN Antibody with FITC

Using conjugates of the anti-PTEN antibody with FITC, it became apparent that AuNP were indeed accumulated at high densities at the test line giving a strong visual signal (section 5.8). However, this was also true for samples which did not contain any analyte — therefore, the results were false-positive. It is believed that this behavior was due to unspecific binding of the AuNP from the conjugate pad, mediated by components of the FITC-conjugation product. However, it was shown that it did not arise from the antibody itself, as no accumulation at the test line could be observed using a secondary antibody conjugated with HRP. This was also underlined by comparison with the unconjugated anti-PTEN antibody, that showed no accumulation at the test line, but a clear band at the control line. Hence, the mechanism or reaction product from the FITC-labelling reaction giving rise to false-positive results could not be unraveled and the strategy had to be abandoned due to time constraints.

6.4 Conjugation of AuNS with anti-PTEN Antibody

Testing the reaction product of the EDC/sNHS-coupling of AuNS with anti-PTEN antibodies on lateral flow strips with a Protein A test line provided a fast and easy strategy to confirm successful conjugation (section 5.9.1). The visible signal at the test line showed an immobilization of AuNS *via* the conjugated antibody. Additionally, the integrity of AuNS was confirmed by comparing Raman signal intensities of the marker band of 4-NTB inside and outside the test line region. A strong signal coinciding with the visible test line band was observed, while low background signal arose outside the test line region. Hence, it was concluded that the Raman reporter-functionalized AuNS had been successfully conjugated to the anti-PTEN antibody. These findings were supported by a 6.5 nm shift in the absorption peak of AuNS after the conjugation

reaction, as it has been reported for these particles previously [141] (section 5.2.3). Additionally, a significant increase in the hydrodynamic diameter of the particles was measured by DLS (section 5.1.3). The increase in size by approximately 23 nm lies in the range of the dimensions of antibodies, which were previously reported to have a size of 10 nm to 12 nm in their longest dimension [149, 150]. If a random orientation is assumed on opposing sides of the particles, as for AuNP conjugated with anti-PTEN antibody before, the size difference supports the successful conjugation of antibodies with AuNS as well.

6.5 Conjugation of Quantum Dots with anti-PTEN Antibody and their Use in Lateral Flow Assays

After following the protocol for the conjugation of DIBO-functionalized QDs with the anti-PTEN antibody, the potential QD-antibody conjugates were tested in LFAs. However, it was observed that there was no binding of conjugates at the test or control line, but only an accumulation of fluorescence signal at the beginning of the nitrocellulose membrane of strips.

Therefore, the running behavior was first tested after dilution in different buffers (section 5.11.1). The results showed however, that AlphaLISA assay buffer with 2 % PEG-4000 was a suitable buffer to promote migration through the nitrocellulose membrane in general, whereas PBS promoted the aggregation of QDs after a short migration through the membrane. The slight accumulation of fluorescence signal at the beginning of test strips when using AlphaLISA assay buffer was attributed to aggregates, that were detected in DLS measurements. The measured hydrodynamic diameters of these potential aggregates were in the range above 4000 nm, not allowing for particles to migrate through the nitrocellulose membrane. In addition, these DLS measurements revealed that no change in the hydrodynamic diameter of disperse QDs was observed after performing the conjugation protocol (section 5.1.4), indicating that no antibody was bound to the particles. Hence, it was investigated, if QDs were in fact not conjugated to anti-PTEN antibody, explaining the missing signal at the test and control line of lateral flow test strips.

First, a dot blot assay revealed that the purified reaction mixture from the conjugation reaction indeed contained antibody binding to PTEN (section 5.11.2). However, the amount of antibody seemed to be reduced in comparison to the unmodified antibody, which was diluted in a similar manner. Additionally, PBS also showed a decreased binding of antibodies in comparison to samples prepared

in AlphaLISA assay buffer with 2% PEG-4000. Still, in neither of the buffers an accumulation of fluorescence signal was observed at the PTEN spots, which coincided with the chemiluminescence signal arising from anti-PTEN antibodies, that should have been conjugated to QDs. Therefore, it was concluded that the chemiluminescence signal arose from free antibody remaining in the reaction mixture despite the attempted purification step for the removal of unconjugated components of the conjugation reaction.

Secondly, the migration of QDs before and after performing the conjugation in an agarose gel showed no apparent difference in the electrophoretic mobility (section 5.11.3). It rather appeared, that QDs from the conjugation reaction migrated slightly further, potentially due to a loss of the DIBO group during the conjugation reaction. Therefore, the results stand in contrast to those reported in literature, which showed a clear retardation of QDs that were conjugated to proteins with a lower molecular weight than antibodies, when the same parameters for electrophoresis were used [143]. Taking the results from DLS measurements, dot blots and agarose gel electrophoresis together, it had to be concluded that the conjugation reaction failed following the protocol of the manufacturer. Due to these unfavourable observations, the use of QDs for the quantitative detection of PTEN in LFAs could not be pursued further.

6.6 Performance of AlphaLISA Assay Formats

When comparing results from AlphaLISA assays performed in microtiter plates (section 5.6) and on lateral flow strips (section 5.4), it became apparent that the original assay design on microtiter plates showed a higher sensitivity of the assay than that transferred to lateral flow strips. This was reflected by the LoD, which was approximately $27\times$ lower in the plate-based format. However, it has to be stated, that the recorded signal arose from different mechanism in the different assay formats. For the original AlphaLISA assay format, chemiluminescence of europium chelates arises from luminescent oxygen channelling by radicals produced from donor beads in their close proximity upon irradiation with laser light at 680 nm (appendix, figure 8.4). Hence, signal evolves with high local restriction, where acceptor and donor beads are closely coupled *via* the analyte — in this case PTEN [151]. For comparison, the set-up transferred to a LFA relies on the use of acceptor beads only, and their emission of fluorescence upon illumination by light in the near UV range. In contrast to the red-light illumination of donor beads, the excitation light needed for acceptor

bead fluorescence may lead to auto-fluorescence of other materials than the acceptor beads themselves. Hence, a high background signal can lead to a reduction of the assay sensitivity. To circumvent this influence and increase the assay sensitivity, time-resolved fluorescence can be used with europium chelates, due to their long fluorescence life-times, as it was for example shown by Juntunen *et al.* [117]. However, a capable device was not available for these studies.

Another striking observation was the influence of incubation time on the recorded signal intensity and therefore also the assay sensitivity (section 5.3). After screening a range of incubation times for the use in lateral flow assays, 5 h were chosen as a reasonable compromise between signal intensity, assay sensitivity, assay run-time and stability of reactants. The same was true for the standard AlphaLISA protocol on microtiter plates, where an increase in assay sensitivity by around 5-fold could be observed when the incubation time was increased from 1 h as recommended [151] to 5 h as optimized for the use in lateral flow strips. Therefore, the time-dependence of the signal intensity was irrespective of the assay format. This fact indicates a lower affinity of the anti-PTEN antibody conjugated to AlphaLISA beads compared to that present on acceptor beads of the commercial kit.

Lastly, a strong matrix effect became apparent, when standard curves were recorded after dilution of PTEN in different diluents (section 5.4) — a phenomenon previously reported for the plate-based assay format [152]. While the LoD on lateral flow strips was below 1 ng mL^{-1} in AlphaLISA assay buffer with 2% PEG-4000, the LoD was increased around 2.4-fold when PTEN was diluted in concentrated medium. In this richer matrix, there seems to be interference with binding between antibodies and the target by molecules of the concentrated medium and the environment might be molecularly more crowded, hindering the recognition of PTEN by conjugated antibodies. Other possible reasons, that have been discussed in literature include the inner filter effect, arising from light absorbing molecules within the sample. However this effect should be minimal even in biological matrices at the emission wavelength of 615 nm for acceptor beads [152]. A more probable effect might again be the absorption of the excitation light in the near UV range. Furthermore, free biotin in concentrated medium might compete for binding sites [152] at the test line, leading to a lower number of captured acceptor beads. Consequently, it is required to find a suitable matrix for the calibration of the assay and appropriate sample pre-treatment strategies to prevent bias in the detection and quantification of PTEN in the desired matrix of clinical samples.

6.7 Recovery of PTEN from Spiked Samples

Spiking samples of EVs from different cell lines and purification strategies also showed a strong dependence on the sample matrix (section 5.5). For both samples from 22Rv1 cells and that from PNT1a cells it was observed, that the calculation of recovery values was not possible based on the standard curve prepared in buffer. Using this approach, recovery values were in almost all cases far below the desired range of $100\% \pm 20\%$. However, the use of the calibration curve prepared in concentrated medium resulted in higher values, but these exceeded the true spiked concentration substantially. Especially for ultra-filtrated samples from 22Rv1 cells, recoveries were above 150%, as these samples present the richest sample matrix for EVs, that might lead to the detection of unspecific signal. More purified samples from 22Rv1 cells, produced by ultra-centrifugation for comparison showed recovery values within the desired range. However, this was only true for the highest spiking concentration of PTEN. A similar observation was made for ultra-filtrated samples from PNT1a cells, spiked with $3.5 \times 10^{-8} \text{ g mL}^{-1}$ PTEN, which gave a suitable recovery based on the standard curve prepared in concentrated medium. Hence, PTEN-negative EV samples from PNT1a cells gave lower recovery values than those from PTEN-positive EV samples, originating from 22Rv1 cells, when both were obtained from ultra-filtration. This fact indicates that despite the subtraction of blank values, endogenous PTEN might increase the recovery from EV samples substantially as seen for 22Rv1 cells.

Additionally, it was suspected that the shift to higher recovery values seen for samples from 22Rv1 cells with decreasing spiked PTEN concentrations may arise from endogenous PTEN. However, samples from PNT1a cells showed the same behavior despite being PTEN-negative. It can therefore be concluded, that there is an unspecific contribution to the measured signal. This bias was most probably measured constantly throughout all samples, however its relative contribution is rising with lower spiked amounts of PTEN. Hence, it results in an increase of the observed recovery values on lateral flow strips when the spiked PTEN concentration was decreasing in all sample types employed for spike-and-recovery experiments.

A comparison with recovery values achieved using the standard AlphaLISA assay format on microtiter plates (section 5.7) underlines the explanation of increasing recovery values by a systematic error in LFAs. As it was shown for recovery experiments on microtiter plates using an internal reference, recovery values were similar throughout all spiking concentrations of PTEN for both sample types, respectively.

In these experiments, EV samples obtained by ultra-centrifugation allowed for recovering the spiked PTEN concentration most precisely, when compared to samples from ultra-filtration and also from LFAs. In contrast, samples from ultra-filtration showed elevated recovery values, which were slightly increasing towards lower spiked concentrations. However, this observation can be explained by the fact that ultra-filtration results in less purified EV populations, due to a concentration of medium constituents by this technique at the same time, which is largely omitted by ultra-centrifugation. Hence, a higher endogenous level of PTEN results, contributing to the measured recovery.

Concludingly, it can be said that the standard AlphaLISA assay format proved to deliver more realistic recovery values of PTEN, although an internal control for the measured signal is required. Additionally, it was shown that no systematic error resulted in this assay format, as it was the case for LFAs. Therefore, the microtiter based detection of PTEN is more sensitive and more precise than that on lateral flow strips, but requires dedicated equipment and a complex assay scheme, which should be omitted by the use of LFAs. Lastly, it can be concluded that ultra-centrifugation yields a more suitable matrix for the detection of spiked PTEN than ultra-filtration. This observation also gives an indication for suitable purification strategies of clinical samples to obtain reliable results.

6.8 Performance of AuNS-Conjugates on Lateral Flow Strips

First, the visual assessment of AuNS-conjugates (section 5.9.1) revealed, that it was possible to achieve a LoD that was approximately $2.5\times$ higher than for AlphaLISA beads in LFAs, when samples were prepared in AlphaLISA assay buffer with 2% PEG-4000. Employing the conjugates at a density of $OD = 4$ in the final sample volume allowed for the formation of visually homogeneous signals at the test line, while a surplus of particles was still able to bind at the control line as an indication of the successful assay. In this respect, AuNS allowed to detect PTEN down to concentrations of 2500 pg mL^{-1} without the need for any equipment for the read-out of LFAs. Hence, AuNS as the 'gold standard' for LFAs chosen here showed less sensitivity than fluorescence detection of Eu^{3+} chelates as expected, however their performance was not as inferior as reported previously [117].

Secondly, the use of a custom Raman strip reader for the detection of signals from Raman reporter molecules on AuNS, immobilized at the test line, showed that the technique resulted in a similar LoD compared to the visual read-out (section 5.9.2).

As these results were obtained in preliminary experiments, it is expected that the sensitivity of LFAs using Raman signal of AuNS for PTEN detection can be enhanced by further optimization of the assay set-up and measurement parameters. The use of higher AuNS concentrations could for example increase the density of particles at the test line and therefore decrease the LoD by visual read-out and Raman signal measurements. However, the finding of optimal conditions have to be subject to future experiments due to time constraints. In addition, the performance of AuNS in more complex matrices, such as cell culture medium or supernatants tested here, will need to be assessed.

7 Conclusion and Outlook

The results obtained in this master thesis showed that the detection of PTEN as a potential new biomarker from EVs is generally possible by *in vitro* LFAs. This was shown for different kinds of labels and read-out methodologies. It was shown, that the success of conjugation of labels with the chosen antibody for PTEN as the target could be verified by DLS, UV-Vis absorption spectra measurement and agarose gel electrophoresis. Hence, these experiments present a straightforward tool-box for the easy characterization of the obtained labels to evaluate their suitability for LFAs.

With the help of these methods, fluorescent AlphaLISA acceptor beads and AuNS were shown to be successfully conjugated to the anti-PTEN antibodies, while also performing suitably in the detection of PTEN. In contrast, these technique also indicated a successful conjugation of AuNP with the antibody, however there was no detectable signal in LFAs. In addition, the conjugation of anti-PTEN antibodies with FITC resulted in false-positive test results and the conjugation of the same antibody with QDs failed.

Therefore, only the use of conjugated AlphaLISA acceptor beads could be tested in a standard microtiter plate-based format and on lateral flow strips, as well as conjugates of AuNS by their visual read-out and Raman measurements. As it was reported, the use of the standard AlphaLISA assay format showed highest sensitivity in the detection of PTEN and the highest precision in the recovery of PTEN from spiked model matrices. For similar experiments on lateral flow strips, a decreased sensitivity was observed and it was not possible to reliably determine the amount of PTEN in model matrices. Furthermore, long incubation times were required for the chosen antibody pair, impeding the fast read-out that is usually associated with LFAs. Lastly, only preliminary experiments could be performed with conjugates of AuNS. Still, the obtained results showed that even the visual read-out of these nanoparticles is similarly sensitive as the fluorescence detection of AlphaLISA beads in concentrated medium on lateral flow strips. With the help of a custom-built Raman strip reader, the sensitivity might even be enhanced further after optimization of the system. Still, the reproducibility of these results needs to be confirmed in future experiments and for different matrices.

However, in general the identification of a suitable biological matrix for the detection of PTEN and hence optimized sample preparation schemes are still required. As there is no consensus in the scientific community about appropriate purification strategies for the diagnostic use of EVs yet, the final sample matrix for the detection

of PTEN is still unknown. Nevertheless, it could be shown that its choice for assay calibration is of high importance, due to possible matrix effects on the detection.

Once defined EV populations can be obtained from biological samples, it is also desired to implement their specific enrichment within the assay. In this way, concentrated EV populations could be separated by surface-markers according to their tissue of origin, for example at a first test line of LFAs. Thereafter, the lysis and detection of desired EV content should occur on the same lateral flow strips, capturing the respective analyte at a second test line. However, due to the minute amounts of specific biomarkers contained in EV samples, a most sensitive detection scheme has to be found. In the course of this thesis, the Raman detection of marker molecules on AuNS and fluorescence detection from Eu^{3+} doped AlphaLISA beads were found to meet these requirements. Hence, future investigation and validation of the proposed detection strategy should rely on these labels. In addition, the conjugation with antibodies with a higher affinity for PTEN may additionally accelerate test-to-result times. In this way, a rapid PoC system could be found, relying on the read-out by a miniaturized and compact Raman reader, which might be translated from a prototype to a commercial solution.

References

- [1] Rebecca L. Siegel, Kimberly D. Miller, and Ahmedin Jemal. “Cancer Statistics, 2019”. In: *CA: A Cancer Journal for Clinicians* 69.1 (Jan. 1, 2019), pp. 7–34. ISSN: 0007-9235. DOI: 10.3322/caac.21551. URL: <https://onlinelibrary.wiley.com/doi/full/10.3322/caac.21551> (visited on 02/18/2019).
- [2] E. David Crawford et al. “Reduction in the Risk of Prostate Cancer: Future Directions After the Prostate Cancer Prevention Trial”. In: *Urology* 75.3 (Mar. 1, 2010), pp. 502–509. ISSN: 0090-4295. DOI: 10.1016/j.urology.2009.05.099. URL: <http://www.sciencedirect.com/science/article/pii/S0090429509009315> (visited on 02/18/2019).
- [3] Jeffrey J. Tosoian et al. “Active Surveillance for Prostate Cancer: Current Evidence and Contemporary State of Practice”. In: *Nature Reviews Urology* 13.4 (Apr. 2016), pp. 205–215. ISSN: 1759-4812, 1759-4820. DOI: 10.1038/nrurol.2016.45. URL: <http://www.nature.com/articles/nrurol.2016.45> (visited on 02/18/2019).
- [4] Laurence Klotz et al. “Long-Term Follow-Up of a Large Active Surveillance Cohort of Patients With Prostate Cancer”. In: *Journal of Clinical Oncology* 33.3 (Dec. 15, 2014), pp. 272–277. ISSN: 0732-183X. DOI: 10.1200/JCO.2014.55.1192. URL: <http://ascopubs.org/doi/full/10.1200/JCO.2014.55.1192> (visited on 02/18/2019).
- [5] Rebecka Arnsrud Godtman et al. “Long-Term Results of Active Surveillance in the Göteborg Randomized, Population-Based Prostate Cancer Screening Trial”. In: *European Urology* 70.5 (Nov. 1, 2016), pp. 760–766. ISSN: 0302-2838. DOI: 10.1016/j.eururo.2016.03.048. URL: <http://www.sciencedirect.com/science/article/pii/S0302283816300264> (visited on 02/18/2019).
- [6] Mark S. Litwin and Hung-Jui Tan. “The Diagnosis and Treatment of Prostate Cancer: A Review”. In: *JAMA* 317.24 (June 27, 2017), pp. 2532–2542. ISSN: 0098-7484. DOI: 10.1001/jama.2017.7248. URL: <https://jamanetwork.com/journals/jama/fullarticle/2633921> (visited on 02/18/2019).
- [7] Daniel A. Barocas et al. “Association Between Radiation Therapy, Surgery, or Observation for Localized Prostate Cancer and Patient-Reported Outcomes After 3 Years”. In: *JAMA* 317.11 (Mar. 21, 2017), pp. 1126–1140. ISSN: 0098-7484. DOI: 10.1001/jama.2017.1704. URL: <https://jamanetwork.com/journals/jama/fullarticle/2612618> (visited on 02/18/2019).

- [8] Ronald C. Chen et al. “Association Between Choice of Radical Prostatectomy, External Beam Radiotherapy, Brachytherapy, or Active Surveillance and Patient-Reported Quality of Life Among Men With Localized Prostate Cancer”. In: *JAMA* 317.11 (Mar. 21, 2017), pp. 1141–1150. ISSN: 0098-7484. DOI: 10.1001/jama.2017.1652. URL: <https://jamanetwork.com/journals/jama/fullarticle/2612617> (visited on 02/18/2019).
- [9] Amy Zhang et al. “Effects of Patient Centered Interventions on Persistent Urinary Incontinence after Prostate Cancer Treatment: A Randomized, Controlled Trial”. In: *The Journal of Urology* 194.6 (Dec. 1, 2015), pp. 1675–1681. ISSN: 0022-5347. DOI: 10.1016/j.juro.2015.07.090. pmid: 26231554. URL: insights.ovid.com (visited on 02/18/2019).
- [10] Deborah Watkins Bruner et al. “Randomized, Double-Blinded, Placebo-Controlled Crossover Trial of Treating Erectile Dysfunction with Sildenafil After Radiotherapy and Short-Term Androgen Deprivation Therapy: Results of RTOG 0215”. In: *The journal of sexual medicine* 8.4 (Apr. 2011), pp. 1228–1238. ISSN: 1743-6095. DOI: 10.1111/j.1743-6109.2010.02164.x. pmid: 21235716. URL: <https://www.ncbi.nlm.nih.gov/pmc/articles/PMC3557497/> (visited on 02/18/2019).
- [11] Hitendra R Patel et al. “Effects of Tadalafil Treatment after Bilateral Nerve-Sparing Radical Prostatectomy: Quality of Life, Psychosocial Outcomes, and Treatment Satisfaction Results from a Randomized, Placebo-Controlled Phase IV Study”. In: *BMC Urology* 15 (Apr. 12, 2015). ISSN: 1471-2490. DOI: 10.1186/s12894-015-0022-9. pmid: 25879460. URL: <https://www.ncbi.nlm.nih.gov/pmc/articles/PMC4419565/> (visited on 02/18/2019).
- [12] Jeremy Couper et al. “Cognitive Existential Couple Therapy (CECT) in Men and Partners Facing Localised Prostate Cancer: A Randomised Controlled Trial”. In: *BJU International* 115.S5 (Apr. 1, 2015), pp. 35–45. ISSN: 1464-4096. DOI: 10.1111/bju.12991. URL: <https://onlinelibrary.wiley.com/doi/full/10.1111/bju.12991> (visited on 02/18/2019).
- [13] Addie C. Wootten et al. “Preliminary Results of a Randomised Controlled Trial of an Online Psychological Intervention to Reduce Distress in Men Treated for Localised Prostate Cancer”. In: *European Urology* 68.3 (Sept. 1, 2015), pp. 471–479. ISSN: 0302-2838. DOI: 10.1016/j.eururo.2014.10.024. URL: <http://www.sciencedirect.com/science/article/pii/S0302283814010380> (visited on 02/18/2019).

- [14] H. BALLENTINE Carter et al. “EXPECTANT MANAGEMENT OF NON-PALPABLE PROSTATE CANCER WITH CURATIVE INTENT: PRELIMINARY RESULTS”. In: *The Journal of Urology* 167.3 (Mar. 1, 2002), pp. 1231–1234. ISSN: 0022-5347. DOI: 10.1016/S0022-5347(05)65271-8. URL: <http://www.sciencedirect.com/science/article/pii/S0022534705652718> (visited on 02/18/2019).
- [15] L. Boccon-Gibod. “Rising PSA with a Negative Biopsy”. In: *European Urology* 40 (Suppl. 2 2001), pp. 3–8. ISSN: 0302-2838, 1873-7560. DOI: 10.1159/000049878. pmid: 11684858. URL: <https://www.karger.com/Article/FullText/49878> (visited on 05/20/2019).
- [16] Virginia A. Moyer. “Screening for Prostate Cancer: U.S. Preventive Services Task Force Recommendation Statement”. In: *Annals of Internal Medicine* 157.2 (July 17, 2012), p. 120. ISSN: 0003-4819. DOI: 10.7326/0003-4819-157-2-201207170-00459. URL: <http://annals.org/article.aspx?doi=10.7326/0003-4819-157-2-201207170-00459> (visited on 02/18/2019).
- [17] Laurence Klotz. “Defining ‘Progression’ and Triggers for Curative Intervention during Active Surveillance”. In: *Current Opinion in Urology* 25.3 (May 2015), p. 258. ISSN: 0963-0643. DOI: 10.1097/MOU.0000000000000158. URL: https://journals.lww.com/co-urology/fulltext/2015/05000/Defining_progression_and_triggers_for_curative.15.aspx (visited on 02/18/2019).
- [18] James E. Thompson et al. “Medium-Term Oncological Outcomes for Extended vs Saturation Biopsy and Transrectal vs Transperineal Biopsy in Active Surveillance for Prostate Cancer”. In: *BJU International* 115.6 (June 1, 2015), pp. 884–891. ISSN: 1464-4096. DOI: 10.1111/bju.12858. URL: <https://onlinelibrary.wiley.com/doi/full/10.1111/bju.12858> (visited on 02/18/2019).
- [19] Alexander Kretschmer and Derya Tilki. “Biomarkers in Prostate Cancer – Current Clinical Utility and Future Perspectives”. In: *Critical Reviews in Oncology/Hematology* 120 (Dec. 1, 2017), pp. 180–193. ISSN: 1040-8428. DOI: 10.1016/j.critrevonc.2017.11.007. URL: <http://www.sciencedirect.com/science/article/pii/S1040842817303785> (visited on 02/18/2019).
- [20] Eberhard G. Trams et al. “Exfoliation of Membrane Ecto-Enzymes in the Form of Micro-Vesicles”. In: *Biochimica et Biophysica Acta (BBA) - Biomem-*

- branes* 645.1 (June 6, 1981), pp. 63–70. ISSN: 0005-2736. DOI: 10.1016/0005-2736(81)90512-5. URL: <http://www.sciencedirect.com/science/article/pii/0005273681905125> (visited on 02/19/2019).
- [21] R. M. Johnstone et al. “Exosome Formation during Maturation of Mammalian and Avian Reticulocytes: Evidence That Exosome Release Is a Major Route for Externalization of Obsolete Membrane Proteins”. In: *Journal of Cellular Physiology* 147.1 (Apr. 1, 1991), pp. 27–36. ISSN: 0021-9541. DOI: 10.1002/jcp.1041470105. URL: <https://onlinelibrary.wiley.com/doi/abs/10.1002/jcp.1041470105> (visited on 02/19/2019).
- [22] R. M. Johnstone et al. “Vesicle Formation during Reticulocyte Maturation. Association of Plasma Membrane Activities with Released Vesicles (Exosomes).” In: *Journal of Biological Chemistry* 262.19 (May 7, 1987), pp. 9412–9420. ISSN: 0021-9258, 1083-351X. pmid: 3597417. URL: <http://www.jbc.org/content/262/19/9412> (visited on 02/19/2019).
- [23] G. Raposo et al. “B Lymphocytes Secrete Antigen-Presenting Vesicles”. In: *The Journal of Experimental Medicine* 183.3 (Mar. 1, 1996), pp. 1161–1172. ISSN: 0022-1007. pmid: 8642258.
- [24] Yong Hyun Park et al. “Prostate-Specific Extracellular Vesicles as a Novel Biomarker in Human Prostate Cancer”. In: *Scientific Reports* 6 (Aug. 9, 2016), p. 30386. ISSN: 2045-2322. DOI: 10.1038/srep30386. URL: <https://www.nature.com/articles/srep30386> (visited on 02/19/2019).
- [25] Graça Raposo and Willem Stoorvogel. “Extracellular Vesicles: Exosomes, Microvesicles, and Friends”. In: *J Cell Biol* 200.4 (Feb. 18, 2013), pp. 373–383. ISSN: 0021-9525, 1540-8140. DOI: 10.1083/jcb.201211138. pmid: 23420871. URL: <http://jcb.rupress.org/content/200/4/373> (visited on 02/19/2019).
- [26] V. R. Minciocchi et al. “Extracellular Vesicles for Liquid Biopsy in Prostate Cancer: Where Are We and Where Are We Headed?” In: *Prostate Cancer and Prostatic Diseases* 20.3 (Sept. 2017), pp. 251–258. ISSN: 1476-5608. DOI: 10.1038/pcan.2017.7. URL: <https://www.nature.com/articles/pcan20177> (visited on 02/19/2019).
- [27] Li Mu et al. “Analysis of the RNA Content of the Exosomes Derived from Blood Serum and Urine and Its Potential as Biomarkers”. In: *Philosophical Transactions of the Royal Society B: Biological Sciences* 369.1652 (Sept. 26,

- 2014), p. 20130502. DOI: 10.1098/rstb.2013.0502. URL: <https://royalsocietypublishing.org/doi/full/10.1098/rstb.2013.0502> (visited on 02/19/2019).
- [28] Michael L. Merchant et al. “Isolation and Characterization of Urinary Extracellular Vesicles: Implications for Biomarker Discovery”. In: *Nature Reviews Nephrology* 13.12 (Dec. 2017), pp. 731–749. ISSN: 1759-507X. DOI: 10.1038/nrneph.2017.148. URL: <https://www.nature.com/articles/nrneph.2017.148> (visited on 04/17/2019).
- [29] Chiara Ciardiello et al. “Focus on Extracellular Vesicles: New Frontiers of Cell-to-Cell Communication in Cancer”. In: *International Journal of Molecular Sciences* 17.2 (Feb. 6, 2016). ISSN: 1422-0067. DOI: 10.3390/ijms17020175. pmid: 26861306. URL: <https://www.ncbi.nlm.nih.gov/pmc/articles/PMC4783909/> (visited on 02/19/2019).
- [30] Amy M. Booth et al. “Exosomes and HIV Gag Bud from Endosome-like Domains of the T Cell Plasma Membrane”. In: *J Cell Biol* 172.6 (Mar. 13, 2006), pp. 923–935. ISSN: 0021-9525, 1540-8140. DOI: 10.1083/jcb.200508014. pmid: 16533950. URL: <http://jcb.rupress.org/content/172/6/923> (visited on 02/19/2019).
- [31] Valentina R. Minciacchi, Michael R. Freeman, and Dolores Di Vizio. “Extracellular Vesicles in Cancer: Exosomes, Microvesicles and the Emerging Role of Large Oncosomes”. In: *Seminars in cell & developmental biology* 40 (Apr. 2015), pp. 41–51. ISSN: 1084-9521. DOI: 10.1016/j.semcdb.2015.02.010. pmid: 25721812. URL: <https://www.ncbi.nlm.nih.gov/pmc/articles/PMC4747631/> (visited on 02/19/2019).
- [32] Guillaume van Niel, Gisela D’Angelo, and Graça Raposo. “Shedding Light on the Cell Biology of Extracellular Vesicles”. In: *Nature Reviews Molecular Cell Biology* 19.4 (Jan. 17, 2018), pp. 213–228. ISSN: 1471-0072, 1471-0080. DOI: 10.1038/nrm.2017.125. URL: <http://www.nature.com/doifinder/10.1038/nrm.2017.125> (visited on 02/20/2019).
- [33] Anna Bergsmedh et al. “Horizontal Transfer of Oncogenes by Uptake of Apoptotic Bodies”. In: *Proceedings of the National Academy of Sciences of the United States of America* 98.11 (May 22, 2001), pp. 6407–6411. ISSN: 0027-8424. DOI: 10.1073/pnas.101129998. pmid: 11353826. URL: <https://www.ncbi.nlm.nih.gov/pmc/articles/PMC33481/> (visited on 02/19/2019).

- [34] Dolores Di Vizio et al. “Oncosome Formation in Prostate Cancer: Association with a Region of Frequent Chromosomal Deletion in Metastatic Disease”. In: *Cancer Research* 69.13 (July 1, 2009), pp. 5601–5609. ISSN: 0008-5472, 1538-7445. DOI: 10.1158/0008-5472.CAN-08-3860. pmid: 19549916. URL: <http://cancerres.aacrjournals.org/content/69/13/5601> (visited on 02/19/2019).
- [35] Dolores Di Vizio et al. “Large Oncosomes in Human Prostate Cancer Tissues and in the Circulation of Mice with Metastatic Disease”. In: *The American Journal of Pathology* 181.5 (Nov. 1, 2012), pp. 1573–1584. ISSN: 0002-9440. DOI: 10.1016/j.ajpath.2012.07.030. URL: <http://www.sciencedirect.com/science/article/pii/S0002944012006001> (visited on 02/19/2019).
- [36] Emanuele Cocucci and Jacopo Meldolesi. “Ectosomes and Exosomes: Shedding the Confusion between Extracellular Vesicles”. In: *Trends in Cell Biology* 25.6 (June 1, 2015), pp. 364–372. ISSN: 0962-8924. DOI: 10.1016/j.tcb.2015.01.004. URL: <http://www.sciencedirect.com/science/article/pii/S096289241500015X> (visited on 06/07/2019).
- [37] Mathilde Mathieu et al. “Specificities of Secretion and Uptake of Exosomes and Other Extracellular Vesicles for Cell-to-Cell Communication”. In: *Nature Cell Biology* 21.1 (Jan. 2019), p. 9. ISSN: 1476-4679. DOI: 10.1038/s41556-018-0250-9. URL: <https://www.nature.com/articles/s41556-018-0250-9> (visited on 06/07/2019).
- [38] Marina Colombo, Graça Raposo, and Clotilde Théry. “Biogenesis, Secretion, and Intercellular Interactions of Exosomes and Other Extracellular Vesicles”. In: *Annual Review of Cell and Developmental Biology* 30.1 (2014), pp. 255–289. DOI: 10.1146/annurev-cellbio-101512-122326. pmid: 25288114. URL: <https://doi.org/10.1146/annurev-cellbio-101512-122326> (visited on 06/07/2019).
- [39] Clotilde Théry et al. “Minimal Information for Studies of Extracellular Vesicles 2018 (MISEV2018): A Position Statement of the International Society for Extracellular Vesicles and Update of the MISEV2014 Guidelines”. In: *Journal of Extracellular Vesicles* 7.1 (Dec. 1, 2018), p. 1535750. ISSN: null. DOI: 10.1080/20013078.2018.1535750. URL: <https://doi.org/10.1080/20013078.2018.1535750> (visited on 06/07/2019).

- [40] Hadi Valadi et al. “Exosome-Mediated Transfer of mRNAs and microRNAs Is a Novel Mechanism of Genetic Exchange between Cells”. In: *Nature Cell Biology* 9.6 (June 2007), pp. 654–659. ISSN: 1476-4679. DOI: 10.1038/ncb1596. URL: <https://www.nature.com/articles/ncb1596> (visited on 02/19/2019).
- [41] Johan Skog et al. “Glioblastoma Microvesicles Transport RNA and Proteins That Promote Tumour Growth and Provide Diagnostic Biomarkers”. In: *Nature Cell Biology* 10.12 (Dec. 2008), pp. 1470–1476. ISSN: 1476-4679. DOI: 10.1038/ncb1800. URL: <https://www.nature.com/articles/ncb1800> (visited on 02/19/2019).
- [42] James H Hurley. “ESCRT Complexes and the Biogenesis of Multivesicular Bodies”. In: *Current Opinion in Cell Biology*. Cell Structure and Dynamics 20.1 (Feb. 1, 2008), pp. 4–11. ISSN: 0955-0674. DOI: 10.1016/j.ceb.2007.12.002. URL: <http://www.sciencedirect.com/science/article/pii/S0955067407001913> (visited on 02/21/2019).
- [43] Keiichi Tamai et al. “Exosome Secretion of Dendritic Cells Is Regulated by Hrs, an ESCRT-0 Protein”. In: *Biochemical and Biophysical Research Communications* 399.3 (Aug. 27, 2010), pp. 384–390. ISSN: 0006-291X. DOI: 10.1016/j.bbrc.2010.07.083. URL: <http://www.sciencedirect.com/science/article/pii/S0006291X10014038> (visited on 02/21/2019).
- [44] Katarina Trajkovic et al. “Ceramide Triggers Budding of Exosome Vesicles into Multivesicular Endosomes”. In: *Science* 319.5867 (Feb. 29, 2008), pp. 1244–1247. ISSN: 0036-8075, 1095-9203. DOI: 10.1126/science.1153124. pmid: 18309083. URL: <http://science.sciencemag.org/content/319/5867/1244> (visited on 02/21/2019).
- [45] Félix M. Goñi and Alicia Alonso. “Effects of Ceramide and Other Simple Sphingolipids on Membrane Lateral Structure”. In: *Biochimica et Biophysica Acta (BBA) - Biomembranes*. Lipid Interactions, Domain Formation, and Lateral Structure of Membranes 1788.1 (Jan. 1, 2009), pp. 169–177. ISSN: 0005-2736. DOI: 10.1016/j.bbamem.2008.09.002. URL: <http://www.sciencedirect.com/science/article/pii/S0005273608002915> (visited on 02/21/2019).
- [46] Alexander C. Theos et al. “A Lumenal Domain-Dependent Pathway for Sorting to Intralumenal Vesicles of Multivesicular Endosomes Involved in Organelle Morphogenesis”. In: *Developmental Cell* 10.3 (Mar. 1, 2006), pp. 343–

354. ISSN: 1534-5807. DOI: 10.1016/j.devcel.2006.01.012. URL: <http://www.sciencedirect.com/science/article/pii/S153458070600058X> (visited on 02/21/2019).
- [47] Guillaume van Niel et al. “The Tetraspanin CD63 Regulates ESCRT-Independent and -Dependent Endosomal Sorting during Melanogenesis”. In: *Developmental Cell* 21.4 (Oct. 18, 2011), pp. 708–721. ISSN: 1534-5807. DOI: 10.1016/j.devcel.2011.08.019. URL: <http://www.sciencedirect.com/science/article/pii/S1534580711003571> (visited on 02/21/2019).
- [48] Arthit Chairoungdua et al. “Exosome Release of -Catenin: A Novel Mechanism That Antagonizes Wnt Signaling”. In: *The Journal of Cell Biology* 190.6 (Sept. 20, 2010), pp. 1079–1091. ISSN: 0021-9525, 1540-8140. DOI: 10.1083/jcb.201002049. pmid: 20837771. URL: <http://jcb.rupress.org/content/190/6/1079> (visited on 02/21/2019).
- [49] Sonja I. Buschow et al. “MHC II in Dendritic Cells Is Targeted to Lysosomes or T Cell-Induced Exosomes Via Distinct Multivesicular Body Pathways”. In: *Traffic* 10.10 (Oct. 1, 2009), pp. 1528–1542. ISSN: 1398-9219. DOI: 10.1111/j.1600-0854.2009.00963.x. URL: <https://onlinelibrary.wiley.com/doi/full/10.1111/j.1600-0854.2009.00963.x> (visited on 02/21/2019).
- [50] Stéphanie Charrin et al. “Tetraspanins at a Glance”. In: *J Cell Sci* 127.17 (Sept. 1, 2014), pp. 3641–3648. ISSN: 0021-9533, 1477-9137. DOI: 10.1242/jcs.154906. pmid: 25128561. URL: <http://jcs.biologists.org/content/127/17/3641> (visited on 02/21/2019).
- [51] Maria Mittelbrunn, Miguel Vicente-Manzanares, and Francisco Sánchez-Madrid. “Organizing Polarized Delivery of Exosomes at Synapses”. In: *Traffic* 16.4 (Apr. 1, 2015), pp. 327–337. ISSN: 1398-9219. DOI: 10.1111/tra.12258. URL: <https://onlinelibrary.wiley.com/doi/full/10.1111/tra.12258> (visited on 02/22/2019).
- [52] Seema Sinha et al. “Cortactin Promotes Exosome Secretion by Controlling Branched Actin Dynamics”. In: *The Journal of Cell Biology* 214.2 (July 18, 2016), pp. 197–213. ISSN: 0021-9525. DOI: 10.1083/jcb.201601025. pmid: 27402952. URL: <https://www.ncbi.nlm.nih.gov/pmc/articles/PMC4949450/> (visited on 02/22/2019).

- [53] Akihiro Matsumoto et al. “Accelerated Growth of B16BL6 Tumor in Mice through Efficient Uptake of Their Own Exosomes by B16BL6 Cells”. In: *Cancer Science* 108.9 (Sept. 1, 2017), pp. 1803–1810. ISSN: 1347-9032. DOI: 10.1111/cas.13310. URL: <https://onlinelibrary.wiley.com/doi/full/10.1111/cas.13310> (visited on 02/22/2019).
- [54] Andrea Piccin, William G. Murphy, and Owen P. Smith. “Circulating Microparticles: Pathophysiology and Clinical Implications”. In: *Blood Reviews* 21.3 (May 1, 2007), pp. 157–171. ISSN: 0268-960X. DOI: 10.1016/j.blre.2006.09.001. URL: <http://www.sciencedirect.com/science/article/pii/S0268960X0600052X> (visited on 04/17/2019).
- [55] Ayuko Hoshino et al. “Tumour Exosome Integrins Determine Organotropic Metastasis”. In: *Nature* 527.7578 (Nov. 2015), pp. 329–335. ISSN: 1476-4687. DOI: 10.1038/nature15756. URL: <https://www.nature.com/articles/nature15756> (visited on 02/22/2019).
- [56] Esther N. M. Nolte-‘t Hoen et al. “Activated T Cells Recruit Exosomes Secreted by Dendritic Cells via LFA-1”. In: *Blood* 113.9 (Feb. 26, 2009), pp. 1977–1981. ISSN: 0006-4971, 1528-0020. DOI: 10.1182/blood-2008-08-174094. pmid: 19064723. URL: <http://www.bloodjournal.org/content/113/9/1977> (visited on 02/22/2019).
- [57] Kristin Denzer et al. “Follicular Dendritic Cells Carry MHC Class II-Expressing Microvesicles at Their Surface”. In: *The Journal of Immunology* 165.3 (Aug. 1, 2000), pp. 1259–1265. ISSN: 0022-1767, 1550-6606. DOI: 10.4049/jimmunol.165.3.1259. pmid: 10903724. URL: <http://www.jimmunol.org/content/165/3/1259> (visited on 02/22/2019).
- [58] Julia Mallegol et al. “T84-Intestinal Epithelial Exosomes Bear MHC Class II/Peptide Complexes Potentiating Antigen Presentation by Dendritic Cells”. In: *Gastroenterology* 132.5 (May 1, 2007), pp. 1866–1876. ISSN: 0016-5085, 1528-0012. DOI: 10.1053/j.gastro.2007.02.043. pmid: 17484880. URL: [https://www.gastrojournal.org/article/S0016-5085\(07\)00402-7/abstract](https://www.gastrojournal.org/article/S0016-5085(07)00402-7/abstract) (visited on 02/22/2019).
- [59] Adrian E. Morelli et al. “Endocytosis, Intracellular Sorting, and Processing of Exosomes by Dendritic Cells”. In: *Blood* 104.10 (Nov. 15, 2004), pp. 3257–3266. ISSN: 0006-4971, 1528-0020. DOI: 10.1182/blood-2004-03-0824. pmid:

15284116. URL: <http://www.bloodjournal.org/content/104/10/3257> (visited on 02/22/2019).
- [60] Anurag Purushothaman et al. “Fibronectin on the Surface of Myeloma Cell-Derived Exosomes Mediates Exosome-Cell Interactions”. In: *Journal of Biological Chemistry* 291.4 (Jan. 22, 2016), pp. 1652–1663. ISSN: 0021-9258, 1083-351X. DOI: 10.1074/jbc.M115.686295. pmid: 26601950. URL: <http://www.jbc.org/content/291/4/1652> (visited on 02/22/2019).
- [61] Bong Hwan Sung et al. “Directional Cell Movement through Tissues Is Controlled by Exosome Secretion”. In: *Nature Communications* 6 (May 13, 2015), p. 7164. ISSN: 2041-1723. DOI: 10.1038/ncomms8164. URL: <https://www.nature.com/articles/ncomms8164> (visited on 02/22/2019).
- [62] Sanyukta Rana et al. “Toward Tailored Exosomes: The Exosomal Tetraspanin Web Contributes to Target Cell Selection”. In: *The International Journal of Biochemistry & Cell Biology* 44.9 (Sept. 1, 2012), pp. 1574–1584. ISSN: 1357-2725. DOI: 10.1016/j.bioce.2012.06.018. URL: <http://www.sciencedirect.com/science/article/pii/S1357272512002178> (visited on 02/22/2019).
- [63] Sonia A. Melo et al. “Glypican-1 Identifies Cancer Exosomes and Detects Early Pancreatic Cancer”. In: *Nature* 523.7559 (July 2015), pp. 177–182. ISSN: 1476-4687. DOI: 10.1038/nature14581. URL: <https://www.nature.com/articles/nature14581> (visited on 02/22/2019).
- [64] Benjamin Frey and Udo S. Gaipl. “The Immune Functions of Phosphatidylserine in Membranes of Dying Cells and Microvesicles”. In: *Seminars in Immunopathology* 33.5 (Sept. 1, 2011), pp. 497–516. ISSN: 1863-2300. DOI: 10.1007/s00281-010-0228-6. URL: <https://doi.org/10.1007/s00281-010-0228-6> (visited on 02/22/2019).
- [65] Ikuhiko Nakase et al. “Active Macropinocytosis Induction by Stimulation of Epidermal Growth Factor Receptor and Oncogenic Ras Expression Potentiates Cellular Uptake Efficacy of Exosomes”. In: *Scientific Reports* 5 (June 3, 2015), p. 10300. ISSN: 2045-2322. DOI: 10.1038/srep10300. URL: <https://www.nature.com/articles/srep10300> (visited on 02/22/2019).
- [66] Du Feng et al. “Cellular Internalization of Exosomes Occurs Through Phagocytosis”. In: *Traffic* 11.5 (May 1, 2010), pp. 675–687. ISSN: 1398-9219. DOI: 10.1111/j.1600-0854.2010.01041.x. URL: <https://onlinelibrary>.

wiley.com/doi/full/10.1111/j.1600-0854.2010.01041.x (visited on 02/22/2019).

- [67] Tian Tian et al. “Exosome Uptake through Clathrin-Mediated Endocytosis and Macropinocytosis and Mediating miR-21 Delivery”. In: *Journal of Biological Chemistry* 289.32 (Aug. 8, 2014), pp. 22258–22267. ISSN: 0021-9258, 1083-351X. DOI: 10.1074/jbc.M114.588046. pmid: 24951588. URL: <http://www.jbc.org/content/289/32/22258> (visited on 02/22/2019).
- [68] Asuka Nanbo et al. “Exosomes Derived from Epstein-Barr Virus-Infected Cells Are Internalized via Caveola-Dependent Endocytosis and Promote Phenotypic Modulation in Target Cells”. In: *Journal of Virology* 87.18 (Sept. 15, 2013), pp. 10334–10347. ISSN: 0022-538X, 1098-5514. DOI: 10.1128/JVI.01310-13. pmid: 23864627. URL: <https://jvi.asm.org/content/87/18/10334> (visited on 02/22/2019).
- [69] Cristina Escrevente et al. “Interaction and Uptake of Exosomes by Ovarian Cancer Cells”. In: *BMC Cancer* 11.1 (Mar. 27, 2011), p. 108. ISSN: 1471-2407. DOI: 10.1186/1471-2407-11-108. URL: <https://doi.org/10.1186/1471-2407-11-108> (visited on 02/22/2019).
- [70] Gabriele De Rubis, Sabna Rajeev Krishnan, and Mary Bebawy. “Liquid Biopsies in Cancer Diagnosis, Monitoring, and Prognosis”. In: *Trends in Pharmacological Sciences* 40.3 (Mar. 1, 2019), pp. 172–186. ISSN: 0165-6147. DOI: 10.1016/j.tips.2019.01.006. URL: <http://www.sciencedirect.com/science/article/pii/S0165614719300173> (visited on 02/22/2019).
- [71] Yusuke Yoshioka et al. “Ultra-Sensitive Liquid Biopsy of Circulating Extracellular Vesicles Using ExoScreen”. In: *Nature Communications* 5 (Apr. 7, 2014), p. 3591. ISSN: 2041-1723. DOI: 10.1038/ncomms4591. URL: <https://www.nature.com/articles/ncomms4591> (visited on 02/22/2019).
- [72] Young Hwa Soung et al. “Exosomes in Cancer Diagnostics”. In: *Cancers* 9.1 (Jan. 2017), p. 8. DOI: 10.3390/cancers9010008. URL: <https://www.mdpi.com/2072-6694/9/1/8> (visited on 02/22/2019).
- [73] Suresh Mathivanan, Hong Ji, and Richard J. Simpson. “Exosomes: Extracellular Organelles Important in Intercellular Communication”. In: *Journal of Proteomics. Current Status of Cancer Proteomics, How Far Are We from Clinical Applications?* 73.10 (Sept. 10, 2010), pp. 1907–1920. ISSN: 1874-3919.

- DOI: 10.1016/j.jprot.2010.06.006. URL: <http://www.sciencedirect.com/science/article/pii/S1874391910001843> (visited on 02/22/2019).
- [74] Yu Li et al. “HAb18G (CD147), a Cancer-Associated Biomarker and Its Role in Cancer Detection”. In: *Histopathology* 54.6 (May 1, 2009), pp. 677–687. ISSN: 0309-0167. DOI: 10.1111/j.1365-2559.2009.03280.x. URL: <https://onlinelibrary.wiley.com/doi/full/10.1111/j.1365-2559.2009.03280.x> (visited on 02/26/2019).
- [75] M. J. Donovan et al. “A Molecular Signature of PCA3 and ERG Exosomal RNA from Non-DRE Urine Is Predictive of Initial Prostate Biopsy Result”. In: *Prostate Cancer and Prostatic Diseases* 18.4 (Dec. 2015), pp. 370–375. ISSN: 1476-5608. DOI: 10.1038/pcan.2015.40. URL: <https://www.nature.com/articles/pcan201540> (visited on 02/19/2019).
- [76] James McKiernan et al. “A Novel Urine Exosome Gene Expression Assay to Predict High-Grade Prostate Cancer at Initial Biopsy”. In: *JAMA Oncology* 2.7 (July 1, 2016), pp. 882–889. ISSN: 2374-2437. DOI: 10.1001/jamaoncol.2016.0097. URL: <https://jamanetwork.com/journals/jamaoncology/fullarticle/2506709> (visited on 02/19/2019).
- [77] Bindhu Madhavan et al. “Combined Evaluation of a Panel of Protein and miRNA Serum-Exosome Biomarkers for Pancreatic Cancer Diagnosis Increases Sensitivity and Specificity”. In: *International Journal of Cancer* 136.11 (June 1, 2015), pp. 2616–2627. ISSN: 0020-7136. DOI: 10.1002/ijc.29324. URL: <https://onlinelibrary.wiley.com/doi/full/10.1002/ijc.29324> (visited on 02/26/2019).
- [78] Shoichiro Tsukita, Mikio Furuse, and Masahiko Itoh. “Multifunctional Strands in Tight Junctions”. In: *Nature Reviews Molecular Cell Biology* 2.4 (Apr. 2001), pp. 285–293. ISSN: 1471-0080. DOI: 10.1038/35067088. URL: <https://www.nature.com/articles/35067088> (visited on 02/26/2019).
- [79] Patrice J. Morin. “Claudin Proteins in Human Cancer: Promising New Targets for Diagnosis and Therapy”. In: *Cancer Research* 65.21 (Nov. 1, 2005), pp. 9603–9606. ISSN: 0008-5472, 1538-7445. DOI: 10.1158/0008-5472.CAN-05-2782. pmid: 16266975. URL: <http://cancerres.aacrjournals.org/content/65/21/9603> (visited on 02/26/2019).

- [80] Jianghong Li et al. “Claudin-Containing Exosomes in the Peripheral Circulation of Women with Ovarian Cancer”. In: *BMC Cancer* 9.1 (July 20, 2009), p. 244. ISSN: 1471-2407. DOI: 10.1186/1471-2407-9-244. URL: <https://doi.org/10.1186/1471-2407-9-244> (visited on 02/26/2019).
- [81] David W. Greening et al. “A Protocol for Exosome Isolation and Characterization: Evaluation of Ultracentrifugation, Density-Gradient Separation, and Immunoaffinity Capture Methods”. In: *Proteomic Profiling: Methods and Protocols*. Ed. by Anton Posch. Methods in Molecular Biology. New York, NY: Springer New York, 2015, pp. 179–209. ISBN: 978-1-4939-2550-6. DOI: 10.1007/978-1-4939-2550-6_15. URL: https://doi.org/10.1007/978-1-4939-2550-6_15 (visited on 02/26/2019).
- [82] Kenneth W. Witwer et al. “Standardization of Sample Collection, Isolation and Analysis Methods in Extracellular Vesicle Research”. In: *Journal of Extracellular Vesicles* 2.1 (Jan. 1, 2013), p. 20360. ISSN: null. DOI: 10.3402/jev.v2i0.20360. URL: <https://doi.org/10.3402/jev.v2i0.20360> (visited on 02/26/2019).
- [83] Jan Lötvall et al. “Minimal Experimental Requirements for Definition of Extracellular Vesicles and Their Functions: A Position Statement from the International Society for Extracellular Vesicles”. In: *Journal of Extracellular Vesicles* 3.1 (Jan. 1, 2014), p. 26913. ISSN: null. DOI: 10.3402/jev.v3.26913. URL: <https://doi.org/10.3402/jev.v3.26913> (visited on 02/26/2019).
- [84] Virginie Vlaeminck-Guillem. “Extracellular Vesicles in Prostate Cancer Carcinogenesis, Diagnosis, and Management”. In: *Frontiers in Oncology* 8 (2018). ISSN: 2234-943X. DOI: 10.3389/fonc.2018.00222. URL: <https://www.frontiersin.org/articles/10.3389/fonc.2018.00222/full> (visited on 02/19/2019).
- [85] Kathleen Gabriel et al. “Regulation of the Tumor Suppressor PTEN through Exosomes: A Diagnostic Potential for Prostate Cancer”. In: *PLoS ONE* 8.7 (July 25, 2013). ISSN: 1932-6203. DOI: 10.1371/journal.pone.0070047. pmid: 23936141. URL: <https://www.ncbi.nlm.nih.gov/pmc/articles/PMC3723640/> (visited on 04/30/2019).
- [86] Antonio Di Cristofano and Pier Paolo Pandolfi. “The Multiple Roles of PTEN in Tumor Suppression”. In: *Cell* 100.4 (Feb. 18, 2000), pp. 387–390. ISSN: 0092-8674. DOI: 10.1016/S0092-8674(00)80674-1. URL: <http://www.>

sciencedirect.com/science/article/pii/S0092867400806741 (visited on 04/30/2019).

- [87] Christopher C. Uzoh et al. “PTEN-Mediated Pathways and Their Association with Treatment-Resistant Prostate Cancer”. In: *BJU International* 104.4 (Aug. 1, 2009), pp. 556–561. ISSN: 1464-4096. DOI: 10.1111/j.1464-410X.2009.08411.x. URL: <https://onlinelibrary.wiley.com/doi/full/10.1111/j.1464-410X.2009.08411.x> (visited on 04/30/2019).
- [88] Jan H. W. Leuvers et al. “A Sol Particle Agglutination Assay for Human Chorionic Gonadotrophin”. In: *Journal of Immunological Methods* 45.2 (Sept. 15, 1981), pp. 183–194. ISSN: 0022-1759. DOI: 10.1016/0022-1759(81)90212-X. URL: <http://www.sciencedirect.com/science/article/pii/002217598190212X> (visited on 03/29/2019).
- [89] Geertruida A. Posthuma-Trumpie, Jakob Korf, and Aart van Amerongen. “Lateral Flow (Immuno)Assay: Its Strengths, Weaknesses, Opportunities and Threats. A Literature Survey”. In: *Analytical and Bioanalytical Chemistry* 393.2 (Jan. 2009), pp. 569–582. ISSN: 1618-2642, 1618-2650. DOI: 10.1007/s00216-008-2287-2. URL: <http://link.springer.com/10.1007/s00216-008-2287-2> (visited on 03/29/2019).
- [90] Xiaolin Huang et al. “Membrane-Based Lateral Flow Immunochromatographic Strip with Nanoparticles as Reporters for Detection: A Review”. In: *Biosensors and Bioelectronics* 75 (Jan. 15, 2016), pp. 166–180. ISSN: 0956-5663. DOI: 10.1016/j.bios.2015.08.032. URL: <http://www.sciencedirect.com/science/article/pii/S0956566315303584> (visited on 03/29/2019).
- [91] Daniel Quesada-González and Arben Merkoçi. “Nanoparticle-Based Lateral Flow Biosensors”. In: *Biosensors and Bioelectronics* 73 (Nov. 15, 2015), pp. 47–63. ISSN: 0956-5663. DOI: 10.1016/j.bios.2015.05.050. URL: <http://www.sciencedirect.com/science/article/pii/S0956566315301482> (visited on 03/29/2019).
- [92] Mika P. A. Laitinen and Matti Vuento. “Affinity Immunosensor for Milk Progesterone: Identification of Critical Parameters”. In: *Biosensors and Bioelectronics* 11.12 (Jan. 1, 1996), pp. 1207–1214. ISSN: 0956-5663. DOI: 10.1016/0956-5663(96)88085-7. URL: <http://www.sciencedirect.com/science/article/pii/0956566396880857> (visited on 03/29/2019).

- [93] M O’Keeffe et al. “Preliminary Evaluation of a Lateral Flow Immunoassay Device for Screening Urine Samples for the Presence of Sulphamethazine”. In: *Journal of Immunological Methods* 278.1 (July 1, 2003), pp. 117–126. ISSN: 0022-1759. DOI: 10.1016/S0022-1759(03)00207-2. URL: <http://www.sciencedirect.com/science/article/pii/S0022175903002072> (visited on 03/29/2019).
- [94] Elizabeth C. Schramm et al. “A Quantitative Lateral Flow Assay to Detect Complement Activation in Blood”. In: *Analytical Biochemistry* 477 (May 15, 2015), pp. 78–85. ISSN: 0003-2697. DOI: 10.1016/j.ab.2015.01.024. URL: <http://www.sciencedirect.com/science/article/pii/S0003269715000470> (visited on 04/02/2019).
- [95] Elisabeth I. Laderman et al. “Rapid, Sensitive, and Specific Lateral-Flow Immunochromatographic Point-of-Care Device for Detection of Herpes Simplex Virus Type 2-Specific Immunoglobulin G Antibodies in Serum and Whole Blood”. In: *Clin. Vaccine Immunol.* 15.1 (Jan. 1, 2008), pp. 159–163. ISSN: 1556-6811, 1556-679X. DOI: 10.1128/CVI.00218-07. pmid: 18003814. URL: <https://cvi.asm.org/content/15/1/159> (visited on 04/02/2019).
- [96] Allison Golden et al. “Extended Result Reading Window in Lateral Flow Tests Detecting Exposure to *Onchocerca Volvulus*: A New Technology to Improve Epidemiological Surveillance Tools”. In: *PLoS ONE* 8.7 (July 23, 2013). ISSN: 1932-6203. DOI: 10.1371/journal.pone.0069231. pmid: 23935960. URL: <https://www.ncbi.nlm.nih.gov/pmc/articles/PMC3720650/> (visited on 04/02/2019).
- [97] Etti Juntunen et al. “Effects of Blood Sample Anticoagulants on Lateral Flow Assays Using Luminescent Photon-Upconverting and Eu(III) Nanoparticle Reporters”. In: *Analytical Biochemistry* 492 (Jan. 1, 2016), pp. 13–20. ISSN: 0003-2697. DOI: 10.1016/j.ab.2015.09.009. URL: <http://www.sciencedirect.com/science/article/pii/S000326971500439X> (visited on 04/02/2019).
- [98] Xiliang Wang et al. “Development of an Immunochromatographic Lateral-Flow Test Strip for Rapid Detection of Sulfonamides in Eggs and Chicken Muscles”. In: *Journal of Agricultural and Food Chemistry* 55.6 (Mar. 1, 2007), pp. 2072–2078. ISSN: 0021-8561. DOI: 10.1021/jf062523h. URL: <https://doi.org/10.1021/jf062523h> (visited on 04/02/2019).

- [99] Yinli Zhao et al. “Development of a Lateral Flow Colloidal Gold Immunoassay Strip for the Rapid Detection of Enrofloxacin Residues”. In: *Journal of Agricultural and Food Chemistry* 56.24 (Dec. 24, 2008), pp. 12138–12142. ISSN: 0021-8561. DOI: 10.1021/jf802648z. URL: <https://doi.org/10.1021/jf802648z> (visited on 04/02/2019).
- [100] Can Zhang, Yan Zhang, and Shuo Wang. “Development of Multianalyte Flow-through and Lateral-Flow Assays Using Gold Particles and Horseradish Peroxidase as Tracers for the Rapid Determination of Carbaryl and Endosulfan in Agricultural Products”. In: *Journal of Agricultural and Food Chemistry* 54.7 (Apr. 1, 2006), pp. 2502–2507. ISSN: 0021-8561. DOI: 10.1021/jf0531407. URL: <https://doi.org/10.1021/jf0531407> (visited on 04/02/2019).
- [101] Helen V. Hsieh, Jeffrey L. Dantzler, and Bernhard H. Weigl. “Analytical Tools to Improve Optimization Procedures for Lateral Flow Assays”. In: *Diagnostics* 7.2 (June 2017), p. 29. DOI: 10.3390/diagnostics7020029. URL: <https://www.mdpi.com/2075-4418/7/2/29> (visited on 04/02/2019).
- [102] Lourdes Rivas et al. “Improving Sensitivity of Gold Nanoparticle-Based Lateral Flow Assays by Using Wax-Printed Pillars as Delay Barriers of Microfluidics”. In: *Lab on a Chip* 14.22 (2014), pp. 4406–4414. DOI: 10.1039/C4LC00972J. URL: <https://pubs.rsc.org/en/content/articlelanding/2014/lc/c4lc00972j> (visited on 04/02/2019).
- [103] Helena de Puig et al. “Challenges of the Nano–Bio Interface in Lateral Flow and Dipstick Immunoassays”. In: *Trends in Biotechnology* 35.12 (Dec. 1, 2017), pp. 1169–1180. ISSN: 0167-7799. DOI: 10.1016/j.tibtech.2017.09.001. URL: <http://www.sciencedirect.com/science/article/pii/S0167779917302317> (visited on 04/02/2019).
- [104] Elif Burcu Bahadır and Mustafa Kemal Sezgintürk. “Lateral Flow Assays: Principles, Designs and Labels”. In: *TrAC Trends in Analytical Chemistry* 82 (Sept. 1, 2016), pp. 286–306. ISSN: 0165-9936. DOI: 10.1016/j.trac.2016.06.006. URL: <http://www.sciencedirect.com/science/article/pii/S0165993616300668> (visited on 04/02/2019).
- [105] Erik C. Dreaden et al. “The Golden Age: Gold Nanoparticles for Biomedicine”. In: *Chemical Society Reviews* 41.7 (Mar. 12, 2012), pp. 2740–2779. ISSN: 1460-4744. DOI: 10.1039/C1CS15237H. URL: <https://pubs.rsc.org/en/content/articlelanding/2012/cs/c1cs15237h> (visited on 04/02/2019).

- [106] Bianca M. I. van der Zande et al. “Colloidal Dispersions of Gold Rods: Synthesis and Optical Properties”. In: *Langmuir* 16.2 (Jan. 1, 2000), pp. 451–458. ISSN: 0743-7463. DOI: 10.1021/la9900425. URL: <https://doi.org/10.1021/la9900425> (visited on 04/02/2019).
- [107] Laura Anfossi et al. “Development and Application of a Quantitative Lateral Flow Immunoassay for Fumonisin in Maize”. In: *Analytica Chimica Acta* 682.1 (Dec. 3, 2010), pp. 104–109. ISSN: 0003-2670. DOI: 10.1016/j.aca.2010.09.045. URL: <http://www.sciencedirect.com/science/article/pii/S0003267010012274> (visited on 04/02/2019).
- [108] D. Tang et al. “Magnetic Nanogold Microspheres-Based Lateral-Flow Immunodipstick for Rapid Detection of Aflatoxin B2 in Food”. In: *Biosensors and Bioelectronics* 25.2 (Oct. 15, 2009), pp. 514–518. ISSN: 0956-5663. DOI: 10.1016/j.bios.2009.07.030. URL: <http://www.sciencedirect.com/science/article/pii/S0956566309004011> (visited on 04/02/2019).
- [109] Hui Xu et al. “Gold-Nanoparticle-Decorated Silica Nanorods for Sensitive Visual Detection of Proteins”. In: *Analytical Chemistry* 86.15 (Aug. 5, 2014), pp. 7351–7359. ISSN: 0003-2700. DOI: 10.1021/ac502249f. URL: <https://doi.org/10.1021/ac502249f> (visited on 04/02/2019).
- [110] Brittany A. Rohrman et al. “A Lateral Flow Assay for Quantitative Detection of Amplified HIV-1 RNA”. In: *PLOS ONE* 7.9 (Sept. 21, 2012), e45611. ISSN: 1932-6203. DOI: 10.1371/journal.pone.0045611. URL: <https://journals.plos.org/plosone/article?id=10.1371/journal.pone.0045611> (visited on 04/02/2019).
- [111] Jinfeng Li et al. “Gold Immunochromatographic Strips for Enhanced Detection of Avian Influenza and Newcastle Disease Viruses”. In: *Analytica Chimica Acta* 782 (June 11, 2013), pp. 54–58. ISSN: 0003-2670. DOI: 10.1016/j.aca.2013.04.022. URL: <http://www.sciencedirect.com/science/article/pii/S0003267013005333> (visited on 04/02/2019).
- [112] L. Anfossi et al. “Increased Sensitivity of Lateral Flow Immunoassay for Ochratoxin A through Silver Enhancement”. In: *Analytical and Bioanalytical Chemistry* 405.30 (Dec. 1, 2013), pp. 9859–9867. ISSN: 1618-2650. DOI: 10.1007/s00216-013-7428-6. URL: <https://doi.org/10.1007/s00216-013-7428-6> (visited on 04/02/2019).

- [113] Minghui Chen et al. “Dual Gold Nanoparticle Lateflow Immunoassay for Sensitive Detection of Escherichia Coli O157:H7”. In: *Analytica Chimica Acta* 876 (May 30, 2015), pp. 71–76. ISSN: 0003-2670. DOI: 10.1016/j.aca.2015.03.023. URL: <http://www.sciencedirect.com/science/article/pii/S0003267015003542> (visited on 04/02/2019).
- [114] Zhizeng Wang et al. “Lateral Flow Test Strip Based on Colloidal Selenium Immunoassay for Rapid Detection of Melamine in Milk, Milk Powder, and Animal Feed”. In: *International Journal of Nanomedicine* (Apr. 2014), p. 1699. ISSN: 1178-2013. DOI: 10.2147/IJN.S58942. URL: <http://www.dovepress.com/lateral-flow-test-strip-based-on-colloidal-selenium-immunoassay-for-ra-peer-reviewed-article-IJN> (visited on 04/03/2019).
- [115] S. C. Lou et al. “One-Step Competitive Immunochromatographic Assay for Semiquantitative Determination of Lipoprotein(a) in Plasma.” In: *Clinical Chemistry* 39.4 (Apr. 1, 1993), pp. 619–624. ISSN: 0009-9147, 1530-8561. pmid: 8472355. URL: <http://clinchem.aaccjnl.org/content/39/4/619> (visited on 04/03/2019).
- [116] P. Noguera et al. “Carbon Nanoparticles in Lateral Flow Methods to Detect Genes Encoding Virulence Factors of Shiga Toxin-Producing Escherichia Coli”. In: *Analytical and Bioanalytical Chemistry* 399.2 (Jan. 1, 2011), pp. 831–838. ISSN: 1618-2650. DOI: 10.1007/s00216-010-4334-z. URL: <https://doi.org/10.1007/s00216-010-4334-z> (visited on 04/04/2019).
- [117] Etti Juntunen et al. “Performance of Fluorescent Europium(III) Nanoparticles and Colloidal Gold Reporters in Lateral Flow Bioaffinity Assay”. In: *Analytical Biochemistry* 428.1 (Sept. 1, 2012), pp. 31–38. ISSN: 0003-2697. DOI: 10.1016/j.ab.2012.06.005. URL: <http://www.sciencedirect.com/science/article/pii/S0003269712003090> (visited on 04/04/2019).
- [118] C. B. Murray, C. R. Kagan, and M. G. Bawendi. “Synthesis and Characterization of Monodisperse Nanocrystals and Close-Packed Nanocrystal Assemblies”. In: *Annual Review of Materials Science* 30.1 (Aug. 1, 2000), pp. 545–610. ISSN: 0084-6600. DOI: 10.1146/annurev.matsci.30.1.545. URL: <https://www.annualreviews.org/doi/10.1146/annurev.matsci.30.1.545> (visited on 04/04/2019).

- [119] John G. Bruno. “Application of DNA Aptamers and Quantum Dots to Lateral Flow Test Strips for Detection of Foodborne Pathogens with Improved Sensitivity versus Colloidal Gold”. In: *Pathogens* 3.2 (June 2014), pp. 341–355. DOI: 10.3390/pathogens3020341. URL: <https://www.mdpi.com/2076-0817/3/2/341> (visited on 04/04/2019).
- [120] Anna N. Berlina et al. “Quantum Dot-Based Lateral Flow Immunoassay for Detection of Chloramphenicol in Milk”. In: *Analytical and Bioanalytical Chemistry* 405.14 (May 1, 2013), pp. 4997–5000. ISSN: 1618-2650. DOI: 10.1007/s00216-013-6876-3. URL: <https://doi.org/10.1007/s00216-013-6876-3> (visited on 04/04/2019).
- [121] N. A. Taranova et al. “‘Traffic Light’ Immunochromatographic Test Based on Multicolor Quantum Dots for the Simultaneous Detection of Several Antibiotics in Milk”. In: *Biosensors and Bioelectronics* 63 (Jan. 15, 2015), pp. 255–261. ISSN: 0956-5663. DOI: 10.1016/j.bios.2014.07.049. URL: <http://www.sciencedirect.com/science/article/pii/S0956566314005508> (visited on 04/04/2019).
- [122] Meiling Ren et al. “Immunochromatographic Assay for Ultrasensitive Detection of Aflatoxin B1 in Maize by Highly Luminescent Quantum Dot Beads”. In: *ACS Applied Materials & Interfaces* 6.16 (Aug. 27, 2014), pp. 14215–14222. ISSN: 1944-8244. DOI: 10.1021/am503517s. URL: <https://doi.org/10.1021/am503517s> (visited on 04/04/2019).
- [123] Hong Duan et al. “Quantum-Dot Submicrobead-Based Immunochromatographic Assay for Quantitative and Sensitive Detection of Zearalenone”. In: *Talanta* 132 (Jan. 15, 2015), pp. 126–131. ISSN: 0039-9140. DOI: 10.1016/j.talanta.2014.08.076. URL: <http://www.sciencedirect.com/science/article/pii/S0039914014007577> (visited on 04/04/2019).
- [124] Yalong Bai et al. “A Sensitive Lateral Flow Test Strip Based on Silica Nanoparticle/CdTe Quantum Dot Composite Reporter Probes”. In: *RSC Advances* 2.5 (Feb. 13, 2012), pp. 1778–1781. ISSN: 2046-2069. DOI: 10.1039/C2RA00976E. URL: <https://pubs.rsc.org/en/content/articlelanding/2012/ra/c2ra00976e> (visited on 04/04/2019).
- [125] I. Hemmilä. “Lanthanides as Probes for Time-Resolved Fluorometric Immunoassays”. In: *Scandinavian Journal of Clinical and Laboratory Investigation* 48.5 (Sept. 1, 1988), pp. 389–399. ISSN: 0036-5513. DOI: 10.1080/

00365518809085747. URL: <https://doi.org/10.1080/00365518809085747> (visited on 04/08/2019).

- [126] Lahja Sev us et al. “Use of Fluorescent Europium Chelates as Labels in Microscopy Allows Glutaraldehyde Fixation and Permanent Mounting and Leads to Reduced Autofluorescence and Good Long-Term Stability”. In: *Microscopy Research and Technique* 28.2 (June 1, 1994), pp. 149–154. ISSN: 1059-910X. DOI: 10.1002/jemt.1070280206. URL: <https://onlinelibrary.wiley.com/doi/abs/10.1002/jemt.1070280206> (visited on 04/08/2019).
- [127] Jingli Yuan and Guilan Wang. “Lanthanide Complex-Based Fluorescence Label for Time-Resolved Fluorescence Bioassay”. In: *Journal of Fluorescence* 15.4 (July 1, 2005), pp. 559–568. ISSN: 1573-4994. DOI: 10.1007/s10895-005-2829-3. URL: <https://doi.org/10.1007/s10895-005-2829-3> (visited on 04/08/2019).
- [128] P. L. a. M. Corstjens et al. “Infrared Up-Converting Phosphors for Bioassays”. In: *IEEE Proceedings - Nanobiotechnology* 152.2 (Apr. 1, 2005), pp. 64–72. ISSN: 1740-9748. DOI: 10.1049/ip-nbt:20045014. URL: https://digital-library.theiet.org/content/journals/10.1049/ip-nbt_20045014 (visited on 04/08/2019).
- [129] Johannes Hampl et al. “Upconverting Phosphor Reporters in Immunochromatographic Assays”. In: *Analytical Biochemistry* 288.2 (Jan. 15, 2001), pp. 176–187. ISSN: 0003-2697. DOI: 10.1006/abio.2000.4902. URL: <http://www.sciencedirect.com/science/article/pii/S0003269700949029> (visited on 04/08/2019).
- [130] R. Sam Niedbala et al. “Detection of Analytes by Immunoassay Using Up-Converting Phosphor Technology”. In: *Analytical Biochemistry* 293.1 (June 1, 2001), pp. 22–30. ISSN: 0003-2697. DOI: 10.1006/abio.2001.5105. URL: <http://www.sciencedirect.com/science/article/pii/S000326970195105X> (visited on 04/08/2019).
- [131] Peng Zhao et al. “Upconversion Fluorescent Strip Sensor for Rapid Determination of *Vibrio Anguillarum*”. In: *Nanoscale* 6.7 (Mar. 14, 2014), pp. 3804–3809. ISSN: 2040-3372. DOI: 10.1039/C3NR06549A. URL: <https://pubs.rsc.org/en/content/articlelanding/2014/nr/c3nr06549a> (visited on 04/08/2019).

- [132] Vi Tran et al. “Rapid, Quantitative, and Ultrasensitive Point-of-Care Testing: A Portable SERS Reader for Lateral Flow Assays in Clinical Chemistry”. In: *Angewandte Chemie International Edition* 58.2 (Jan. 8, 2019), pp. 442–446. ISSN: 1433-7851. DOI: 10.1002/anie.201810917. URL: <https://onlinelibrary.wiley.com/doi/full/10.1002/anie.201810917> (visited on 04/08/2019).
- [133] Joonki Hwang, Sangyeop Lee, and Jaebum Choo. “Application of a SERS-Based Lateral Flow Immunoassay Strip for the Rapid and Sensitive Detection of Staphylococcal Enterotoxin B”. In: *Nanoscale* 8.22 (June 2, 2016), pp. 11418–11425. ISSN: 2040-3372. DOI: 10.1039/C5NR07243C. URL: <https://pubs.rsc.org/en/content/articlelanding/2016/nr/c5nr07243c> (visited on 04/10/2019).
- [134] Lucía Blanco-Covián et al. “Au@Ag SERRS Tags Coupled to a Lateral Flow Immunoassay for the Sensitive Detection of Pneumolysin”. In: *Nanoscale* 9.5 (Feb. 2, 2017), pp. 2051–2058. ISSN: 2040-3372. DOI: 10.1039/C6NR08432J. URL: <https://pubs.rsc.org/en/content/articlelanding/2017/nr/c6nr08432j> (visited on 04/10/2019).
- [135] Myriam Oliveira-Rodríguez et al. “Development of a Rapid Lateral Flow Immunoassay Test for Detection of Exosomes Previously Enriched from Cell Culture Medium and Body Fluids”. In: *Journal of Extracellular Vesicles* 5.1 (Jan. 1, 2016), p. 31803. ISSN: null. DOI: 10.3402/jev.v5.31803. URL: <https://doi.org/10.3402/jev.v5.31803> (visited on 04/10/2019).
- [136] Myriam Oliveira-Rodríguez et al. “Point-of-Care Detection of Extracellular Vesicles: Sensitivity Optimization and Multiple-Target Detection”. In: *Biosensors and Bioelectronics* 87 (Jan. 15, 2017), pp. 38–45. ISSN: 0956-5663. DOI: 10.1016/j.bios.2016.08.001. URL: <http://www.sciencedirect.com/science/article/pii/S0956566316307485> (visited on 04/10/2019).
- [137] Tingting Wu et al. “Enhanced Lateral Flow Assay with Double Conjugates for the Detection of Exosomes”. In: *Science China Chemistry* 61.11 (Nov. 1, 2018), pp. 1423–1429. ISSN: 1869-1870. DOI: 10.1007/s11426-018-9305-6. URL: <https://doi.org/10.1007/s11426-018-9305-6> (visited on 04/10/2019).
- [138] Sheila López-Cobo et al. “Immunoassays for Scarce Tumour-Antigens in Exosomes: Detection of the Human NKG2D-Ligand, MICA, in Tetraspanin-Containing Nanovesicles from Melanoma”. In: *Journal of Nanobiotechnology*

- 16.1 (May 2, 2018), p. 47. ISSN: 1477-3155. DOI: 10.1186/s12951-018-0372-z. URL: <https://doi.org/10.1186/s12951-018-0372-z> (visited on 04/10/2019).
- [139] N. Nausch and A. Cerwenka. “NKG2D Ligands in Tumor Immunity”. In: *Oncogene* 27.45 (Oct. 2008), pp. 5944–5958. ISSN: 1476-5594. DOI: 10.1038/onc.2008.272. URL: <https://www.nature.com/articles/onc2008272> (visited on 04/10/2019).
- [140] Omodele Ashiru et al. “Natural Killer Cell Cytotoxicity Is Suppressed by Exposure to the Human NKG2D Ligand MICA*008 That Is Shed by Tumor Cells in Exosomes”. In: *Cancer Research* 70.2 (Jan. 15, 2010), pp. 481–489. ISSN: 0008-5472, 1538-7445. DOI: 10.1158/0008-5472.CAN-09-1688. pmid: 20068167. URL: <http://cancerres.aacrjournals.org/content/70/2/481> (visited on 04/10/2019).
- [141] Max Schütz et al. “Hydrophilically Stabilized Gold Nanostars as SERS Labels for Tissue Imaging of the Tumor Suppressor P63 by Immuno-SERS Microscopy”. In: *Chemical Communications* 47.14 (Mar. 22, 2011), pp. 4216–4218. ISSN: 1364-548X. DOI: 10.1039/C0CC05229A. URL: <https://pubs.rsc.org/en/content/articlelanding/2011/cc/c0cc05229a> (visited on 06/21/2019).
- [142] Ulf Andreasson et al. “A Practical Guide to Immunoassay Method Validation”. In: *Frontiers in Neurology* 6 (Aug. 19, 2015). ISSN: 1664-2295. DOI: 10.3389/fneur.2015.00179. pmid: 26347708. URL: <https://www.ncbi.nlm.nih.gov/pmc/articles/PMC4541289/> (visited on 05/28/2019).
- [143] Annika Meiners et al. “Conjugation of Spin Labeled Proteins to Fluorescent Quantum Dots”. In: *Materials Today: Proceedings*. 7th NRW Nano-Conference 4 (Jan. 1, 2017), S180–S187. ISSN: 2214-7853. DOI: 10.1016/j.matpr.2017.09.184. URL: <http://www.sciencedirect.com/science/article/pii/S221478531731917X> (visited on 07/16/2019).
- [144] Wolfgang Haiss et al. “Determination of Size and Concentration of Gold Nanoparticles from UVVis Spectra”. In: *Analytical Chemistry* 79.11 (June 1, 2007), pp. 4215–4221. ISSN: 0003-2700. DOI: 10.1021/ac0702084. URL: <https://doi.org/10.1021/ac0702084> (visited on 05/14/2019).

- [145] CytoDiagnostics Inc. *Introduction to Gold Nanoparticle Characterization - Cytodiagnosics*. URL: <http://www.cytodiagnosics.com/store/pc/viewcontent.asp?idpage=3> (visited on 05/14/2019).
- [146] Vi Tran et al. “Probing the SERS Brightness of Individual Au Nanoparticles, Hollow Au/Ag Nanoshells, Au Nanostars and Au Core/Au Satellite Particles: Single-Particle Experiments and Computer Simulations”. In: *Nanoscale* 10.46 (Nov. 29, 2018), pp. 21721–21731. ISSN: 2040-3372. DOI: 10.1039/C8NR06028B. URL: <https://pubs.rsc.org/en/content/articlelanding/2018/nr/c8nr06028b> (visited on 06/21/2019).
- [147] Jacek Jasieniak et al. “Re-Examination of the Size-Dependent Absorption Properties of CdSe Quantum Dots”. In: *The Journal of Physical Chemistry C* 113.45 (Nov. 12, 2009), pp. 19468–19474. ISSN: 1932-7447. DOI: 10.1021/jp906827m. URL: <https://doi.org/10.1021/jp906827m> (visited on 06/17/2019).
- [148] Sungjee Kim et al. “Type-II Quantum Dots: CdTe/CdSe(Core/Shell) and CdSe/ZnTe(Core/Shell) Heterostructures”. In: *Journal of the American Chemical Society* 125.38 (Sept. 1, 2003), pp. 11466–11467. ISSN: 0002-7863. DOI: 10.1021/ja0361749. URL: <https://doi.org/10.1021/ja0361749> (visited on 06/17/2019).
- [149] Wenhai Han et al. “Cryo Atomic Force Microscopy: A New Approach for Biological Imaging at High Resolution”. In: *Biochemistry* 34.26 (July 4, 1995), pp. 8215–8220. ISSN: 0006-2960. DOI: 10.1021/bi00026a001. URL: <https://doi.org/10.1021/bi00026a001> (visited on 05/09/2019).
- [150] Michael Reth. “Matching Cellular Dimensions with Molecular Sizes”. In: *Nature Immunology* 14.8 (Aug. 2013), pp. 765–767. ISSN: 1529-2908, 1529-2916. DOI: 10.1038/ni.2621. URL: <http://www.nature.com/articles/ni.2621> (visited on 05/09/2019).
- [151] Martina Bielefeld-Sevigny. “AlphaLISA Immunoassay Platform— The “No-Wash” High-Throughput Alternative to ELISA”. In: *ASSAY and Drug Development Technologies* 7.1 (Feb. 1, 2009), pp. 90–92. ISSN: 1540-658X. DOI: 10.1089/adt.2009.9996. URL: <https://www.liebertpub-com.zorac.aub.aau.dk/doi/10.1089/adt.2009.9996> (visited on 07/12/2019).

- [152] Fritz Poulsen and Kirsten Borres Jensen. “A Luminescent Oxygen Channeling Immunoassay for the Determination of Insulin in Human Plasma”. In: *Journal of Biomolecular Screening* 12.2 (Mar. 1, 2007), pp. 240–247. ISSN: 1087-0571. DOI: 10.1177/1087057106297566. URL: <https://doi.org/10.1177/1087057106297566> (visited on 07/12/2019).
- [153] *Alpha Reagents/PerkinElmer*. URL: <http://www.perkinelmer.com/de/category/alpha-reagents> (visited on 08/12/2019).

8 Appendix

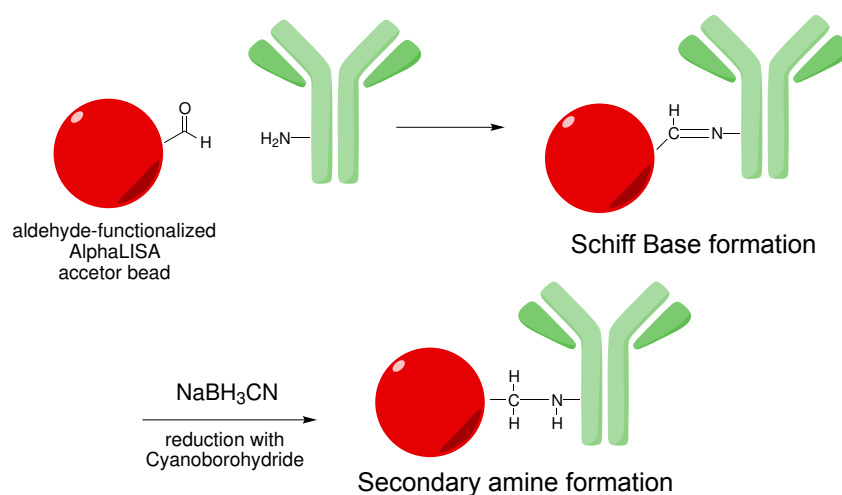


Figure 8.1 Simplified reaction of aldehyde-functionalized AlphaLISA acceptor beads with amine groups of antibodies. After formation of a Schiff base between these two groups, they were reduced by sodium cyanoborohydride, giving an irreversible linkage between beads and antibodies. Reaction components not to scale.

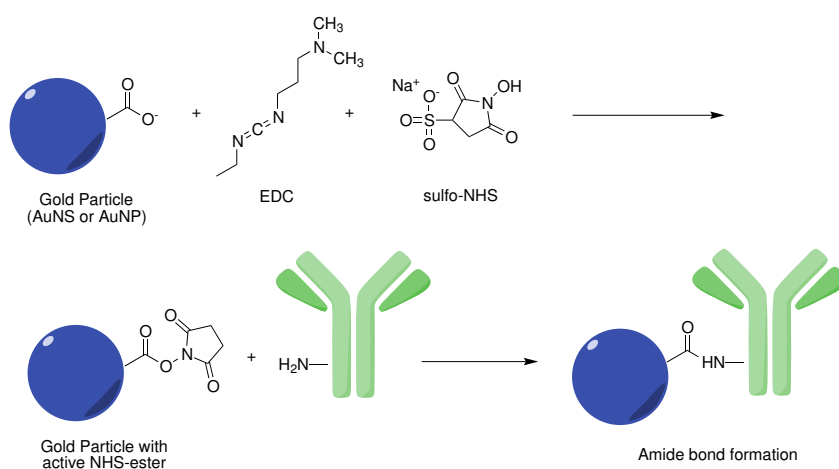


Figure 8.2 Reaction for the activation of carboxylic acid groups of the PEG-coating of gold particles by EDC and sulfo-NHS. When the active sulfo-NHS ester is formed with carboxylic acid groups, these can react with amine groups of antibodies to form an amide bond. Formation of the active sulfo-NHS ester for AuNS was performed by Vi Tran, whereas AuNP were purchased functionalized with the leaving group. Reaction components not to scale.

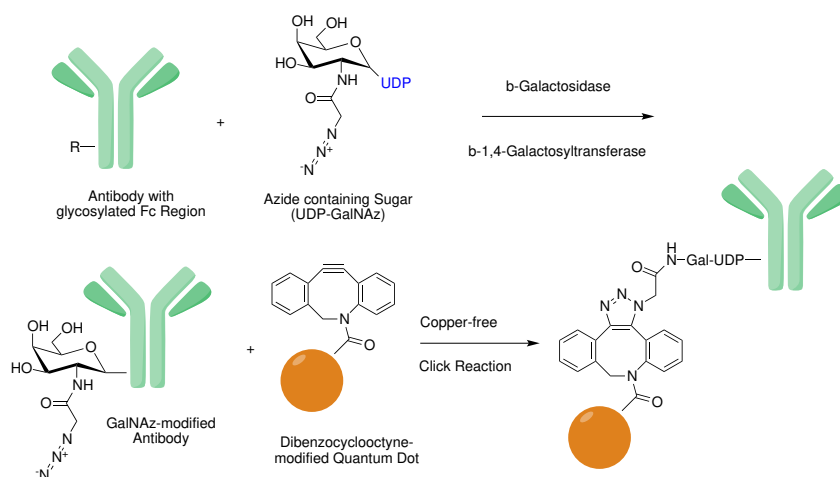


Figure 8.3 Simplified reaction scheme for the commercial QD conjugation kit. First, the glycosylation pattern of antibodies should be modified by β -Galactosidase. Then, UDP-N-azidoacetylgalactosamine (UDP-GalNAz) the azide containing sugar moiety is attached to the hydrocarbon chain by β -1,4-galactosyltransferase. Thereafter, the copper-free click reaction occurs with dibenzocyclooctyne-groups of QDs to form the conjugate. Reaction components not to scale.

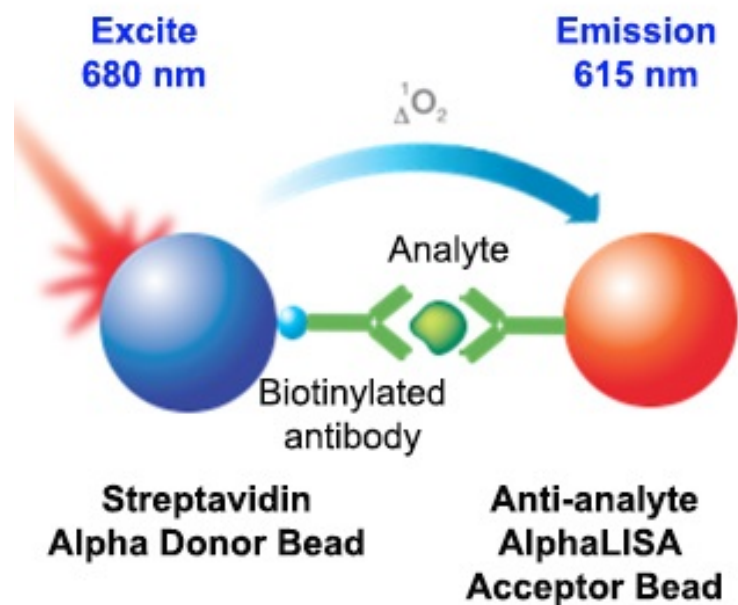


Figure 8.4 Schematic illustration of the AlphaLISA assay principle. The analyte is bound by one antibody, conjugated with AlphaLISA acceptor beads and another antibody labelled with biotin. After formation of the sandwich-type structure between antibodies and the analyte, streptavidin coated donor beads bind to biotin-residues of one antibody population. Thereafter, reactive oxygen species can be liberated by donor beads upon excitation with laser light at 680 nm. The channelling of oxygen species to AlphaLISA acceptor beads then causes the emission of chemiluminescence light at 615 nm from the latter bead type. The intensity of detected chemiluminescence correlates with the amount of bound target molecules. Figure taken from [153].

size distributions of self-conjugated AlphaLISA beads

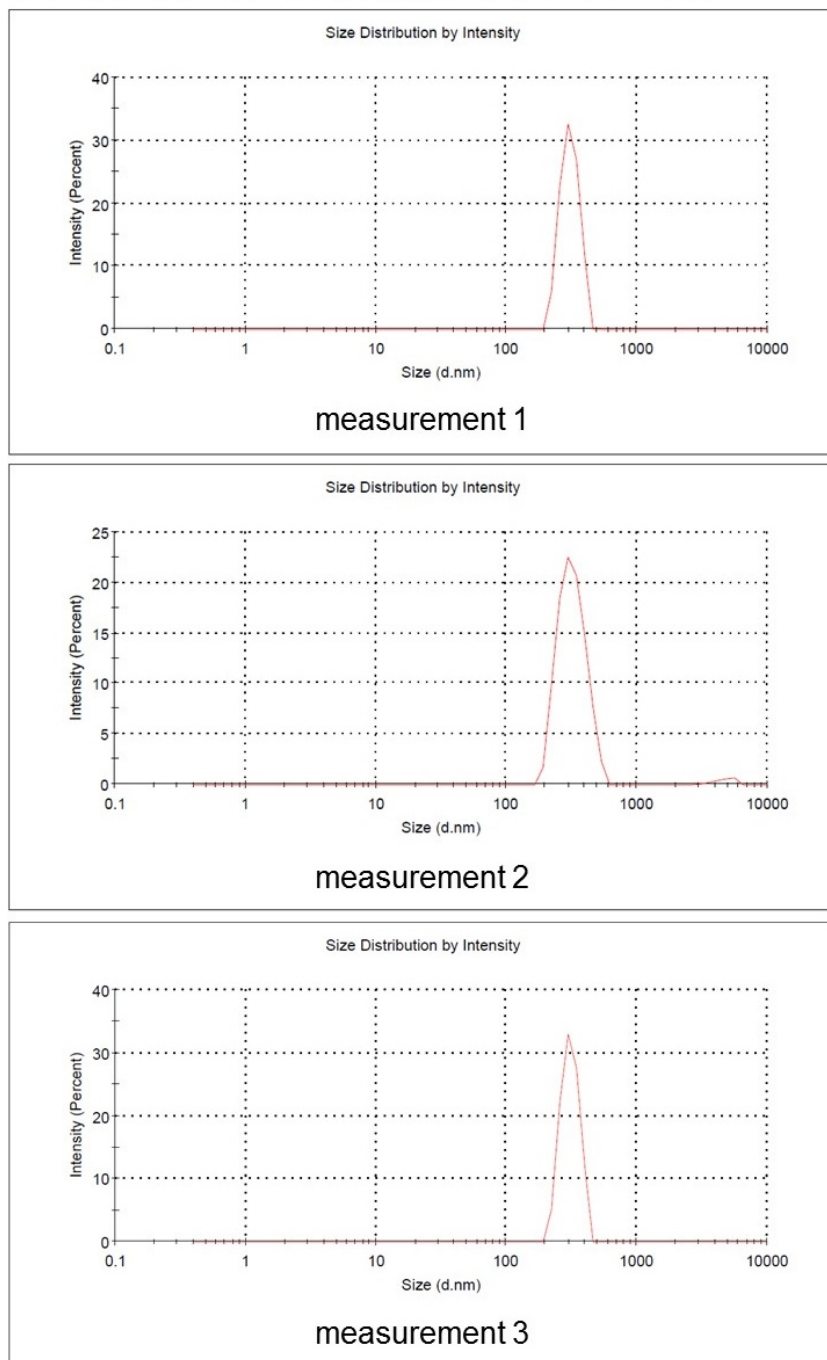


Figure 8.5 Size distributions by number of three measurements performed with AlphaLISA beads that were coupled in-house to anti-PTEN antibodies.

size distributions of commercial beads with coupled Abs

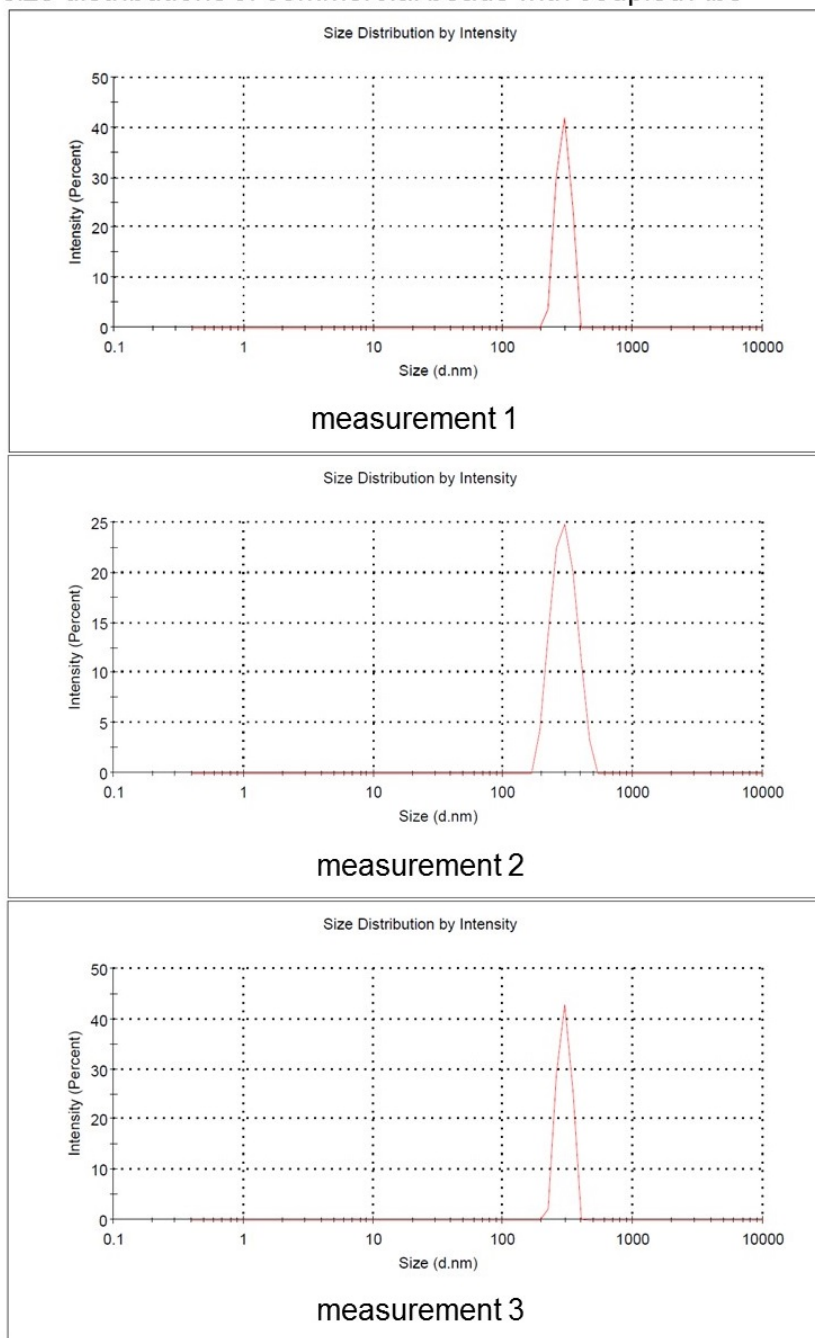


Figure 8.6 Size distributions by number of three measurements performed with AlphaLISA beads that are purchased with coupled anti-PTEN antibodies.

size distributions of unconjugated AuNP I

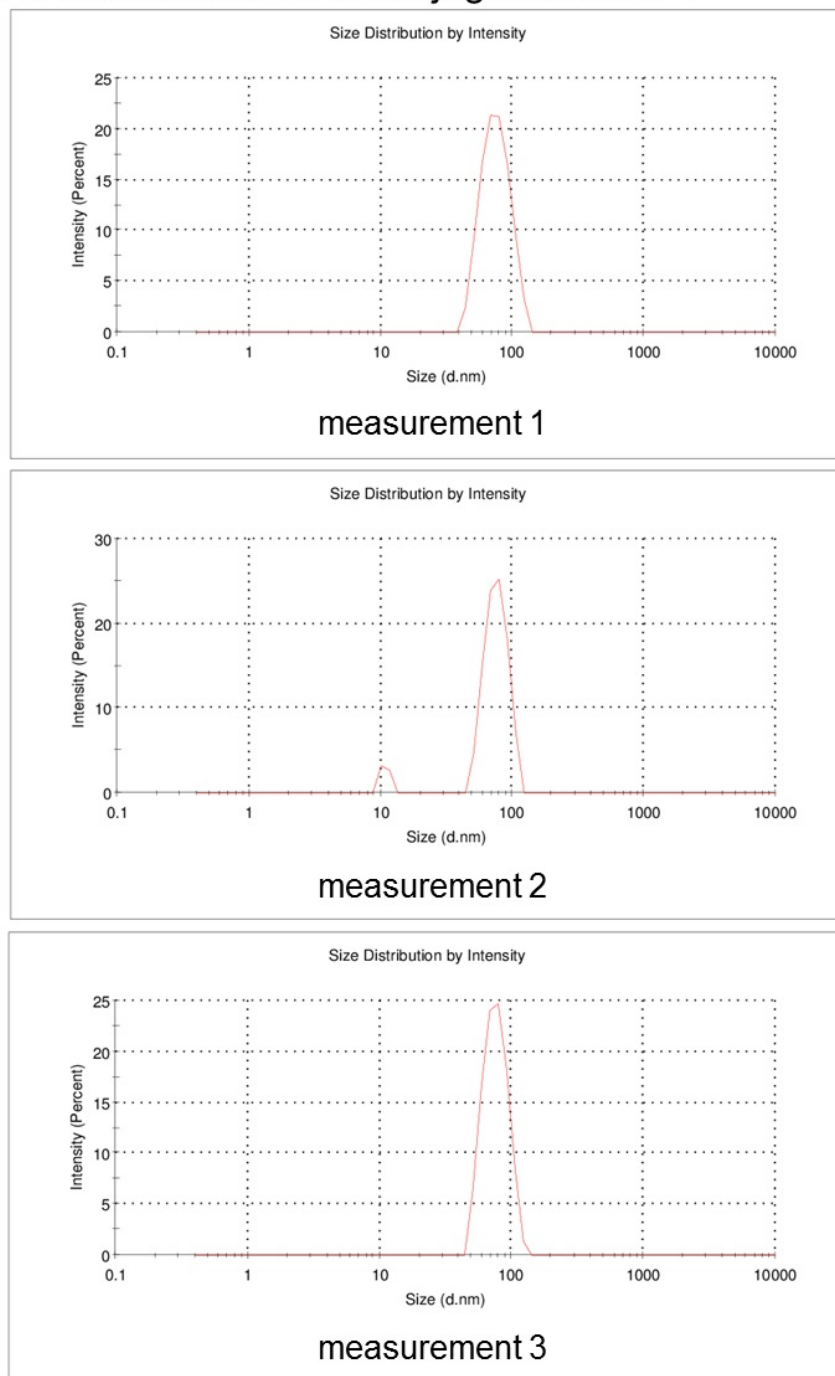


Figure 8.7 Size distributions by intensity for measurements 1 to 3, performed with unconjugated AuNP at $OD = 1$ in AuNP storage buffer.

size distributions of unconjugated AuNP II

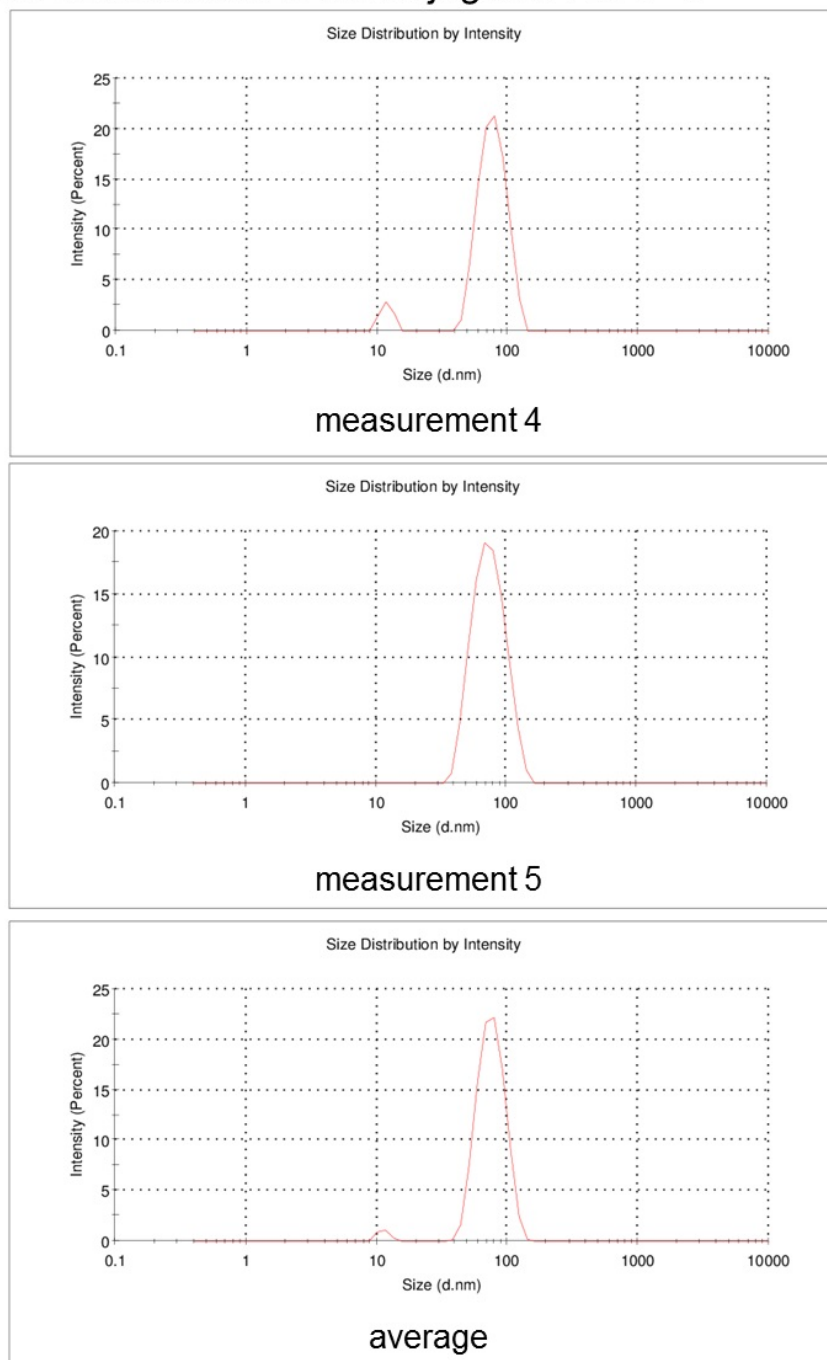


Figure 8.8 Size distributions by intensity for measurements 4 and 5, as well as the average for all 5 measurements, obtained with unconjugated AuNP at $OD = 1$ in AuNP storage buffer.

size distributions of antibody-conjugated AuNP I

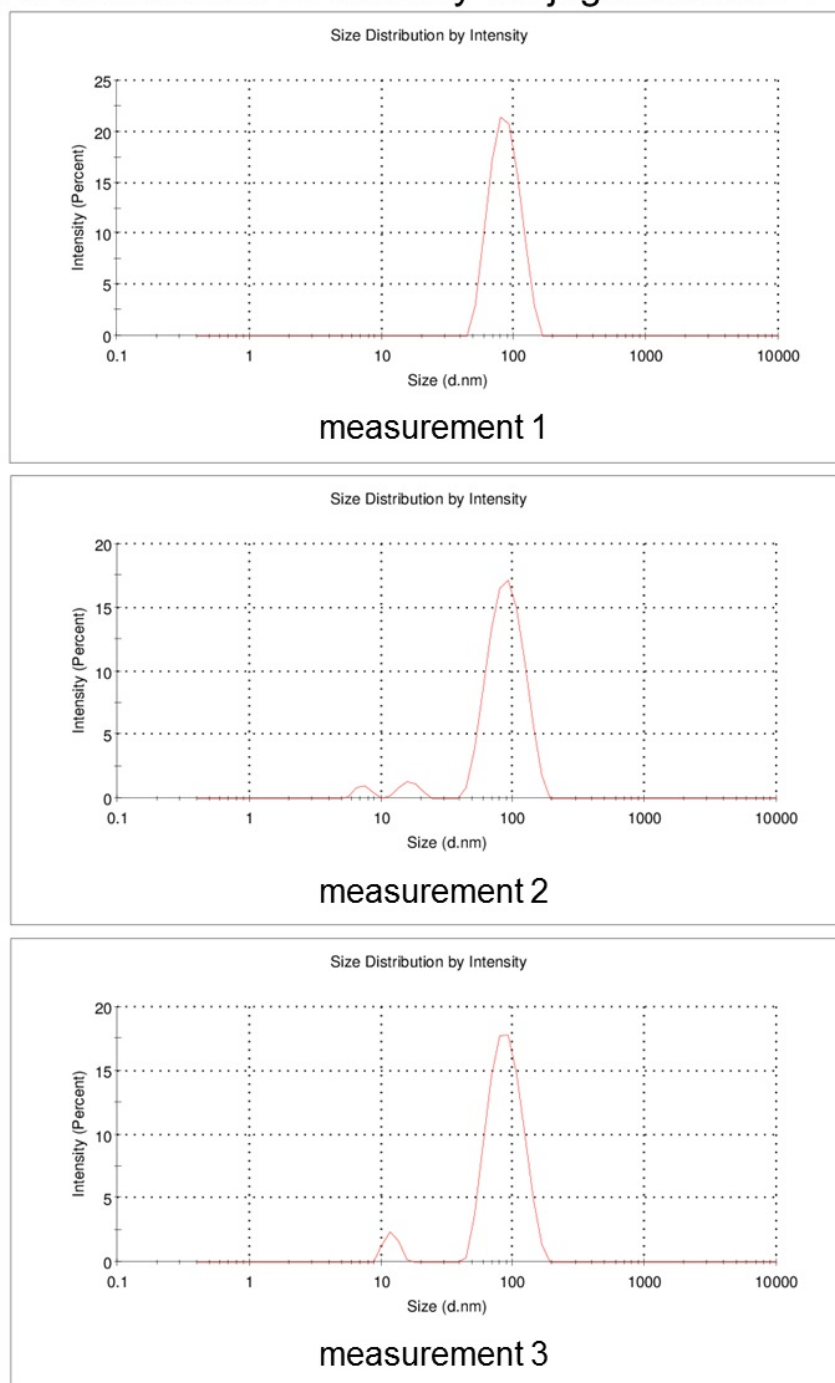


Figure 8.9 Size distributions by intensity for measurements 1 to 3, performed with AuNP after conjugation. The concentration was adjusted to $OD = 1$ with storage buffer for AuNP.

size distributions of antibody-conjugated AuNP II

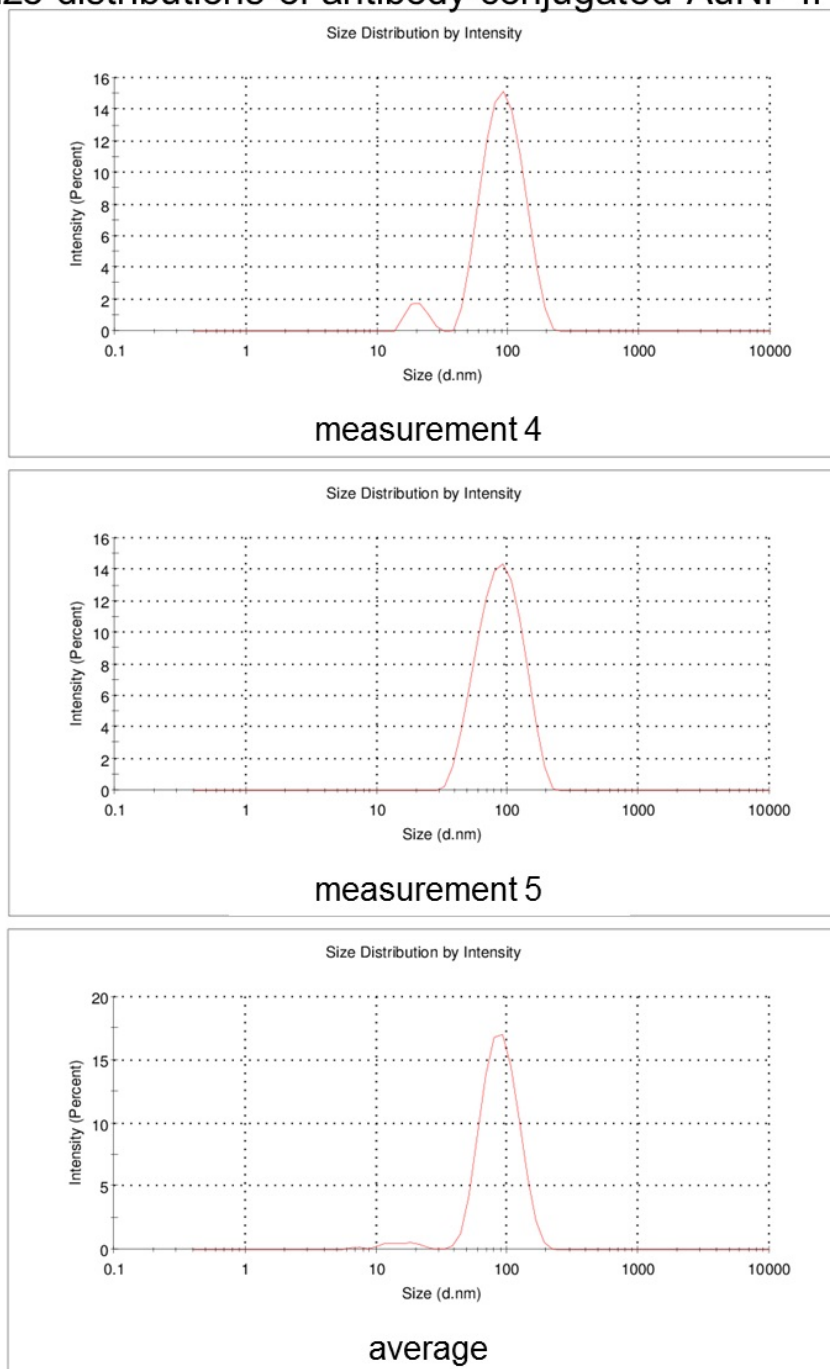


Figure 8.10 Size distributions by intensity for measurements 4 and 5, as well as the average for all 5 measurements, obtained AuNP after conjugation. The concentration was adjusted to $OD = 1$ with AuNP storage buffer.

size distributions of unconjugated AuNS

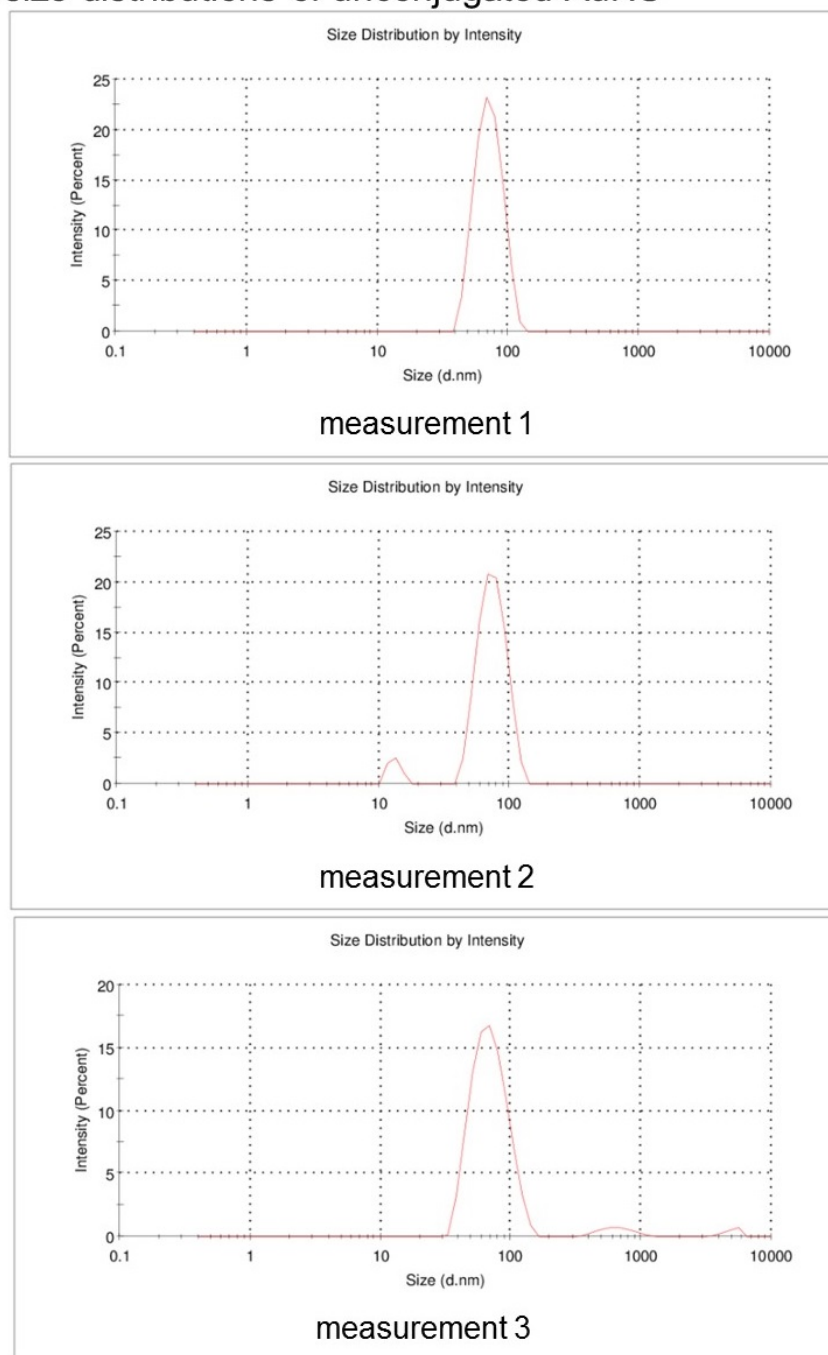


Figure 8.11 Size distributions by intensity for the three measurements of AuNS before conjugation, performed at an $OD = 0.08$ after dilution in PBS.

size distributions of AuNS-conjugates with Antibodies

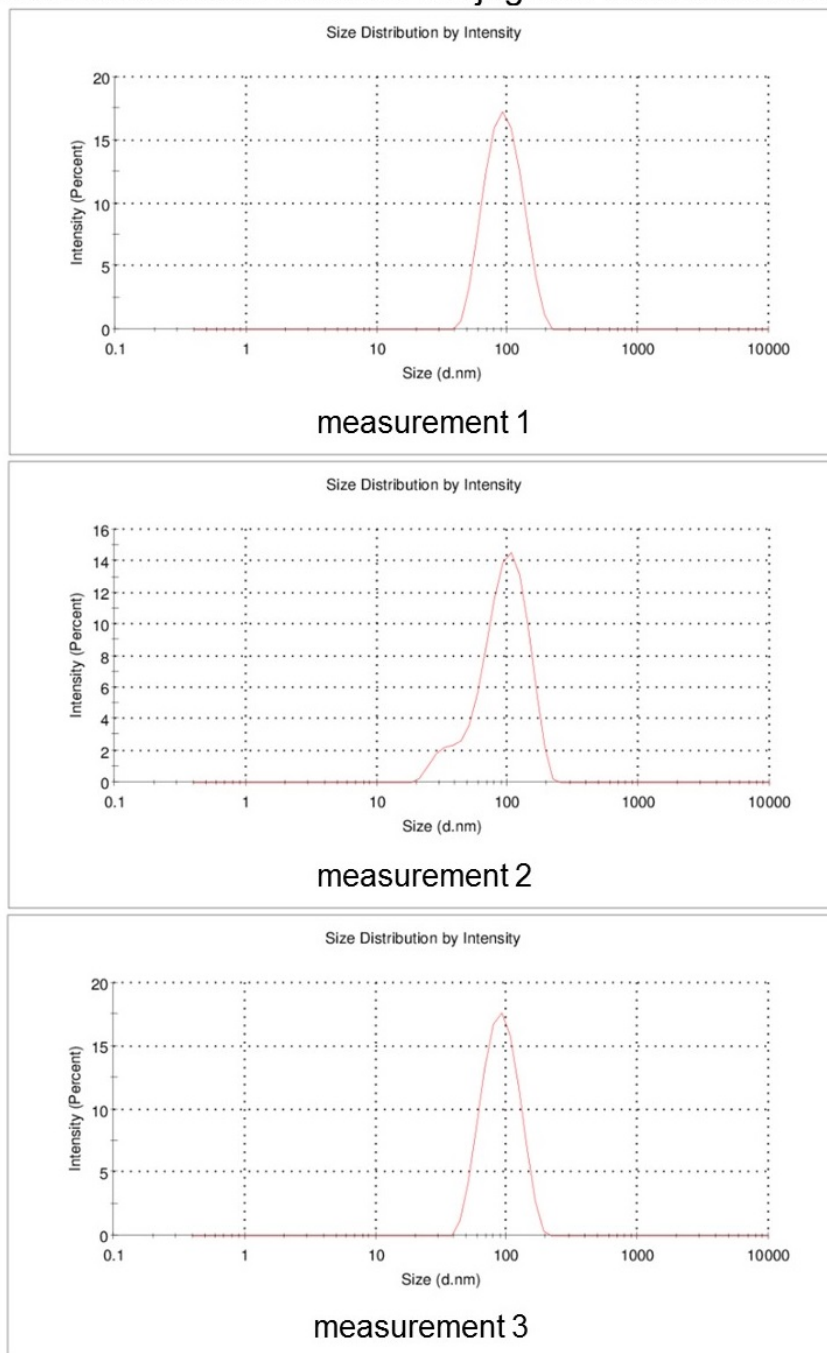


Figure 8.12 Size distributions by intensity for the three measurements of AuNS-conjugated with anti-PTEN antibody, obtained at an $OD = 0.8$ after dilution in PBS.

size distributions of unconjugated QDots625

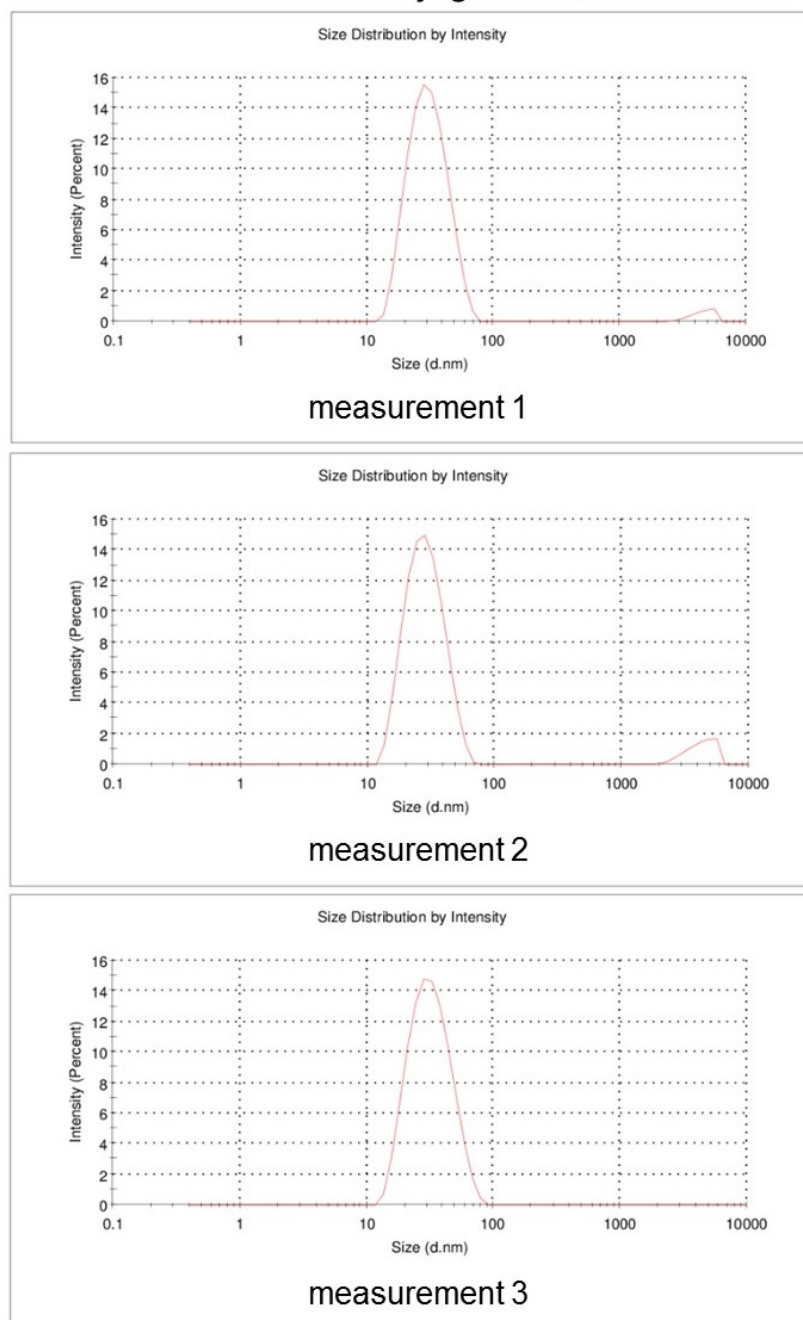


Figure 8.13 Size distributions by intensity for all three measurements performed with unconjugated QDots625. The supplied stock solution was diluted 1:200 in Tris buffer, pH 7.0.

size distributions of conjugated QDots625-Ab

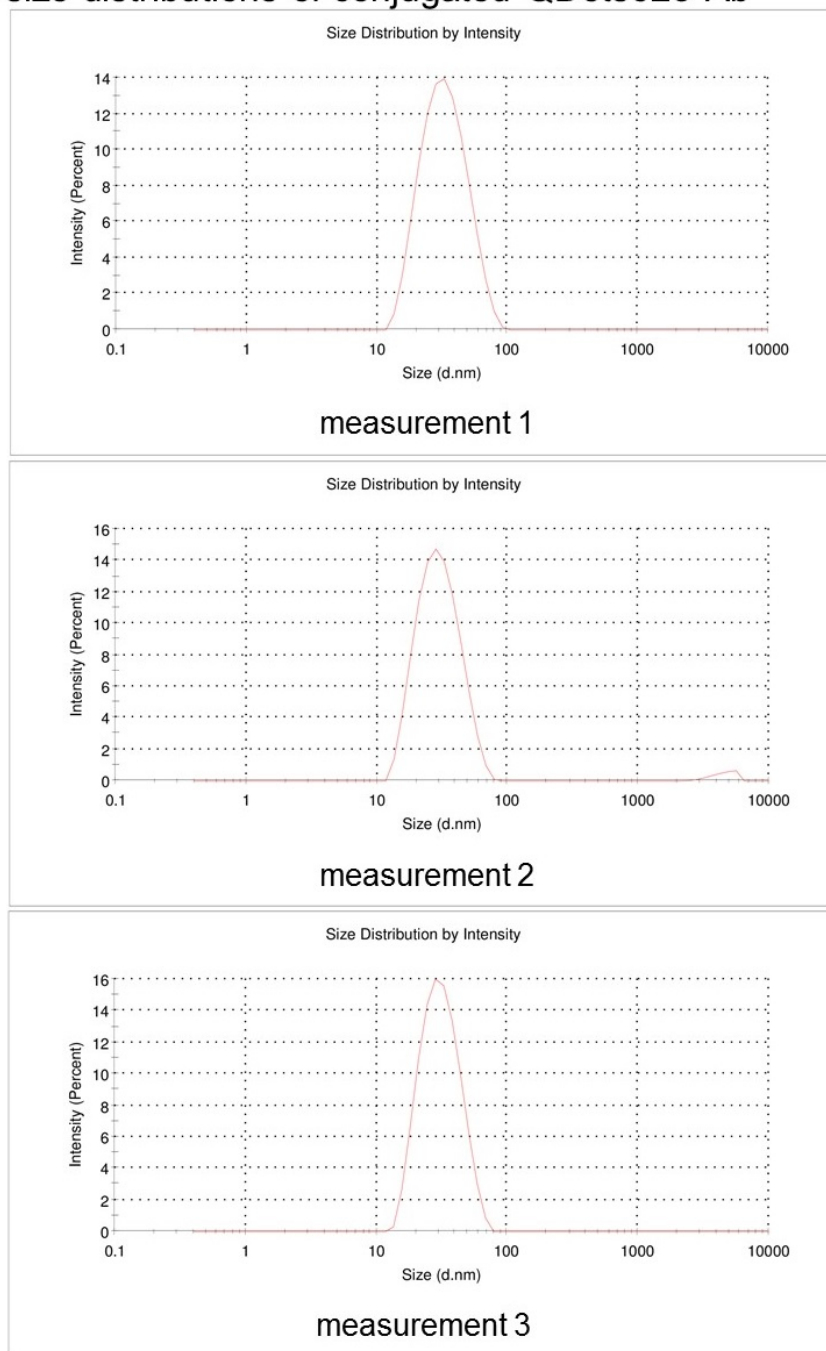


Figure 8.14 Size distributions by intensity for all three measurements performed with QDots625 after conjugation with anti-PTEN antibody. The solution of conjugate was diluted 1:500 in Tris buffer, pH 7.0.

Standard Curve for PTEN on microtiter plate in concentrated medium - 1 h incubation

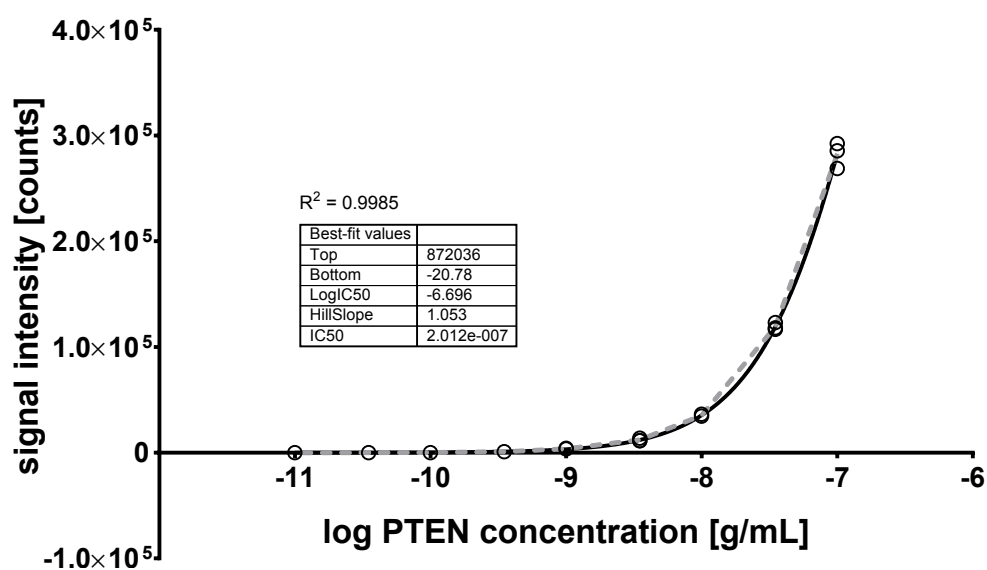


Figure 8.15 Calibration curve for PTEN diluted in concentrated medium (concentration factor: 80 \times), obtained using AlphaLISA beads conjugated to anti-PTEN antibody in-house in a standard protocol on microtiter plates. The incubation time of antibodies with PTEN was 1 h. Signals were recorded for 300 ms on a Tecan Infinite M1000pro, after excitation of donor beads at 680 nm for 100 ms. All samples were prepared in triplicates, together with four blanks in triplicate. Values for each data point are given by open circles as the blank-corrected signal and the mean for each PTEN concentration is represented by the grey dashed line. The black solid line represents the 4-parameter logistics function with the indicated results and goodness of fit R^2 .

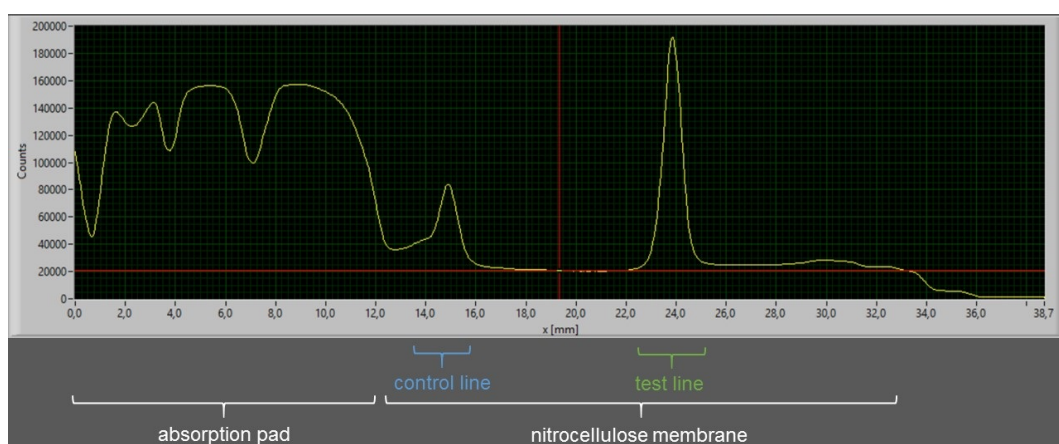


Figure 8.16 Typical scan of lateral flow strips obtained from the LRE CPoCLabFluo reader. The employed concentration of PTEN in this sample was $1 \times 10^{-8} \text{ g mL}^{-1}$, detected with anti-PTEN antibody coupled to AlphaLISA beads. Characteristic regions of the scan are labelled with respect to the regions of the lateral flow strip.

**Standard Curve for PTEN on Lateral Flow Strips
in AlphaLISA buffer - 1 h incubation**

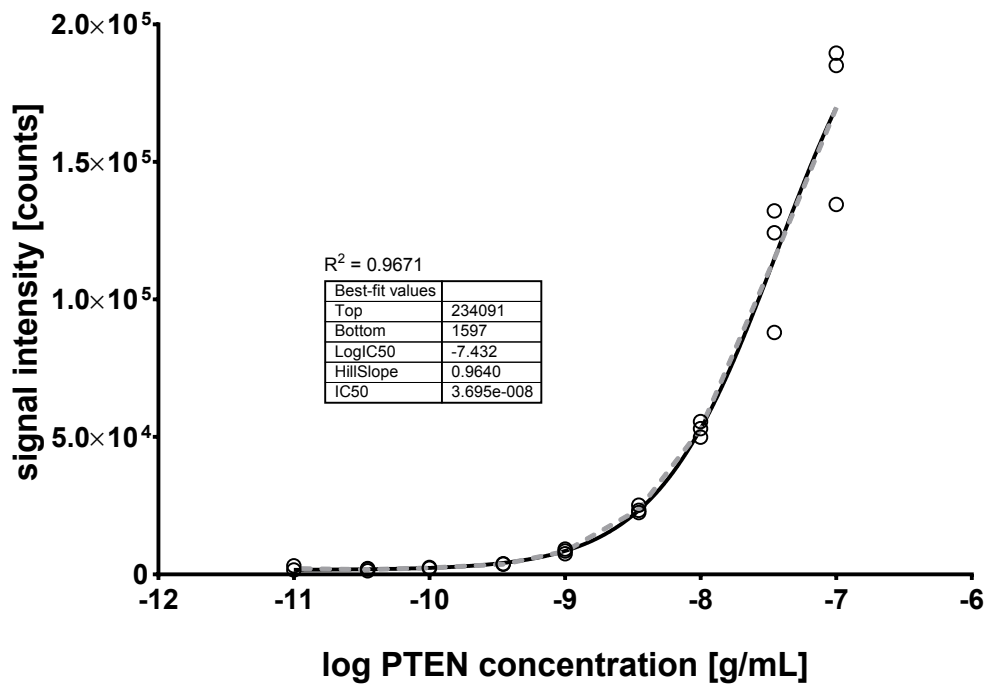


Figure 8.17 Calibration curve for PTEN diluted in AlphaLISA assay buffer with 2 % PEG-4000, using AlphaLISA beads conjugated to anti-PTEN antibody in-house and incubated with the analyte for 1 h. Signals were recorded on an LRE cPoCLabFluo reader and samples were prepared in triplicates. Values for each data point are given by open circles as the blank-corrected maximum signal at the test line and the mean for each PTEN concentration is represented by the grey dashed line. The black solid line represents the 4-parameter logistics function with the indicated results and goodness of fit R^2 .

**Measured Signal Intensities of AlphaLISA beads
imaged on ChemiDoc MP system - 5 h incubation**

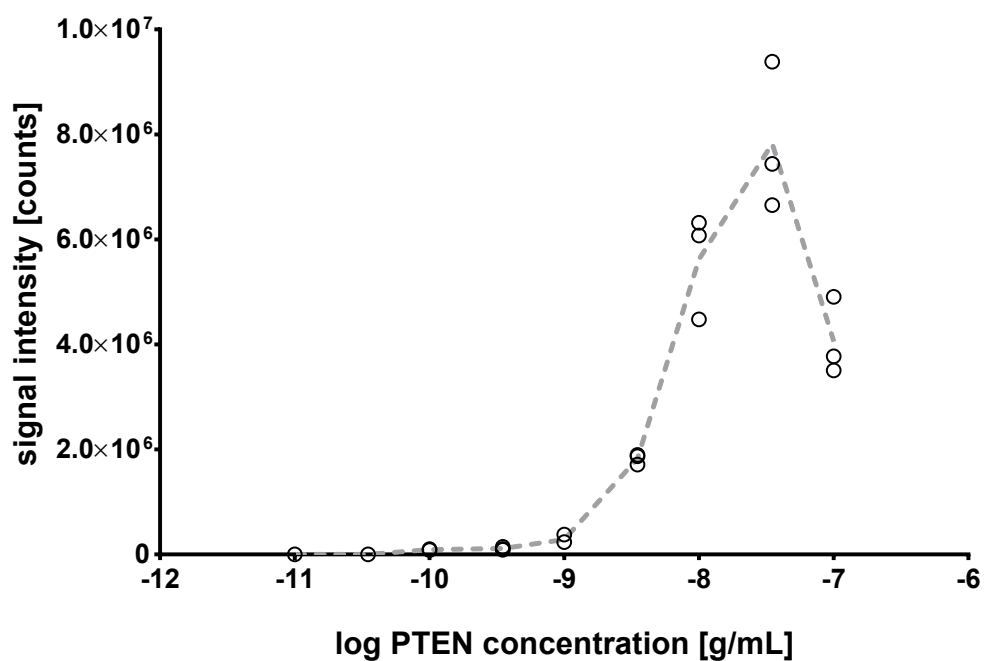


Figure 8.18 Obtained signal intensities for AlphaLISA beads conjugated to anti-PTEN antibody in-house and incubated with the analyte for 5 h. Strips were imaged on a ChemiDoc MP system and analyzed with Lab View software. Values for each data point are given by open circles and the mean for each PTEN concentration is represented by the grey dashed area. A 4-parameter logistics function could not be fitted to the obtained data.

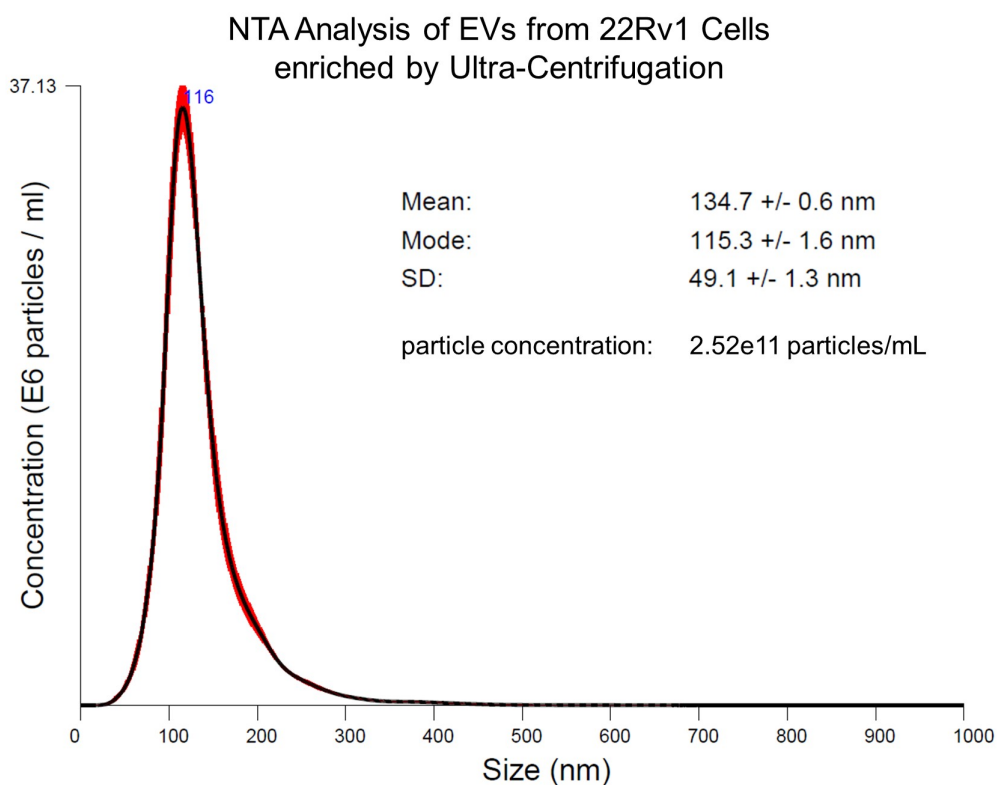


Figure 8.19 The average size distribution of particles ± 1 standard error of the mean is depicted, as it was determined from three nanoparticle tracking analysis measurements. A 1:100 dilution of a sample from 22Rv1 cells was measured, which was prepared by ultra-centrifugation. Additionally, the mean size and the mode of the particle sizes are given together with the SD of the size. The given particle concentration reflects the one found in the undiluted sample.

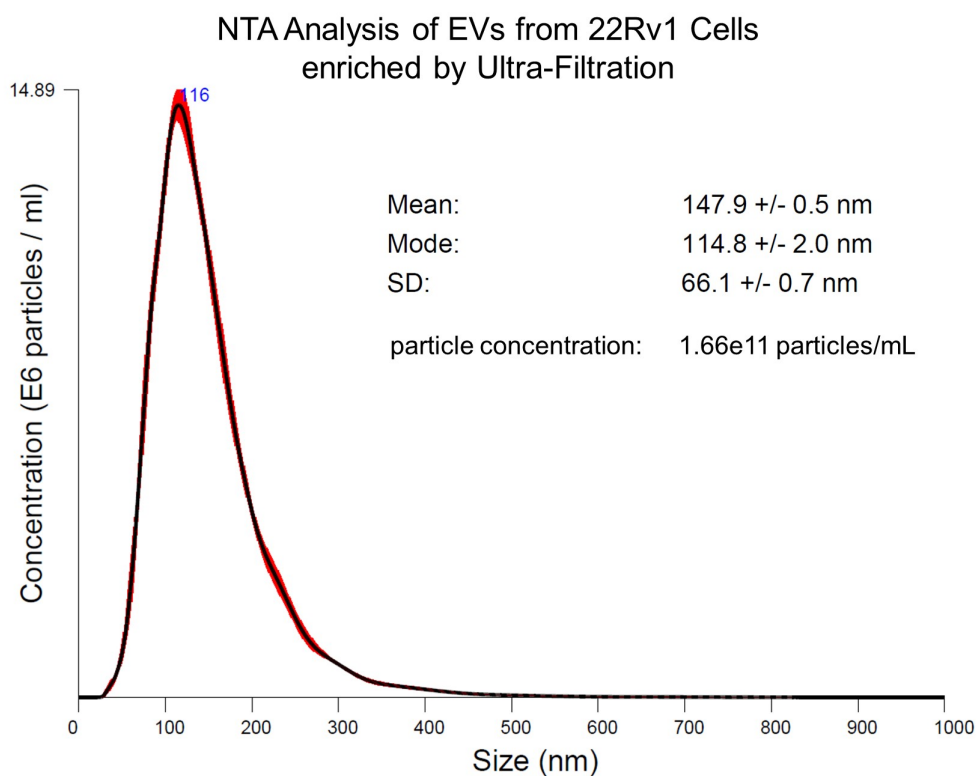


Figure 8.20 The average size distribution of particles ± 1 standard error of the mean is depicted, as it was determined from three nanoparticle tracking analysis measurements. A 1:100 dilution of a sample from 22Rv1 cells was measured, which was prepared by ultra-filtration. Additionally, the mean size and the mode of the particle sizes are given together with the SD of the size. The given particle concentration reflects the concentration found in the undiluted sample.

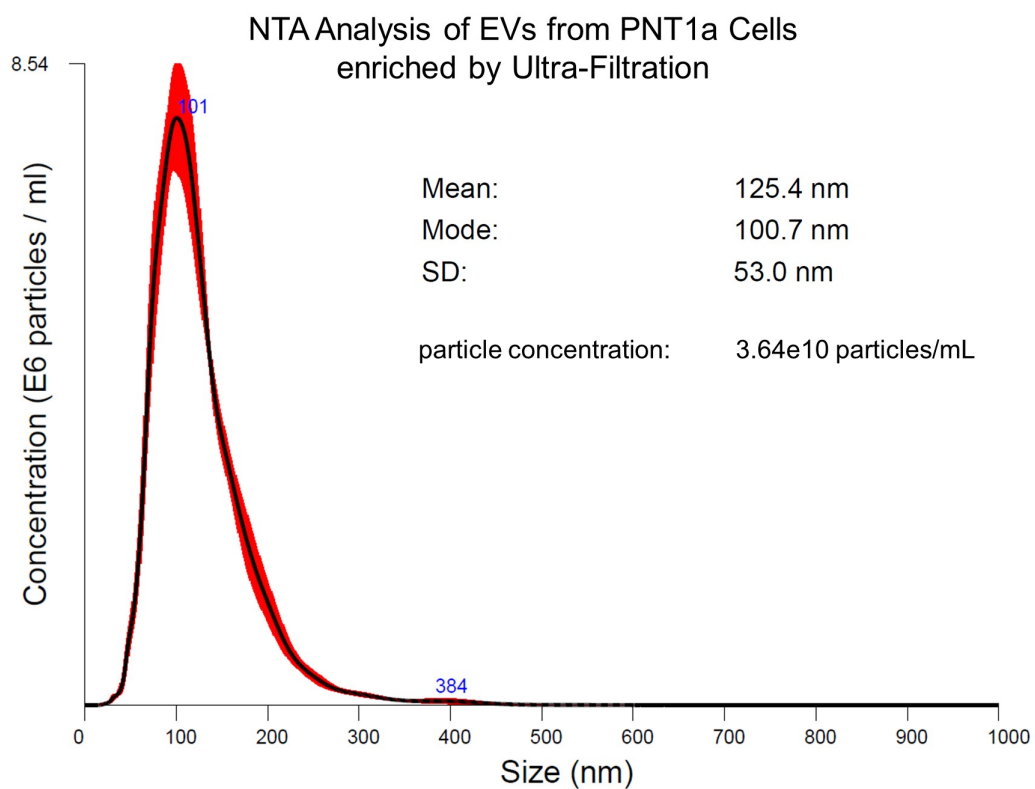


Figure 8.21 The average size distribution of particles ± 1 standard error of the mean is depicted, as it was determined from three nanoparticle tracking analysis measurements. A 1:50 dilution of a sample from PNT1a cells was measured, which was prepared by ultra-filtration. Additionally, the mean size and the mode of the particle sizes are given together with the SD of the size. The given particle concentration reflects the concentration found in the undiluted sample.

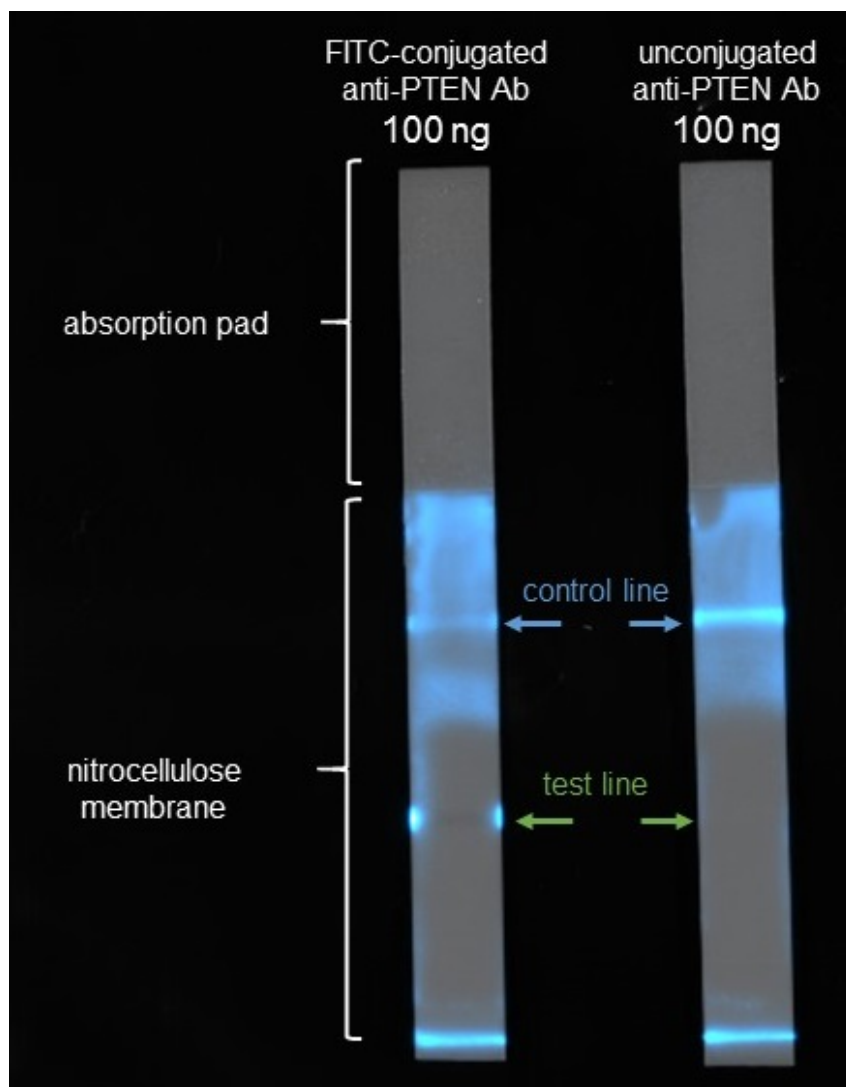


Figure 8.22 Colorimetric image of lateral flow strips overlaid with chemiluminescence image (cyan) from HRP substrate. Sample and conjugate pad, as well as the covering plastic film were removed from strips. On the left, a slight accumulation at the test line edges is visible for the FITC-labelled antibody, which is not visible for the unconjugated antibody (right strip). The control line shows an accumulation of signal for both the unmodified and the FITC-conjugated antibody.

Raman Spectra of blank Sample after running and of an unused Nitrocellulose Membrane without running

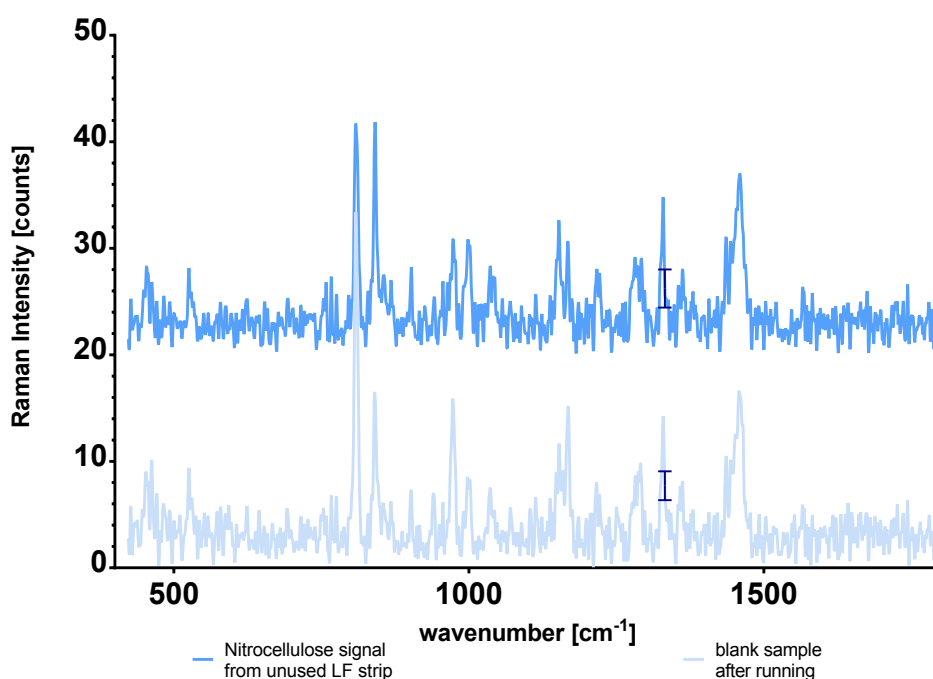


Figure 8.23 Comparison of Raman spectra of the test line region of commercial lateral flow strip after running blank samples and of an unused lateral flow strips. Signals of the nitrocellulose itself (shifted by $y = 20counts$) observed for unused strips show that the material shows a slight signal around 1340 cm^{-1} as the marker band of 4-NTB, which has a similar intensity to that of blanks. The SD of the peak maxima in the marker band region of 4-NTB is indicated by error bars. Hence unspecific binding of AuNS at the test line for PTEN-negative samples was negligible.

Raman Spectra of AuNS-conjugates at different Locations of the Test Line

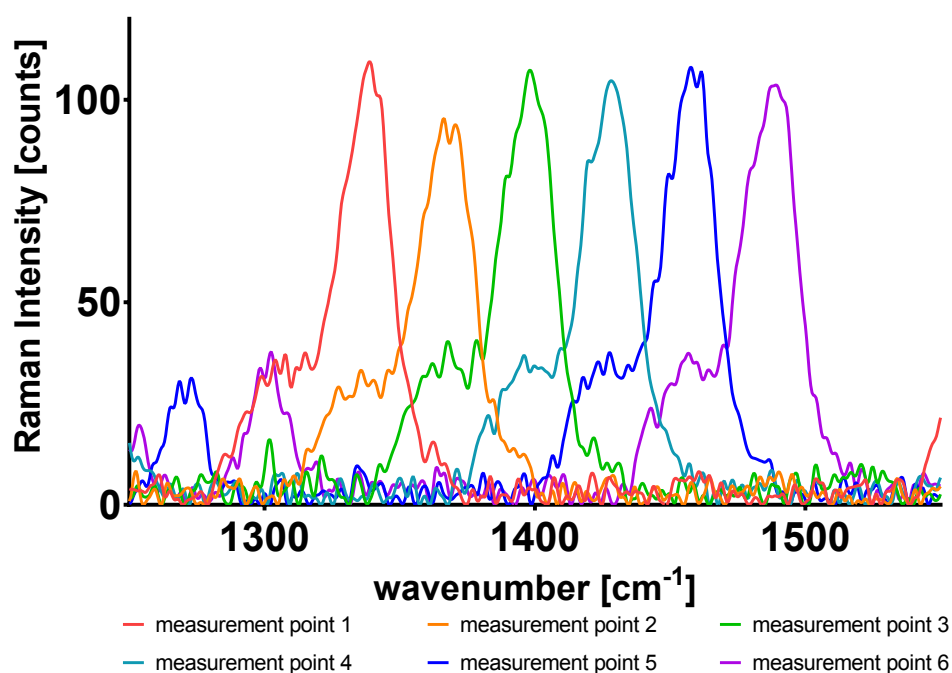


Figure 8.24 Raman spectra of the 4-NTB marker band region around a wavenumber of 1340 cm^{-1} obtained at six different points of the test line of commercial lateral flow strip using $8.75 \times 10^{-8}\text{ g mL}^{-1}$ PTEN. The spectra of each measurement point are shifted by 50 cm^{-1} with respect to the previous measurement point. The appearance of the peaks of the marker band indicates a homogeneous distribution of conjugated AuNS on the test line.

Raman Spectra of the Test Line Region of Lateral Flow Strips with different PTEN concentrations

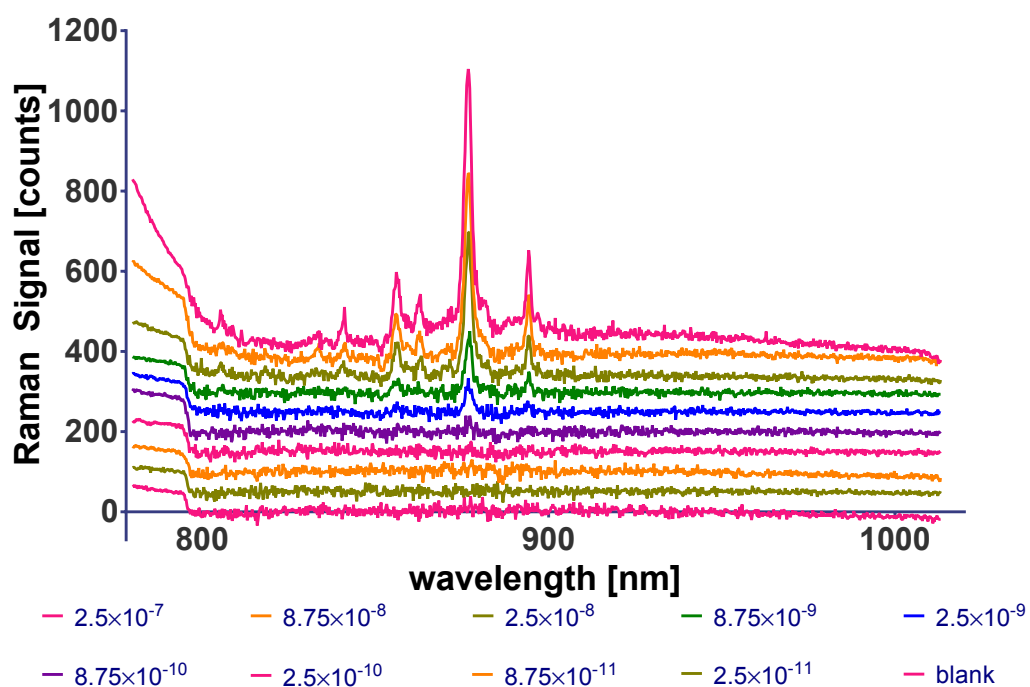


Figure 8.25 Baseline corrected Raman spectra recorded at the test line of lateral flow strips for the indicated concentrations of PTEN in g mL^{-1} . The spectra of each measurement point are shifted by 50 counts with respect to the preceding lower concentration. The marker band of 4-NTB lies at a wavelength of approximately 877 nm.

9 Acknowledgements

First, I would like to thank Aalborg University and Leonid Gurevich for the possibility to perform my master thesis in the way it was carried out and for its evaluation.

Secondly, I want to express my gratitude to the Fraunhofer IZI and especially to Dr. Dirk Kuhlmeier, who welcomed me in the institute, provided a project and allowed me to carry out my master thesis in the most convenient way possible. I also thank Dr. Kuhlmeier for the fruitful discussions, for providing fresh ideas and insights as well as for his enthusiasm in supporting the project. It was a pleasure to work in his research group.

Additionally, I also thank all other members of the Microdiagnostics Group, who supported me with my lab work. I especially thank Ana Lopes for being my supervisor and giving me guidance and practical support throughout my master thesis. Furthermore I am thankful to Susann Allelein for providing EV samples and giving advice and sharing knowledge about EV research. I also thank Sabrina Rau for providing insight into AlphaLISA assays and helping in the transfer of the system to lateral flow strips. Without all this support, I would not have been able to perform the master thesis in the way it is presented here.

Furthermore, I thank Prof. Dr. Sebastian Schlücker from the University of Duisburg-Essen for the cooperation in the framework of this master thesis. The possibility to perform measurements in the group's facilities is highly acknowledged, as well as the help of Vi Tran, who performed conjugation of Raman-active gold particles and assisted with conduction of lateral flow assays using these reporter molecules, as well as with the data acquisition.